



Kent Academic Repository

Evitts, Jack J (2020) *An analysis on the photometric variability of V 1490 Cyg.* Master of Science by Research (MScRes) thesis, University of Kent,.

Downloaded from

<https://kar.kent.ac.uk/80982/> The University of Kent's Academic Repository KAR

The version of record is available from

This document version

Other

DOI for this version

Licence for this version

UNSPECIFIED

Additional information

Versions of research works

Versions of Record

If this version is the version of record, it is the same as the published version available on the publisher's web site. Cite as the published version.

Author Accepted Manuscripts

If this document is identified as the Author Accepted Manuscript it is the version after peer review but before type setting, copy editing or publisher branding. Cite as Surname, Initial. (Year) 'Title of article'. To be published in *Title of Journal*, Volume and issue numbers [peer-reviewed accepted version]. Available at: DOI or URL (Accessed: date).

Enquiries

If you have questions about this document contact ResearchSupport@kent.ac.uk. Please include the URL of the record in KAR. If you believe that your, or a third party's rights have been compromised through this document please see our [Take Down policy](https://www.kent.ac.uk/guides/kar-the-kent-academic-repository#policies) (available from <https://www.kent.ac.uk/guides/kar-the-kent-academic-repository#policies>).

UNIVERSITY OF KENT

CENTRE FOR ASTROPHYSICS AND PLANETARY SCIENCE
SCHOOL OF PHYSICAL SCIENCES

An analysis on the photometric variability of V 1490 Cyg

Author:

Jack J. Evitts

Supervisor:

Dr. Dirk Froebrich

Second Supervisor:

Dr. James Urquhart

A revised thesis submitted for the degree of

MSc by Research

10th April 2020



Abstract

Variability in Young Stellar Objects (YSOs) is one of their primary characteristics. Long-term, multi-filter, high-cadence monitoring of large samples aids understanding of such sources. Although data from the HOYS citizen science project allows for such monitoring, usage of different filters introduces colour-terms to the photometric data. This thesis outlines the development of a novel colour-term correction method, improving photometric error to within a couple of percent. The corrected light curve for the YSO, V 1490 Cyg, is then discussed in detail.

The source is observed to be a quasi-periodic dipper with a period of 31.447 ± 0.011 days. Long and short-term variability is observed for B, V, R_c and I_c data, with larger variability on short timescales for U and H_α . U amplitudes were observed to vary on timescales of hours, indicating the source is still accreting. No significant trends were observed in the structure function, with the amount of mass in the occulting structure seen to vary by up to a factor of 10 for both mass increase and decrease. The lower estimate of the typical accretion rate of V 1490 Cyg was found of the order $10^{-10} M_\odot/\text{year}$, consistent with low levels of accretion as seen in other T-Tauri stars. Investigating the orbiting structure in V vs. $V - I_c$ parameter space suggests low column density material with roughly ISM dust properties. Embedded in this envelope are denser, small-scale structures, most likely composed of larger dust grains. The scattering properties of this material are consistent and do not change over time. An accurate distance to both IC 5070 and V 1490 Cyg of 870^{+70}_{-55} pc has been determined using Gaia. Literature near-infrared (NIR) and mid-infrared (MIR) data suggest that V 1490 Cyg is most likely a CTTS, with a currently low, but variable accretion rate. It is potentially at the start of the transition into a WTTS or transition disk object. This thesis finds the nature of the variability of the source is most likely attributed to a protoplanet-induced disk warp.

Acknowledgements

This thesis has only become a reality with the kind support and help of many individuals. I would like to extend my sincere thanks to all of them.

Firstly, I would like to thank all contributors of data for their efforts towards the success of both the HOYS project and this study. Also many thanks to my fellow researchers who have helped in obtaining and discussing the data that is the backbone of this work. In particular I would like to express my special gratitude and thanks to my supervisor, Dr. Dirk Froebrich for imparting his knowledge and expertise.

I am highly indebted to both STFC (Grant no. ST/S505456/1) and the University of Kent for the funding that has enabled me to start and continue with this research.

Finally, I wish to thank and acknowledge my loving and supportive wife, Liz. Without her help, I could not have succeeded in this endeavour.

Declaration of Authorship

I, **Jack J. Evitts** declare that this thesis titled "*An analysis on the photometric variability of V 1490 Cyg*" and the work presented in it are my own and has been generated by me as the result of my own original research.

I confirm that:

1. This work was done wholly or mainly while in candidature for a research degree at this University;
2. Where any part of this thesis has previously been submitted for a degree or any other qualification at this University or any other institution, this has been clearly stated;
3. Where I have consulted the published work of others, this is always clearly attributed;
4. Where I have quoted from the work of others, the source is always given. With the exception of such quotations, this thesis is entirely my own work;
5. I have acknowledged all main sources of help;
6. Where the thesis is based on work done by myself jointly with others, I have made clear exactly what was done by others and what I have contributed myself.

Signed: Jack J. Evitts

Date: 10th April 2020

A summarised version of the data and analysis presented in this thesis has been written into a journal paper that has been submitted to, and accepted by, *Monthly Notices of the Royal Astronomical Society* for publication.

Contents

1	Introduction	3
1.1	Star Formation	4
1.2	Disks	5
1.3	Planet Formation	6
1.4	Variable Young Stars	7
2	HOYS	10
2.1	The Project	10
2.2	The Beacon Observatory	11
2.3	Targets	12
3	Observational Data and Photometric Calibration	13
3.1	V 1490 Cyg Imaging Observations	13
3.2	Photometry Data Calibration	13
3.2.1	Basic Relative Photometric Calibration	14
3.2.2	Photometry Colour Correction	15
3.3	Spectroscopy Data	21
4	Analysis of the Data for the Light Curve of V 1490 Cyg	26
4.1	The Quasi-Periodic Light Curve of V 1490 Cyg	26

4.2	Asymmetry of the Light Curve of V 1490 Cyg	34
4.3	Analysis of the Variability Fingerprints	35
4.4	Column Density Distribution of Consecutive Dips	39
4.5	Colour Dependence of Periodic Dips	49
5	Discussion	54
5.1	Distance of V 1490 Cyg	54
5.2	Potential Binarity of V 1490 Cyg	57
5.3	Literature NIR and MIR data for V 1490 Cyg	58
5.4	Evolutionary Stage of V 1490 Cyg	58
5.5	The Nature of V 1490 Cyg	60
5.5.1	Protoplanet-induced Disk Warp	61
5.5.2	Magnetically-induced Disk Warp	61
5.5.3	Hill Sphere of Accreting Protoplanet	62
6	Conclusions	63
	Bibliography	76
A	Appendix A: Description of Observatories and Data Reduction	77
A.1	Description of Amateur Observatories and Data	77
A.2	Description of University and Professional Observatories	86

Introduction

Young stellar objects (YSOs) were initially discovered by their irregular and large optical variability (Joy, 1945). Their fluxes can be affected by a wide variety of physical processes, such as changeable emission from accretion shocks, variable emission from the inner disk, and variable extinction along the line-of-sight (Carpenter et al., 2001). Furthermore, variability in YSOs occurs on a wide variety of timescales. These can range from short term accretion rate changes over minutes, to long term outburst or disk occultation events, spanning in duration from years to tens of years. Thus, observing variable young stars over a wide range of timescales and wavelengths allows us to explore the physical processes, structure and evolution of their environment, and provides key insights into the formation of stars.

Numerous photometric variability surveys have been conducted in the past, aiming to address the study of YSO variability. Often they have either focused on high cadence over relatively short periods (e.g. with COROT and Kepler (Cody et al., 2014; Ansdell et al., 2016)), or more long term, but lower cadence (e.g. with UGPS and VVV (Contreras Peña et al., 2014, 2017b)). The recently initiated HOYS project aims to perform high cadence, long-term and multi-filter optical monitoring of YSOs. It uses a combination of professional, university and amateur observatories (Froebrich et al., 2018a) to study accretion and extinction related short and long-term variability in a number of nearby young clusters and star forming regions. More detail on the project is discussed in Chapter 2.

Characterising the structure and properties of the inner accretion disks in YSOs is vital for our understanding of the accretion processes and the formation of terrestrial (inner) planets in those systems. However, investigating the innermost disk structure of YSOs on scales below 1 AU is currently only possible through indirect methods such as photometric monitoring of disk occultation events. Of particular interest are periodic, or semi-periodic, occultation events (e.g. in AA Tau (Bouvier et al., 1999) or UX Ori (Herbst and Shevchenko, 1999) type objects, though often aperiodic). They allow us to identify the physical location of the occulting structures in the disks based on the period, and therefore to determine the spatial scales of the material directly.

This thesis is organised as follows. The remainder of this Chapter gives a detailed overview of star and disk formation taken from the literature. In Chapter 2, the HOYS project is introduced; its aims, and a description of the telescope set-up. Chapter 3 explains the data obtained for the project and details the internal calibration procedure for the inhomogeneous data set. This includes the colour calibration technique, developed for the HOYS project. An analysis of the YSO, V 1490 Cyg, in Chapter 4 is then described and the implications for the nature of the source discussed in Chapter 5. Finally, all conclusions are presented in Chapter 6.

1.1 Star Formation

Low-mass star formation begins when diffuse interstellar medium (ISM) condenses, creating massive ($\sim 10^7 M_{\odot}$) bound structures resulting from gravitational instabilities. These giant molecular associations, or HI super-clouds, gain high levels of internal turbulence from the ISM. Turbulence combined with self-gravity causes fragmentation into giant molecular clouds, further developing into clumps and filaments. Initial collapse leads to the formation of the first hydrostatic core, once the central density increases to the point where the inner region becomes opaque to radiation (Larson, 1969). This renders the collapse adiabatic rather than isothermal. The short-lived, self-gravitating core (di Francesco et al., 2007) is still molecular and grows in mass by continued infall from the outer layers (Boss and Yorke, 1995; Stahler and Palla, 2005; Omukai, 2007).

As the object continues to accrete from the surrounding core, both its mass and central temperature increase with time (Ward-Thompson et al., 1999; Evans et al., 2001; Kirk et al., 2005). When the temperature reaches ~ 2000 K, molecules such as H_2 are collisionally dissociated, preventing the temperature from continuing to rise to sufficiently balance gravity. A second collapse is initiated, leading to the formation of the second hydrostatic core. The bulk of the core's material continues to surround this protostar becoming the envelope. The collapse of the core causes the system to rotate faster. The surrounding material therefore flattens and a centrifugally supported disk forms (Terebey et al., 1984). Magnetic fields, plus rotation, lead to winds and jets, driven from the surface of circumstellar disks at a range of radii (Shang et al., 2007; Pudritz et al., 2007). The inner portion of the wind, arising nearest the central star, becomes collimated into a jet-like outflow (Arce et al., 2007; Wu et al., 2004). The impact of this disk wind on the protostellar core sweeps up much of the ambient gas into a massive molecular outflow.

For a $1 M_{\odot}$ source, the first $\sim 10^5$ years are termed Class 0 sources (Andre et al., 2000) and have protostars, disks and jets, with the envelope mass being much greater than the combined disk and protostellar mass (André, 1995). Thermal emission of dust through this Class indicates a cold outer envelope and highly collimated bipolar outflows are also typically observed (Bachiller and Tafalla, 1999; Arce et al., 2007). For the next $\sim 10^{5-6}$ yr (Lada, 1987; Myers and Ladd, 1993), the central protostellar mass exceeds that of the envelope. The star and disk contribute to the thermal emission indicating a warm dust component. Outflows are typically weaker in this stage and the sources are labelled as Class I.

By Class II, the envelope has largely dispersed, but the central stars are surrounded

by a circumstellar disk. Such sources are called classical T Tauri stars (CTTS) and last for $\sim 10^{6-7}$ yr (Lada, 1987; Myers and Ladd, 1993). Emission at short wavelengths is dominated by the central protostar, while the disk emits more strongly at longer wavelengths. As this disk depletes of gas, the central object is left surrounded by a debris disk (Wyatt, 2008; Matthews et al., 2014). Such Class III objects must have already formed any planets and asteroid belts by this time (Lada, 1987; Myers and Ladd, 1993).

1.2 Disks

Due to the rotation of protostellar cores, collapse results in the formation of a centrifugally supported disk through conservation of angular momentum. Predictions, based on observations of low-mass dense cores, give disk sizes $\lesssim 1000$ AU. Similar results are obtained using sub-millimetre continuum observations and millimetre interferometry (Kitamura et al., 2002). After approximately 0.5 Myr (Evans et al., 2009), gaseous Keplerian protoplanetary disks are present at scales of between 100 – 500 AU around both low- and intermediate-mass stars (Dutrey et al., 2007; Andrews and Williams, 2007a).

Modelling suggests the inner radii of disks around T Tauri stars are at ~ 0.04 AU, showing gaseous disks extend inward to smaller radii than dust disks (Najita et al., 2007). Sublimation temperatures of dust grains ($\sim 1500 - 2000$ K) are relatively low compared to the CO dissociation temperature (~ 4000 K); the inner radius of the dust disk therefore being defined by dust sublimation (Muzerolle et al., 2003; Eisner, 2007). As protostellar systems prior to the T Tauri stage are still encompassed by dusty envelopes that emit at similar wavelengths to the disk, it can be hard to estimate initial sizes of circumstellar disks. Where it is possible for the inner envelope emission to be distinguished, disk sizes appear similar (Jorgensen et al., 2005).

Masses of protostellar disks may be estimated via millimetre and sub-millimetre wavelength observations, with total disk masses for T Tauri systems thought to be in the range of $10^{-3} - 10^{-1} M_{\odot}$, with a median near $0.005 M_{\odot}$ (Andrews and Williams, 2005). However, these estimates could be far lower than actual masses if large fractions of the grains have grown to millimetre or centimetre sizes, thus emitting only weakly in the sub-millimetre (Hartmann et al., 2006; Natta et al., 2007). Observations can be combined with modelling to suggest that the largest grains in protostellar disks are in fact centimetre-size pebbles (Wilner et al., 2005; Rodmann et al., 2006). Determining the distribution of mass within disks is difficult because sub-millimetre ALMA emission is likely to be optically thick in the inner regions, while at longer wavelengths there is insufficient resolution to probe the inner-disk regions (Andrews and Williams, 2007b). Additionally, disk mass determinations assume a constant ratio of gas to dust. At late evolutionary stages, photo-evaporation and ice formation may preferentially remove gas and planet formation may preferentially remove dust.

The thermal structure of protostellar disks is thought to be highly complex. Disks may be heated, both externally via irradiation from the central star, and internally from viscous dissipation of orbital kinetic energy as the gas accretes (Calvet et al., 1991; Chiang and Goldreich, 1997). Consequently, vertical temperature distributions may have a local minimum at intermediate altitudes (D’Alessio et al., 1998); flaring of the disk’s sur-

face affects the amount of radiation intercepted from the central star (Dullemond et al., 2007). Additionally, gas and dust temperatures may differ in the upper atmospheres where the densities are low and stellar X-rays strongly heat the gas (Najita et al., 2007). Models have been developed (D’Alessio et al., 2006; Dullemond et al., 2007) indicating that although some grains have grown to large sizes, small grains still remain in disk atmospheres (Dullemond et al., 2007; Natta et al., 2007).

Observations of IC 348 show that for $\sim 70\%$ of stars, disks have become optically thin in the infrared, implying inner disks with $R \lesssim 20$ AU have been removed within the 2 – 3 Myr age of the system (Lada et al., 2006). Observations of other clusters are consistent with these results (Sicilia-Aguilar et al., 2006a). For clusters spanning a range of ages, Haisch et al. (2001) suggests that overall disk lifetimes are ≈ 6 Myr. Even in the 10 Myr old cluster NCG 7160, a small percentage of stars still show signs of disks (Sicilia-Aguilar et al., 2006a), and disk lifetimes appear to be inversely correlated with the mass of the star (Hernández et al., 2007). The presence of dusty disk emission is well correlated with evidence of accretion in gaseous emission line profiles, indicating that gas and dust disks have similar lifetimes (Jayawardhana et al., 2006; Sicilia-Aguilar et al., 2006b). Andrews and Williams (2005) conclude that inner and outer disk lifetimes agree within 10^5 yr.

Accretion in YSOs shows gas is falling onto the stellar surface along magnetic field lines (Calvet et al., 2000). Gullbring et al. (1998) measured an accretion rate for Myr old T Tauri stars of $\sim 10^{-8} M_{\odot} \text{ yr}^{-1}$, and White and Ghez (2001) found similar accretion rates for the primary T Tauri stars in binary systems. A compilation of observations (White and Basri, 2003; Muzerolle et al., 2003; Calvet et al., 2004) show the accretion rate depends on stellar mass. During their embedded stages (a few 10^5 yr), low-mass stars have typical disk accretion rates similar to, or slightly larger, than those of CTTS (White et al., 2007). Infall rates from protostellar envelopes typically exceed disk accretion rates by a factor 10 – 100, so it is possible that mass is stored in the disk and released intermittently in brief, but prodigious, accretion events similar to FU Ori outbursts (Kenyon et al., 1990; Hartmann and Kenyon, 1996).

1.3 Planet Formation

Most of a protostellar disk’s mass is accreted during the first 10^5 years. This correlates strongly with intense outflow activity, and it is during this phase that the formation of the planetary system begins. In distant regions of massive disks, giant planet formation may occur through rapid, driven fragmentation, gravitationally caused (Mayer et al., 2002; Rafikov, 2009). Another cause is accretion over Myr timescales of massive gaseous envelopes on rocky planetary cores (Pollack et al., 1996; Helled et al., 2014). The disk becomes excited and perturbed, caused by the appearance of the giant planets; with collisions consequently forming terrestrial planets within the disk (Raymond et al., 2014).

A disk’s mass affects both star and planet formation. The central star accretes most of its mass through its disk, whilst the giant planets must compete for gas from the same supply. Early disk masses exceeding $0.01 M_{\odot}$ provide a sufficient gas supply to quickly

form Jovian planets (Weidenschilling, 1977). For disks with mass $\sim 0.1 M_{\odot}$, strong spiral waves can be generated, driving rapid accretion onto the central star (Arzamasskiy and Rafikov, 2018). These waves may be prone to fragmentation.

As discussed, protostellar disk's lifetimes are known to be in the range of 3 – 10 Myr. For gas disks around stars of less than $2 M_{\odot}$, 80 % has dissipated by 5 Myr after their formation (Carpenter et al., 2006; Hernández et al., 2008, 2010), suggesting massive planet formation must therefore occur during this time.

Protostellar outflows occur early on in star formation. They are seen in Class 0 sources, which implies that magnetised disks are also present at these early stages (Arce et al., 2007). These outflows are launched due to the magnetic fields that pass through the disk. The fields also having a strong stabilising effect on the fragmentation of disks.

Simulations by Seifried et al. (2012) suggest within the first few 10^4 years, launching of centrifugally driven jets grows more efficient through the disk becoming Keplerian. Prior to this, angular momentum transport through spiral waves could be the more dominant mode.

Rocky planetary cores ($\sim 10 M_{\oplus}$) are required for the core accretion method of generating giant planets taking place during the early disk phase (Johansen et al., 2014). This allows time for the accretion of a gas envelope around such cores. Gas lifetime in the inner disk provides an upper time limit for giant planet formation (Zuckerman et al., 1995). This age is limited by accretion onto the star and photo-evaporation. Generation of planetesimals from which giant cores are created must, therefore, begin at an even earlier time.

Over 10^5 yr, forming planetary cores undergo rapid migration through the disk (Ida and Lin, 2008; Benz et al., 2014). This movement occurs through the exchange of angular momentum between the planet's orbit and the gaseous disk by means of Lindblad and co-rotation resonances (Tanaka et al., 2002). The migration may be slowed by planet traps: regions within the disk of zero net torque acting upon the planet (Masset et al., 2006; Matsumura et al., 2009; Hasegawa and Pudritz, 2011, 2012). Narrow, dead zones are also formed within the disk where growing planets can be trapped. Such zones arise from inhomogeneities in disks, ice lines, and heat transition regions, arising from viscous disk heating to stellar irradiation domination.

1.4 Variable Young Stars

Observations of variable young stars allow us to explore the structure and evolution of the environment surrounding YSOs, providing a key insight into star formation. As multiple causes of variability occur simultaneously, observed light curves may be very complex to interpret. Several prototypical stars have however been identified as corresponding to different physical causes.

Classical T Tauri stars (CTTS), named after the first star of their class to be identified (located in Taurus), are young ($\sim 1 - 10$ Myr), low-mass ($< 2 M_{\odot}$) stars surrounded by a circumstellar disk from which they accrete. They are characterised by unusual

spectral features, such as high H and K luminosities, and by large, and fairly rapid, irregular variations in luminosity, with timescales on the order of days. Their magnetic fields are strong enough to truncate the inner disks and channel the accreting gas. These systems also produce outflows in the form of stellar and disk winds that may collimate in a jet (Bouvier et al., 1986; Hartmann et al., 2016). At about the same ages T Tauri stars that are no longer, or are slowly accreting, are called weak-line T Tauri stars (WTTS). Such low-mass, pre-main-sequence (PMS), objects represent a transition between stars that are still shrouded in dust and main sequence stars.

FU Ori and EX Lupi, possibly a short timescale counterpart, are prototypes for stars with strong, long-lived optical outbursts, caused by sharp increases in their mass accretion rates (Audard et al., 2014). This accretion may reach values on the order of $10^{-4} M_{\odot} \text{ yr}^{-1}$, lasting over decades. The phenomenon is now known to occur on a wide range of timescales within some T Tauri stars (Stauffer et al., 2016), including objects with continuous accretion rate changes and, therefore, highly stochastic light-curves (Stauffer et al., 2014, 2016). Stars that behave similarly have been dubbed FUors (Herbig, 1966, 1977) and EXors (Herbig, 1989) respectively, with a third category of MNors suggested in Contreras Peña et al. (2017a).

Instabilities in the circumstellar accretion disk around an FUor/EXor star can result in a mass $\sim 0.01 M_{\odot}$ being deposited onto the central star over the duration of the outburst. During that time, the inner-disk can become 100 to 1000 times more luminous than the central star whilst strong, high-velocity winds occur (Croswell et al., 1987). It has been suggested that T Tauri stars may exhibit several of these outbursting events during their lifetimes. Recent studies have indicated separate observational classification of FUors and EXors are not needed, as discoveries of new outbursting sources have resulted in a less definitive separation, and the outburst might lie on a spectrum (Contreras Peña et al., 2017a; Contreras Peña et al., 2019).

Dimming events could indicate temporary eclipsing of the central young star by portions of the inner disk, warped by the star's magnetic field (Bouvier et al., 1986; McGinnis et al., 2015). The first star identified to exhibit this behaviour was AA Tau (Bouvier et al., 2014) and stars with similar light curves are now classified as 'dippers'. The UX Ori (UXor) phenomenon of Herbig Ae/Be (HAeBe) stars is attributed to obscuration by circumstellar dust in an inclined disk (Grinin et al., 1994; Natta et al., 1997; Grinin et al., 2001; Dullemond et al., 2003), unsteady accretion (Herbst and Shevchenko, 1999), or cloudlets (Natta et al., 2000).

HAeBe stars were originally identified by Herbig (1960) as potential high mass equivalents to T Tauri stars. They are pre-main-sequence stars with masses of $2 M_{\odot}$ or larger (Strom et al., 1972; Hillenbrand et al., 1992; The et al., 1994). Photometric variations of T Tauri stars can be divided into three types (Herbst et al., 1994). Type I variations arise from the rotation of a star with large cool spots and Type II variations are caused by changes in the observed pattern of hot accretion spots on a star's surface due to unsteady accretion and stellar rotation. Type III variables (UXors seen in Herbst et al. (1994)) and HAeBe stars are less clearly defined. It is observed that the inner circumstellar environment in more massive PMS stars differ from those in CTTSs by the nature of their variability.

WTTS display only Type I variations. Due to the stability of their large cool spots

on timescales of months to years (Grankin, 1994), photometric monitoring allows for rotation periods to be obtained (Rydgren et al., 1983; Bouvier et al., 1986; Grankin, 1994; Choi and Herbst, 1996). CTTS display both Type I and Type II variations. The timescale for intrinsic changes in the hot spots can be less than, or similar to, a rotation period, making it more difficult to determine rotation periods for CTTS (Bouvier et al., 1993). The timescale of variations are longer in Type III variables and there can be more variation in V, R, and I.

Erupting young stars are considered crucial to understanding star formation and the time evolution of mass accretion rates, from embedded protostars to CTTS, and eventually WTTS. Nevertheless, despite study and classification, many of the variable young stars discovered do not seem to strictly conform to set categories. Whilst the physics, detailing accretion bursts and their variation, is still under debate, the episodic nature of accretion is now considered by some to be a defining characteristic of early stellar evolution.

HOYS

2.1 The Project

HOYS¹ is an ongoing citizen-science project run by the University of Kent since October 2014. The acronym stands for Hunting Outbursting Young Stars. It currently involves a network of amateur telescopes, several University observatories, as well as other professional telescopes. These are distributed across 10 different countries throughout Europe in addition to sites in the U.S. For a full list of observatories used to collect the data presented in this thesis, see Appendix A.

The project aims to combine data from various geographical locations for long term, multi-filter, optical photometric monitoring of young stellar clusters. This allows for the discovery of outbursting objects for detailed follow-up study. Such analysis may, in part, be carried out using the high cadence sampling achieved by the project. Targets are young, nearby, star clusters or star forming regions with ages less than 10 Myr. They are typically at distances within 1 kpc. Every target is visible from the Northern hemisphere through use of small telescopes, and the full list is below in Chapter 2.3.

All data presented in this thesis has been obtained for the HOYS project (Froebrich et al., 2018a). At the time of writing, the project had 56 participants submitting data, in several cases from multiple amateur observers or multiple telescopes/observing sites. In total approximately 12,500 images have been gathered. In those, ≈ 95 million reliable photometric measurements have been obtained for stars in all of the 22 HOYS target regions. Participants are free to observe and image any object from a target list and submit them into the HOYS database through a dedicated web-interface².

To aid in the submission and processing of data for all participants, an online portal was developed by Will Furnell. He wrote the website using the Django³ web frame-

¹<http://astro.kent.ac.uk/~df/hoyscaps/index.html>

²<http://astro.kent.ac.uk/HOYS-CAPS/>

³<https://www.djangoproject.com/>

work with Django ORM being used for managing the MariaDB database⁴. All processed data are automatically added to this database giving users and the public the ability to plot and download light curves⁵ for all objects observed.

No restrictions are given to participants regarding target, cadence, field of view, filter selection or integration times. This allows for random sampling of the target fields when combined in the database. Basic data reduction is supposed to be performed on all images before submission, including dark/bias and flat-field corrections.

2.2 The Beacon Observatory

Approximately 50% of the data taken for the HOYS project were supplied by the Beacon Observatory. The Beacon Observatory⁶ is located at the University of Kent (51.296633° North, 1.053267° East, 69 m elevation). It consists of a 17" Planewave Corrected Dall-Kirkham (CDK) Astrograph telescope inside a 3.5 m diameter Baader All-Sky Dome allowing for a 360° field of view. The telescope is equipped with a 4k × 4k Peltier-cooled CCD camera and a B, V, R_c, I_c, H_α filter set. The pixel scale of the detector is 0.956", giving the camera a field of view of just over 1° × 1°. As the corners of the detector are vignettted, the usable field of view is a circle of diameter ~ 1°. A GM3000HPS Equatorial German Mount allows for full tracking capability.

Images taken by Beacon for HOYS are typically 8 sets of 120 s integrations in V, R_c, and I_c. This sequence takes approximately one hour, including filter changes and CCD readout. All images are individually dark and bias subtracted. Polar sky-flats are then used for flat-fielding of the images. The Montage software package⁷ is then used to median average multiple images of a common target and filter.

At the start of the night, polar sky-flats are obtained by pointing the telescope at a Declination of 88° and a random Right Ascension angle. As soon as the number of counts at the centre of the CCD fall below 50,000 in a one second exposure, a one second flat-field is taken. The telescope is then moved by 2 hrs in RA (plus or minus) and the next one second flat-field is taken. By continuing this procedure in the same direction in RA until twelve polar sky-flats have been obtained, the data reduction pipeline combines all flat-fields together. Polar sky-flats are taken for each filter. This removes the background gradient in the flat-field images.

For more information on the equipment at the observatory, the User Manual may be obtained under 'Documents' from the associated Beacon website⁸.

⁴<https://mariadb.org/>

⁵<http://astro.kent.ac.uk/HOYS-CAPS/lightcurve/>

⁶http://astro.kent.ac.uk/Beacon_observatory/index.html

⁷<http://montage.ipac.caltech.edu/>

⁸http://astro.kent.ac.uk/Beacon_observatory/documents/index.html

Table 2.1: List of winter targets with their location in Right Ascension and Declination (J2000) epoch.

Number	Cluster/Region Name	RA (J2000)	DEC (J2000)
001	NGC 1333	03 29 02	+31 20 54
002	IC 348	03 44 34	+32 09 48
003	M42	05 35 17	-05 23 28
004	NGC 2264	06 40 58	+09 53 42
005	Sigma-Ori Cluster	05 38 45	-02 36 00
006	Lambda-Ori Cluster	05 35 06	+09 56 00
007	L 1641 N Cluster	05 36 19	-06 22 12
008	NGC 2244	06 31 55	+04 56 30
009	NGC 2068	05 46 46	+00 04 12

Table 2.2: List of summer targets with their location in Right Ascension and Declination (J2000) epoch.

Number	Cluster/Region Name	RA (J2000)	DEC (J2000)
110	Berkeley 86	20 20 12	+38 41 24
111	P Cyg	20 17 47	+38 01 59
112	MWSC 3274	20 11 13	+37 27 00
114	IC 1396 N	21 40 42	+58 16 06
115	IC 1396 A	21 36 35	+57 30 36
116	NGC 7129	21 42 56	+66 06 12
118	IC 5070	20 51 00	+44 22 00
119	IC 5146	21 53 29	+47 16 01

2.3 Targets

Target regions are separated into three categories: winter, summer and Gaia variable objects. Winter and summer targets are shown in Tables 2.1 and 2.2 whilst Gaia variables are taken from the Gaia Photometric Alerts list ⁹. These categories can be distinguished through the HOYS target numbering system; each three digit numbers starting with 0, 1 and 2 respectively.

At time of writing, there are 9 Gaia targets currently being monitored by the HOYS project, including an FU Ori out-bursting object (Hillenbrand et al., 2018). Some of the Gaia objects are already observable within summer or winter fields. Therefore this does not often conflict with time spent observing the main HOYS regions.

⁹<http://gsaweb.ast.cam.ac.uk/alerts/alertsindex>

Observational Data and Photometric Calibration

3.1 V 1490 Cyg Imaging Observations

In this thesis, the data for the star V 1490 Cyg is analysed, which is situated in the Pelican Nebula, or IC 5070, corresponding to HOYS target number 118. At the time of writing, a total of 85, 419, 1134, 932, 249, and 755 images in the U, B, V, R_c , H_α and I_c filters have been gathered, respectively for this target field. The target itself has sufficient quality data (magnitude uncertainty smaller than 0.2 mag) in 3321 images from 44 different users and 66 different imaging devices - see Chapter 3.2.2 for details. A full description of the observatories, the equipment used, the typical observing conditions and patterns, as well as data reduction procedures is given in Appendix A. All HOYS observations included in the paper for V 1490 Cyg have been taken over the last 4 years.

All of the data used for this thesis has been collected for the HOYS project, which, as discussed previously in Chapter 2.1, combines data-sets obtained by a large network of telescopes, amateur and professional, as well as several University observatories. This leads to the usage of a wide variety of different filters which needs to be accounted for during the photometric calibration process. Thus, the data are calibrated in a two-step process.

3.2 Photometry Data Calibration

The basic relative data calibration for all of the HOYS data, developed by and summarised in Chapter 2.4 of Froebrich et al. (2018a), will now be described below.

Table 3.1: List of internal flags generated by the Source Extractor software.

Flag	Description
0	No error in the photometry.
1	The object has neighbours, bright and close enough to significantly bias the MAG AUTO photometry, or bad pixels (more than 10% of the integrated area affected).
2	The object was originally blended with another one.
4	At least one pixel of the object is saturated (or very close to).
8	The object is truncated (too close to an image boundary).
16	Object's aperture data are incomplete or corrupted.
32	Object's isophotal data are incomplete or corrupted.
64	A memory overflow occurred during deblending.
128	A memory overflow occurred during extraction.

Images may be submitted to the HOYS database server¹ by participating observers. They then indicate for each image which target region and telescope/detector combination has been used. The date/time, exposure time, and filter meta-data is then extracted from the FITS header and, using the Astrometry.net² software (Hogg et al., 2008), the image coordinate system is accurately determined.

3.2.1 Basic Relative Photometric Calibration

The initial photometric calibration process is carried out on the data before it is submitted to the HOYS database. The Source Extractor³ software (Bertin and Arnouts, 1996) is used to perform aperture photometry for all images. The software provides flags with basic warnings about the source extraction process, in order of increasing concern.

A flag of 0 would indicate no error in the photometry, whereas a flag of 4 warns that at least one object pixel is saturated. These flags are given as powers of 2, allowing the user to determine if a measurement has multiple associated flags as the resultant flag would be a sum of lesser flag values. The full description of the software and the resulting flags can be read in the Source Extractor documentation. For the calibration process, flags less than 5 are deemed acceptable for reliable photometry; any data with higher flags are not used.

In addition to flags provided by the Source Extractor software, four new flags have been added during the calibration process to indicate potential problems with the data. These flags of 256, 512, 1024 and 2048 will be described further in this chapter as they are introduced into the correction procedure (see Chapter 3.2.2 for flag 2048).

For each region and filter a deep image obtained under photometric conditions has been chosen as a reference image. The U-band reference frames are from the Thüringer

¹<http://astro.kent.ac.uk/HOYS-CAPS/>

²<http://nova.astrometry.net/>

³<https://www.astromatic.net/software/sextractor>

Landessternwarte (see Appendix A.2), while all the other reference images (B, V, R_c, I_c) are from the Beacon Observatory (see Appendix A.2). Offsets for the calibration were determined into apparent magnitudes for each of the reference images through use of the Cambridge Photometric Calibration Server⁴, set-up for Gaia follow-up photometry.

The magnitude dependent calibration offsets $f(m_i)$ between all images and the reference frames have been obtained by fitting a photo-function and 4th order polynomial (Moffat, 1969; Bacher et al., 2005) to matching stars with accurate photometry. Fitting was achieved through use of least-squares optimisation.

$$f(m_i) = A \cdot \log(10^{B \cdot (m_i - C)} + 1) + \mathcal{P}_4(m_i) \quad (3.1)$$

Figure 3.1 shows an example of how the calibration works on data taken from an image of IC 5070. The observation was made with a green (TG) filter at the Seltztal-Observatory and is calibrated into the V-band reference image for the IC 5070 region.

Stars brighter than the left-most vertical solid line in Fig. 3.1 had their flags increased by the new flag 256, and stars fainter than the right-most vertical solid line increased by 512. These additions were made to identify, and remove, any stars in each image with magnitudes outside the calibration range as Eq. 3.1 will potentially be invalid. Additionally, the flag is increased by 1048 if there are any other problems with this basic photometric calibration.

Note that all H_α images are calibrated against the R_c-band reference images. Typically the accuracy of this basic relative calibration ranges from a few percent for the brighter stars, to 0.20 mag for the faintest detected stars, depending on the observatory, filter, exposure time and observing conditions.

3.2.2 Photometry Colour Correction

In Froebrich et al. (2018a), analysis was limited to data taken either with the Beacon Observatory, or data taken in the same filters. Now, with a much larger fraction of amateur data using a variety of slightly different filters, in particular from DSLR cameras, the calibration of the photometry needs to consider colour terms. Hence, a way was required to internally calibrate the photometry in the database. The flowchart shown in Fig. 3.2 outlines the general steps of the correction process which are explained in detail below.

The correction procedure assumes that non-variable stars, found in each target region, do not change their brightness over time. Hence these stars do have a known magnitude and colour. By comparing the photometry of these stars in an image, after the basic relative calibration, to their known brightness, any difference can be attributed to colour-terms in that particular image. These may be caused either by varying filter transmission profiles from the range of filters used, differing sensitivity curves of the detectors, or by the observing conditions (e.g. thin/thick cirrus). These colour-terms

⁴<http://gsaweb.ast.cam.ac.uk/followup>

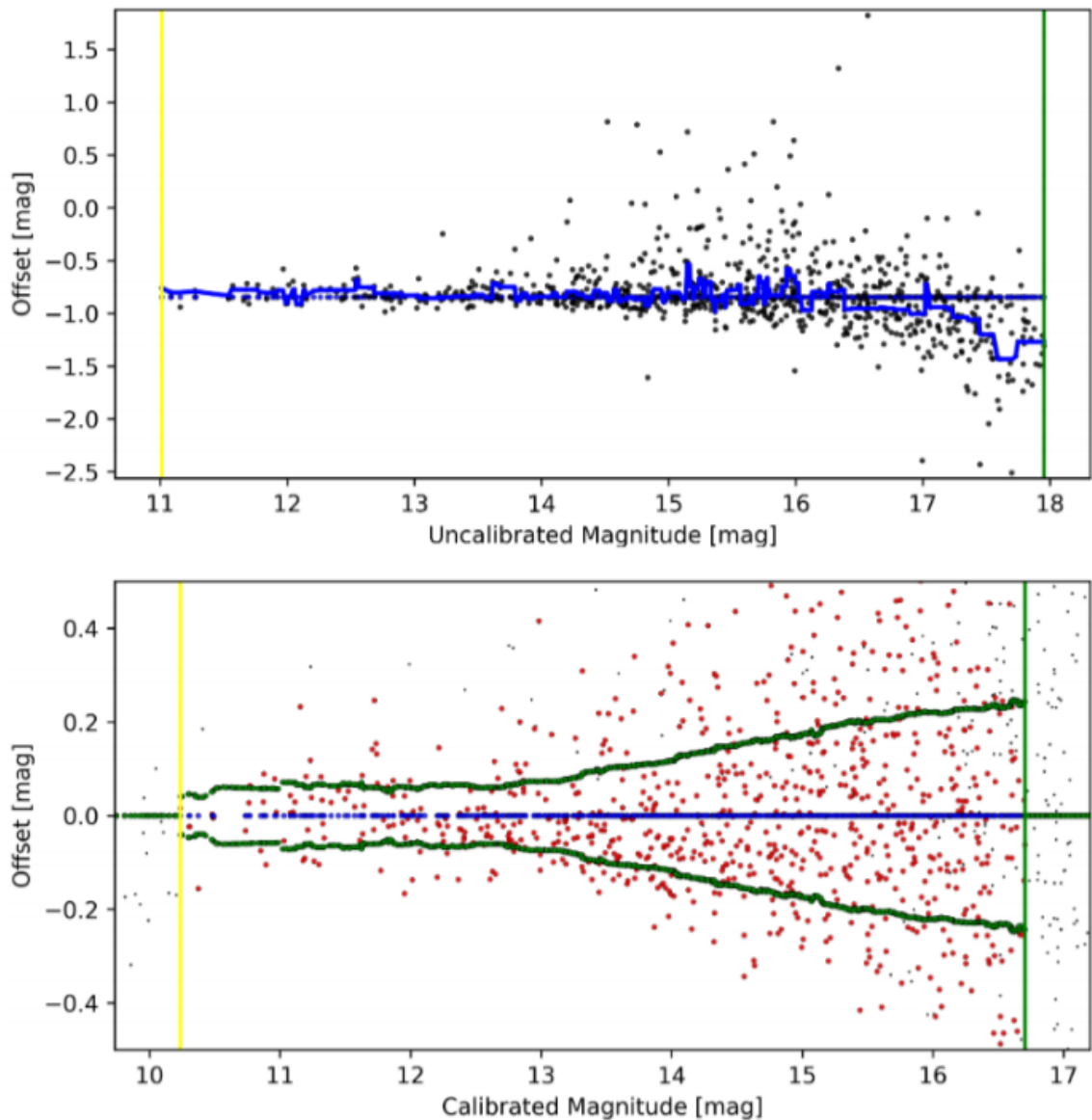


Figure 3.1: Calibration of an image of IC 5070 from a green (TG) filter into the V filter. **Left panel:** Difference ($m_i - m_r$) of the instrumental magnitudes between the TG image and the V-band reference data set. The running median is indicated by a line through the data-points and the two vertical lines show the range of instrumental magnitudes considered. **Right panel:** Difference ($m - m_r$) between the calibrated TG data and the V-band reference frame. Larger dots indicate stars with no problems in the photometry (flag of 0), while the remaining stars are shown as smaller dots. Lines above and below zero indicate the one sigma scatter for stars within 0.5 mag bins and the two vertical lines show the range of magnitudes in which stars are included in the calibration.

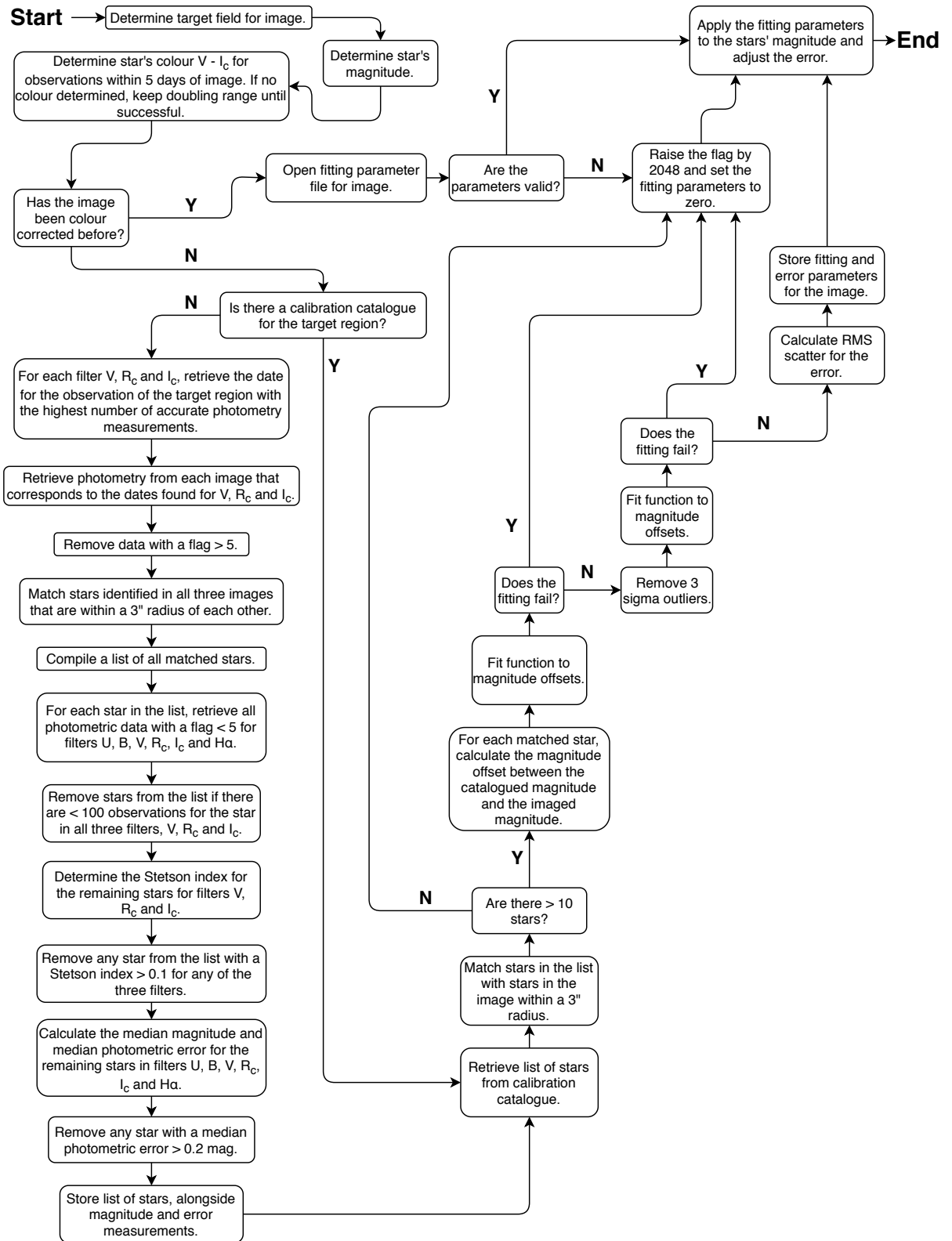


Figure 3.2: Flowchart detailing the colour correction process of the HOYS photometry on a given star in a given image.

can therefore be corrected for, further removing any systematic errors potentially introduced during the basic calibration step. Thus, a reliable catalogue of non-variable stars is needed for each HOYS target region.

Identifying Non-Variable Stars

For each target region, and V, R_c, I_c filters, the image with the largest number of accurately measured (Source Extractor flag less than 5 – see Bertin and Arnouts (1996) for details) and calibrated magnitudes was identified. All stars in these images that are detected in all three filters (matched within a 3'' radius) are selected to generate a master list of stars for the region in the HOYS database. For all selected stars, the accurately measured photometry in all filters (U, B, V, R_c, H_α, I_c) is extracted. All stars with less than 100 data-points in V, R_c, and I_c are removed. The Stetson index, \mathcal{I} , was then determined for the V, R_c, and I_c data.

The Stetson variability index, \mathcal{I} , developed by Welch and Stetson (1993), indicates the degree to which n quasi-simultaneous pairs of measurements obtained in two different filters are correlated. Assuming that a star's light curve consists of pairs of measurements obtained closely in time when compared to the expected variability time-scale, the Stetson index, \mathcal{I} , may be calculated for a single filter (Stetson, 1996).

$$\mathcal{I} = \frac{\sum_{k=1}^n \text{sgn}(P_k) \sqrt{|P_k|}}{n} \quad (3.2)$$

Equations 3.2 - 3.4 govern this, where n is the total number of observations in the filter, m_k is the k^{th} magnitude in the filter, \bar{m} is the mean magnitude in the filter, $\sigma_{m,k}$ is the calibrated magnitude error in the filter for the k^{th} measurement and $\text{sgn}()$ indicates whether the term is positive or negative.

$$P_k = \delta_k^2 - 1 \quad (3.3)$$

$$\delta_k = \sqrt{\frac{n}{n-1}} \left(\frac{m_k - \bar{m}}{\sigma_{m,k}} \right) \quad (3.4)$$

Figure 3.3 shows the Stetson index for V plotted against visual calibrated magnitude, for all stars within the target region of IC 5070. For the purpose of this thesis, all stars with a Stetson index of less than 0.1 in all three filters (V, R_c, I_c) were selected as non-variable. For all these stars, the median magnitudes and colours were determined in all of the filters (U, B, V, R_c, H_α, I_c) as reference brightness for the subsequent calibration. The Stetson index cut is a compromise between selecting only the most non-variable sources, while ensuring that images with small fields of view contain a sufficient number of these calibration stars.

As can be seen in Fig. 3.3 there is a slight upward trend of the Stetson index in V for fainter stars, which is also seen in the R_c and I_c filters. This is caused by a small under-

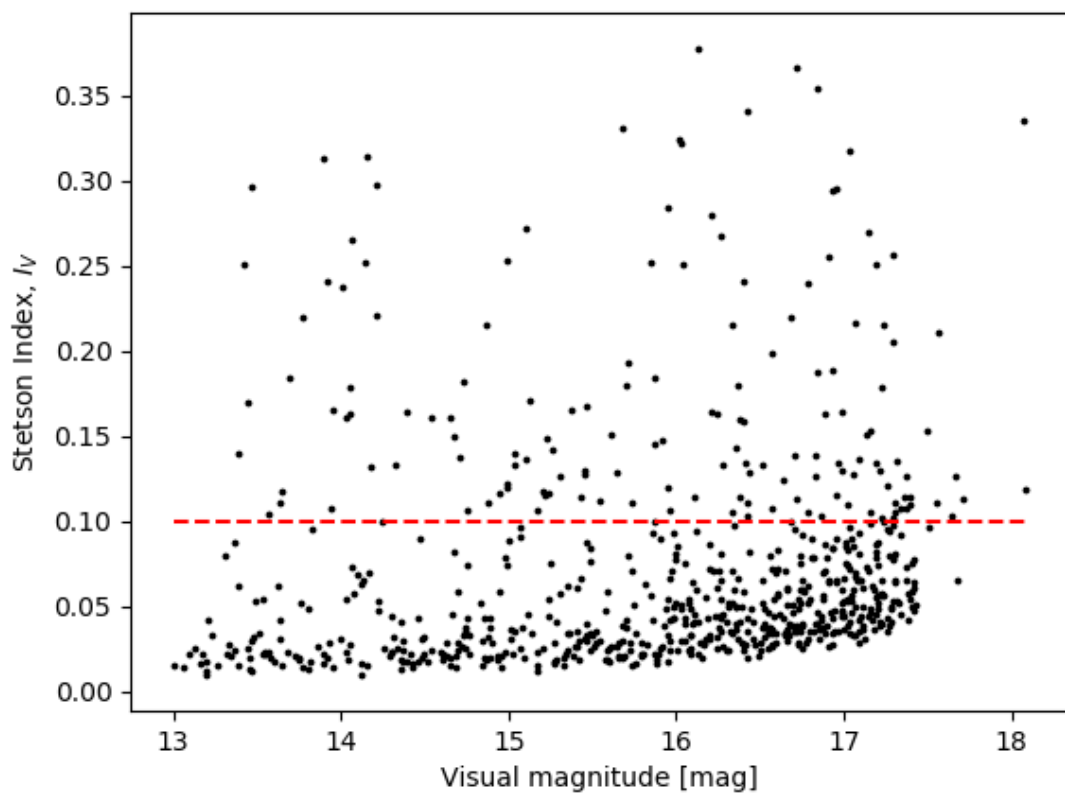


Figure 3.3: Stetson variability index, I_V , against visual magnitude for all stars within the HOYS target region IC 5070. The red dashed line shows the cut made, below which stars were deemed to be non-variable.

estimation of the photometric uncertainties for the fainter stars during the basic photometric calibration due to images having different limiting magnitudes. The effect is, however, very small and thus has no significant impact on the selection of non-variable sources.

Colour Correction

To remove any systematic magnitude offset caused by colour-terms, a unique function $\mathcal{W}_N(m, c)$ is determined for each image (N). Here c is the colour of the stars in the image, with m the stars' calibrated magnitudes for the filter that each image is calibrated into. For the purpose of this thesis, the colour $V - I_c$ is used. However, any other colour may be chosen providing the star is detectable in the corresponding filters. The functional form of the correction factor used is a simple 2nd order polynomial, for both magnitude and colour, with no mixed terms and a common offset p_0 , i.e.:

$$\mathcal{W}_N(m, V - I_c) = p_0 + \mathcal{P}_1^2(m) + \mathcal{P}_2^2(V - I_c), \quad (3.5)$$

where \mathcal{P}^2 represents a second order polynomial without the constant term. Thus, there are the five free parameters to determine for the correction function $\mathcal{W}_N(m, c)$. Hence, all non-variable stars detected (with Source Extractor flag less than 5) in image N are identified and the difference determined between their magnitude and their real magnitude. Any stars that show a magnitude difference of more than ± 0.5 mag and whose magnitude uncertainty is bigger than 0.2 mag are removed. This is needed as in particular in U, but also in H_α , stars selected as non-variable in V, R_c , and I_c can change their brightness, as many of them are young sources. At least 10 non-variable stars are required to be present in the image. A least-square optimisation of these magnitude differences is then performed to determine the required parameters. Since there are typically many more fainter than brighter non-variable stars in the images, a magnitude m_i dependent weighting w_i factor is introduced for each star i during the fitting process that is determined as:

$$w_i = \frac{1}{(m_i - \min(m_i) - 2)^2} \quad (3.6)$$

Here $\min(m_i)$ represents the magnitude of the brightest star included in the fitting process. This is the same weighting factor that is used when fitting the photo function and 4th order polynomial during the basic data calibration in Chapter 3.2.1. This gives brighter stars a larger weight during the optimisation. To ensure the fit is not influenced by misidentified, or newly variable stars, the fitting is done using a three-sigma clipping process. Figures 3.4 and 3.5 show four examples of how the fitting process reliably removes any systematic colour and magnitude dependent photometry offsets.

These examples come from different users with unique telescope and detector combinations. The top four panels of Figure 3.4 are of a B-filter image (fits_id 4765), taken by the Beacon Observatory. The bottom four panels show V-filter images (fits_id 4765), taken by the Beacon Observatory. The top four panels of Figure 3.5 are of an R_c -filter

image with fits_id 4765, taken by user 41. The bottom four panels show an I_c -filter image with fits_id 4765, taken by user 16.

To correct the magnitude m_i of a particular star, i , in image N using the determined parameters of $\mathcal{W}_N(m, V - I_c)$, the colour of the star must be known at the time of the observation for image N . The median magnitude in V and I_c is determined from all images taken within ± 5 days of the observation date to estimate the colour. If there is insufficient data, the time range is doubled until a value is found. As one can see in Fig. 3.4 the colour dependence of the correction is quite weak. Therefore, estimating the star's colour from the uncorrected photometry will not introduce any large systematic offsets; the majority of the data has been obtained using filters that do have a very small colour-term.

The calibration procedure is used to estimate a more representative uncertainty for the photometry after the correction of systematic offsets. Uncertainty is here defined as the RMS scatter of the magnitude offsets of all calibration stars in the image which have the same magnitude (within ± 0.1 mag) as the star in question. If there are less than 10 calibration stars in that range, the magnitude range is increased until there are at least 10 calibration stars from which the RMS can be estimated.

The above described colour correction procedure only fails for 181 of the 3513 images when applied to the data of V 1490 Cyg, to which their internal flags are raised by 2048. The typical median calibrated magnitude uncertainties for U and H_α filters are 0.08 mag and 0.09 mag, respectively. This decreases to about 0.02 mag for the B, V, R_c , and I_c filters. Figure 3.6 shows histograms of all calibrated magnitude uncertainties that are less than 0.2 mag for each filter. The black line over-plotted is the cumulative frequency distribution of the same data, showing that roughly 80 % of the uncertainties in the broad-band filters are less than 0.04 mag.

The entire analysis presented in this thesis has been conducted using the colour corrected light curve for all data submitted and processed in the HOYS database before September 1st 2019. It excludes any measurement with a higher than 0.2 mag photometric uncertainty after the colour correction procedure.

3.3 Spectroscopy Data

From 1st August to 15th September in 2018, HOYS observations were coordinated in a high cadence photometric monitoring campaign of V 1490 Cyg in order to monitor the short term variability of the source. In support of this campaign, an attempt was made to obtain optical spectra of the source every five days. This utilised the FLOYDS spectrograph (Sand, 2014) on the 2 m LCOGT telescope on Haleakala in Hawaii. It has a resolution between $R = 400$ (blue) and $R = 700$ (red) and covers a wavelength range from 320 nm – 1000 nm. Due to weather, observations were carried out only on six nights during the above-mentioned period. During each observing night, 3×600 s exposures of the target were taken, using a slit width of $1.2''$.

The pipeline reduced spectra were utilised and downloaded from the LCOGT archive. All spectra taken in the same night are averaged. The only feature visible in all the

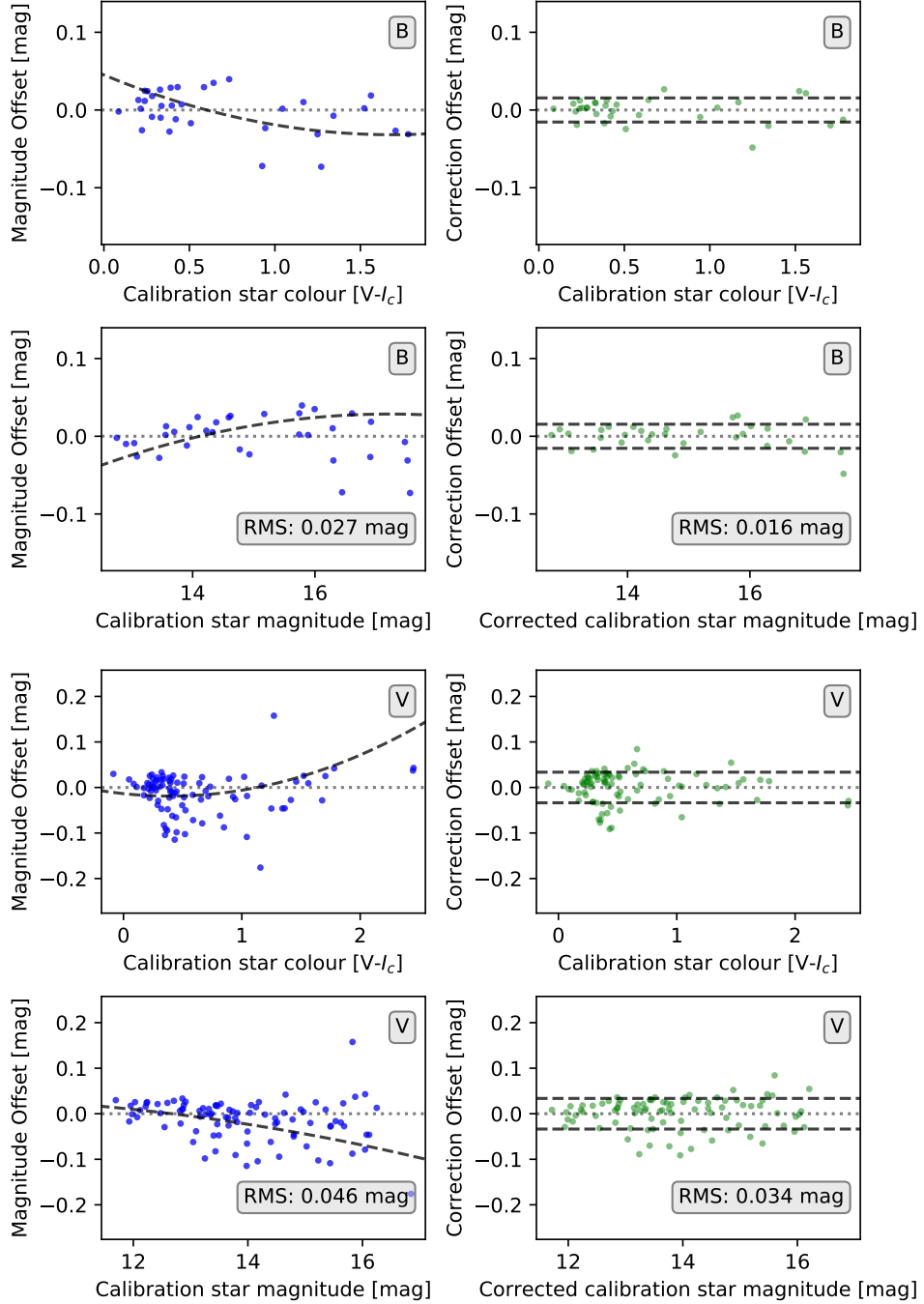


Figure 3.4: Example correction plots for two images in B (top) and V (bottom). The B and V examples show very small colour-terms, compared to the R_c and I_c images in 3.5. In both figures there are four panels. **Top Left:** The dots show the offset calculated for each calibration star against their median colour ($V - I_c$). The dashed line shows $\mathcal{W}_N(m, V - I_c)$ for the median magnitude of the calibration stars. **Bottom left:** The dots show the offset calculated for each calibration star against their magnitudes. The dashed line shows $\mathcal{W}_N(m, V - I_c)$ for the median colour of the calibration stars. **Top right:** The dots show the corrected off-sets for the calibration stars against their colour. **Bottom right:** The dots show the corrected off-sets for the calibration stars against their magnitudes. All sigma-clipped stars are removed from the right panels. The dashed lines in the right panels indicate the RMS scatter after the correction.

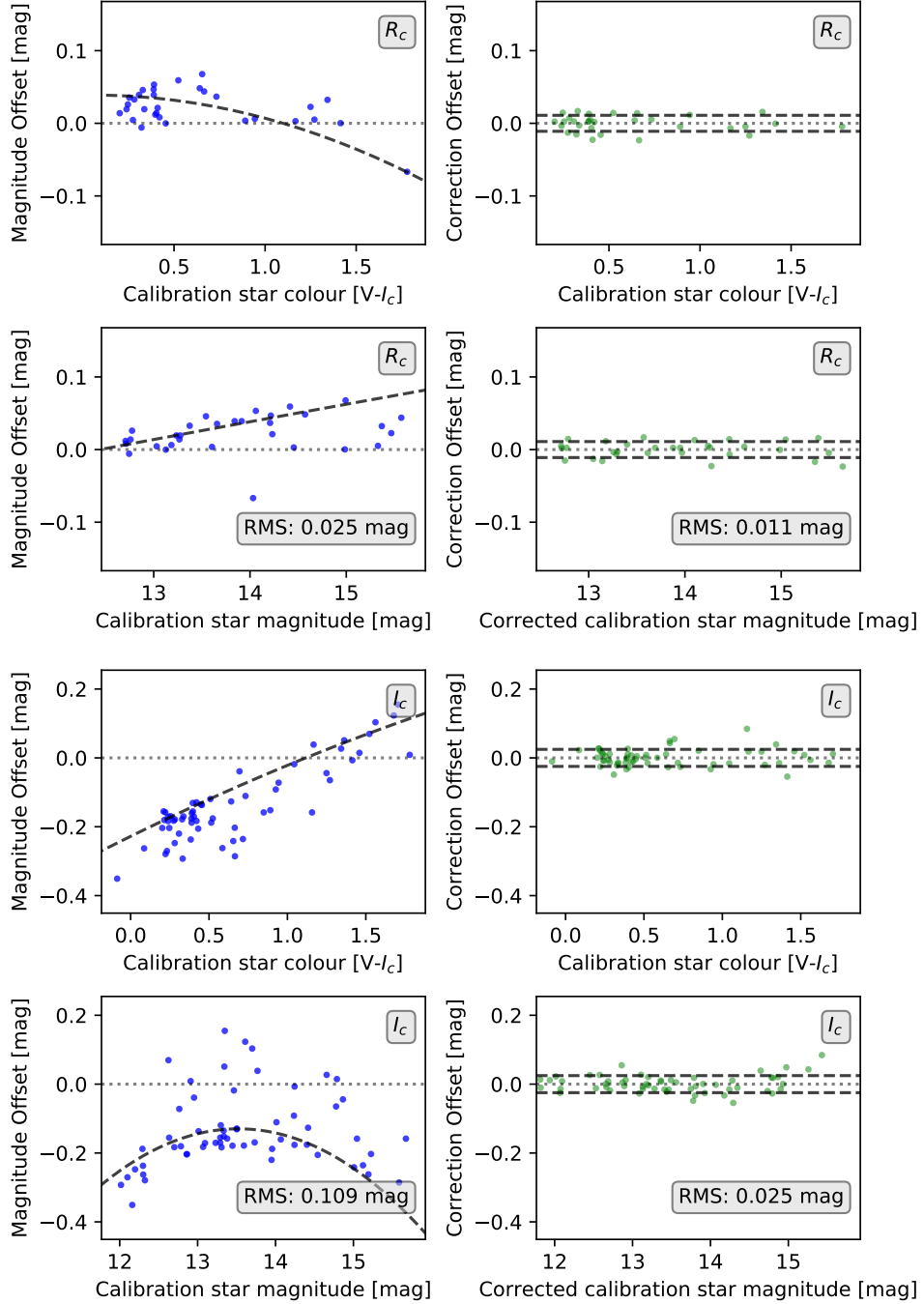


Figure 3.5: Example correction plots for two images in R_c (top), and I_c (bottom). The R_c and I_c images represent some of the largest colour terms present in the data. In both figures there are four panels. **Top Left:** The dots show the offset calculated for each calibration star against their median colour ($V - I_c$). The dashed line shows $\mathcal{W}_N(m, V - I_c)$ for the median magnitude of the calibration stars. **Bottom left:** The dots show the offset calculated for each calibration star against their magnitudes. The dashed line shows $\mathcal{W}_N(m, V - I_c)$ for the median colour of the calibration stars. **Top right:** The dots show the corrected off-sets for the calibration stars against their colour. **Bottom right:** The dots show the corrected off-sets for the calibration stars against their magnitudes. All sigma-clipped stars are removed from the right panels. The dashed lines in the right panels indicate the RMS scatter after the correction.

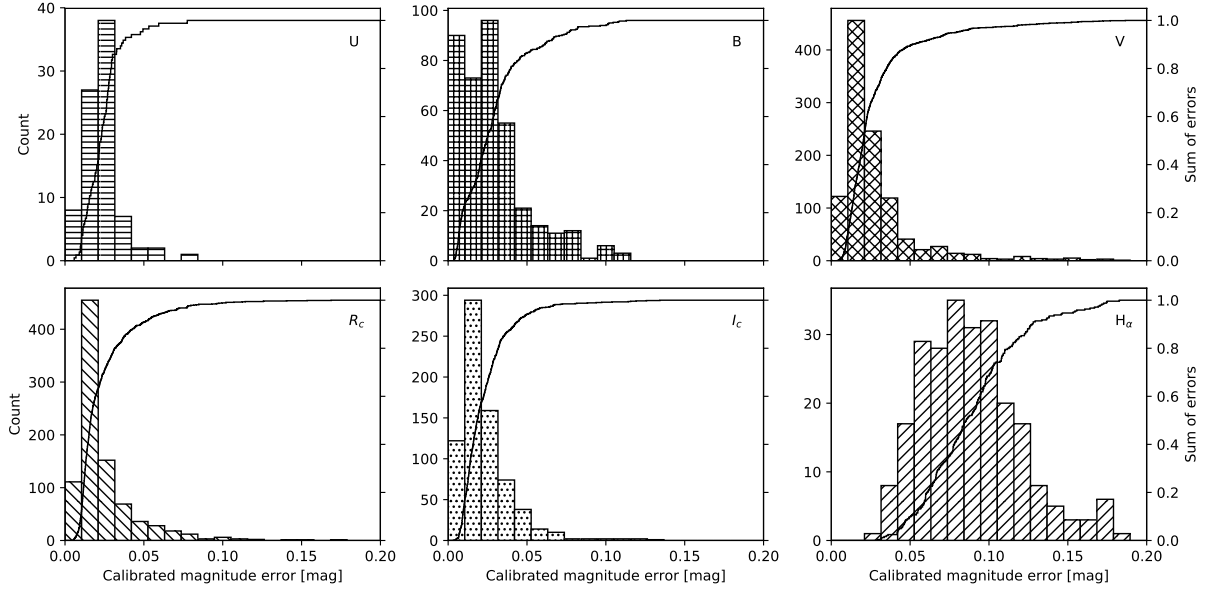


Figure 3.6: Histograms showing the number of the photometric uncertainties of all brightness measurements of V 1490 Cyg after the colour correction. Each panel represents one of the filters. The solid line represents the cumulative distribution. One can see that more than 80 % of the V, R_c , and I_c measurements have photometric uncertainties of less than 0.04 mag.

Table 3.2: Observation dates of LCOGT optical spectra and the measured H_α equivalent width for V 1490 Cyg.

Julian Date	EW [\AA]
2458338.7817	− 4.31
2458343.9943	− 5.30
2458348.8409	− 4.36
2458368.9099	− 8.63
2458373.8684	− 3.29
2458376.9494	− 3.49

spectra is the H_α line. All spectra were normalised to the continuum near the H_α line and the equivalent width (EW) of the line determined by fitting a Gaussian profile to the line. The region around the H_α line for all spectra are shown in Fig. 3.7.

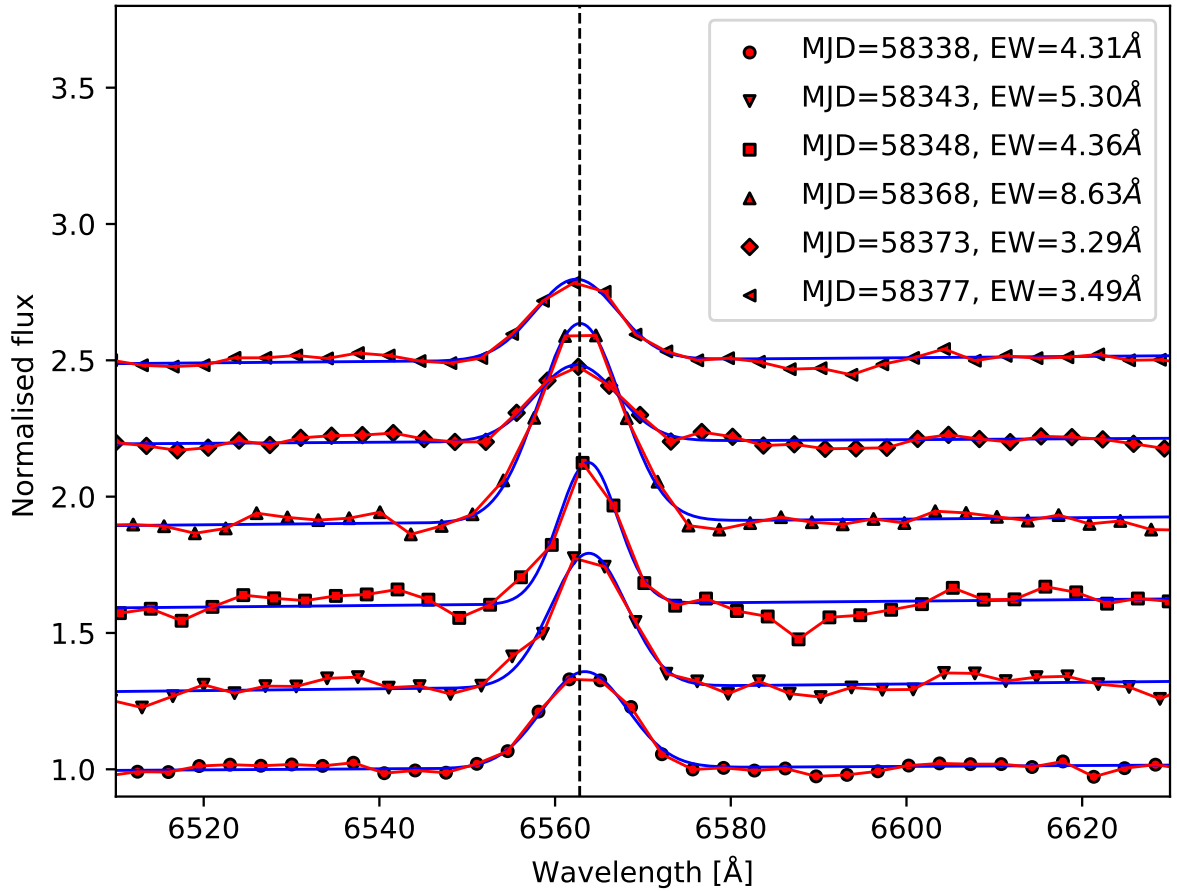


Figure 3.7: H_{α} line profiles for V 1490 Cyg taken during August and September 2018, ordered in time from bottom to top. The exact Julian dates and H_{α} equivalent widths are listed in Table 3.2. The symbols and connecting lines indicate the data, while the solid smooth lines are the Gaussian fit to the H_{α} line from which the equivalent widths are measured. The dashed vertical line indicates the nominal H_{α} wavelength.

Analysis of the Data for the Light Curve of V 1490 Cyg

4.1 The Quasi-Periodic Light Curve of V 1490 Cyg

Quasi-periodic dimming events allow for distances of occulting material to be determined from the central star. Observations across several periods enable investigations into temporal changes in the line-of-sight column density distribution, and multi-wavelength data allows for dust scattering properties to be analysed. The HOYS project aims to identify such periodic dimming events around YSOs. The data-set is used to search for periodicity in light curves from YSOs in the Pelican nebula (IC 5070).

The Pelican Nebula is a H II star forming region (SFR) associated with the North America Nebula in the constellation Cygnus. Whilst the two nebulae are catalogued as separate objects due to their visual appearance, they are now commonly regarded as parts of the same physical gas and dust cloud whose properties were reviewed by Reipurth and Schneider (2008). Rebull et al. (2011) identified more than 2000 YSOs in the 7 deg² field towards North American and Pelican complex including nearly 250 YSOs in the Pelican cluster.

V 1490 Cyg, also known as 2MASSJ20505357+4421008, is located in the Pelican Nebula IC 5070 at the J2000 position RA = 20h50m53.58s, DEC = +44°21'00.88" (Gaia Collaboration, 2018). It has been classified as a low-mass YSO and emission-line object by Ogura et al. (2002), having detected H α emission in its spectrum. Samus et al. (2003) determined it to be a Variable Star of Orion Type (*Or**). It is not listed in Findeisen et al. (2013) who surveyed the area using data from the Palomar Transient Factory but has recently been included in the ASASS-N variable stars, reporting no periodicity of the source. V 1490 Cyg was additionally included in the list of candidates for YSOs published by Guieu et al. (2009) and has been further studied by Ibryamov et al. (2018a), who also did not report any periodicity. Froebrich et al. (2018b) investigated the source and determined a period of approximately 31.8 days in the V-band. The object was also included in the analysis of HOYS data in Froebrich et al. (2018a). There it was classi-

Table 4.1: Ranges of variability for each filter for V 1490 Cyg . Given are the minimum and maximum recorded magnitudes and the difference between them.

Filter	min [mag]	max [mag]	Δm [mag]
U	18.18	14.92	3.26
B	18.70	16.60	2.10
V	17.31	15.03	2.27
R_c	15.96	13.97	1.99
H_{α}	15.29	11.00	4.29
I_c	15.26	13.65	1.61

fied as one of the most variable sources, grouped into the extreme dipper category. The colour and brightness changes were estimated to be consistent with dust grains that are larger than typical ISM dust grains.

The 4 year long-term HOYS light curves of V 1490 Cyg , observed between September 2015 and September 2019 in filters U, B, V, R_c, H _{α} and I_c are shown in Figs. 4.1, 4.2 and 4.3. The object shows strong variability, with large amplitude changes in all filters, in agreement with its classification as variable star by Samus et al. (2003). In Table 4.1, the range of maximum variability in each filter is listed. The brightness variations of V 1490 Cyg are seen over the entirety of the observing period.

A focused, coordinated, observing campaign of IC 5070 was run between 1st August – 15th September of 2018. All participants were encouraged to image the Pelican Nebula as often as they were able, enabling an investigation into the short-term variability of the source on timescales of hours. Figure 4.4 shows a close-up of the light curve in U, B, V, R_c and I_c, as well as for R_c – H _{α} over this time. The apparent 15–16 day period in this figure is actually just a double dip event. Some observed periods display such features, but not in others, showing a stochastic nature.

One can see clear, short duration changes in the brightness of the source during this 45 day observing period. In the four broad-band filters (B, V, R_c, I_c), the light curves appear to show exactly the same behaviour with only differing amplitudes. The U-band data, although sparse, does not follow this trend and shows very large variability on very short time scales. This will be discussed in more detail in Chapter 4.3. The R_c – H _{α} light curve also does not follow the general trend of the broad-band filters. Both longer and shorter term variability differs, with short term bursts having amplitudes of up to 1 mag.

A more detailed investigation of the entire 4 year light curve reveals that the variations in the star’s brightness occur as dips in brightness lasting from a few days to about two weeks. A Lomb-Scargle Periodogram (Scargle, 1982) was determined, to investigate if these dips are periodic. The periodograms for the B, V, R_c, and I_c filters are shown in Figs. 4.5, 4.6. A clear quasi-periodic behaviour of V 1490 Cyg for the broad-band filters V, R_c and I_c may be identified, with a roughly 31.5 day period, in agreement with Froebrich et al. (2018b).

Utilising the V, R_c and I_c HOYS data, an average period of 31.423 ± 0.023 days was found for occultations. The uncertainty is the RMS of the periods determined for the individual filters. In order to improve the accuracy of the period determinations, B, V,

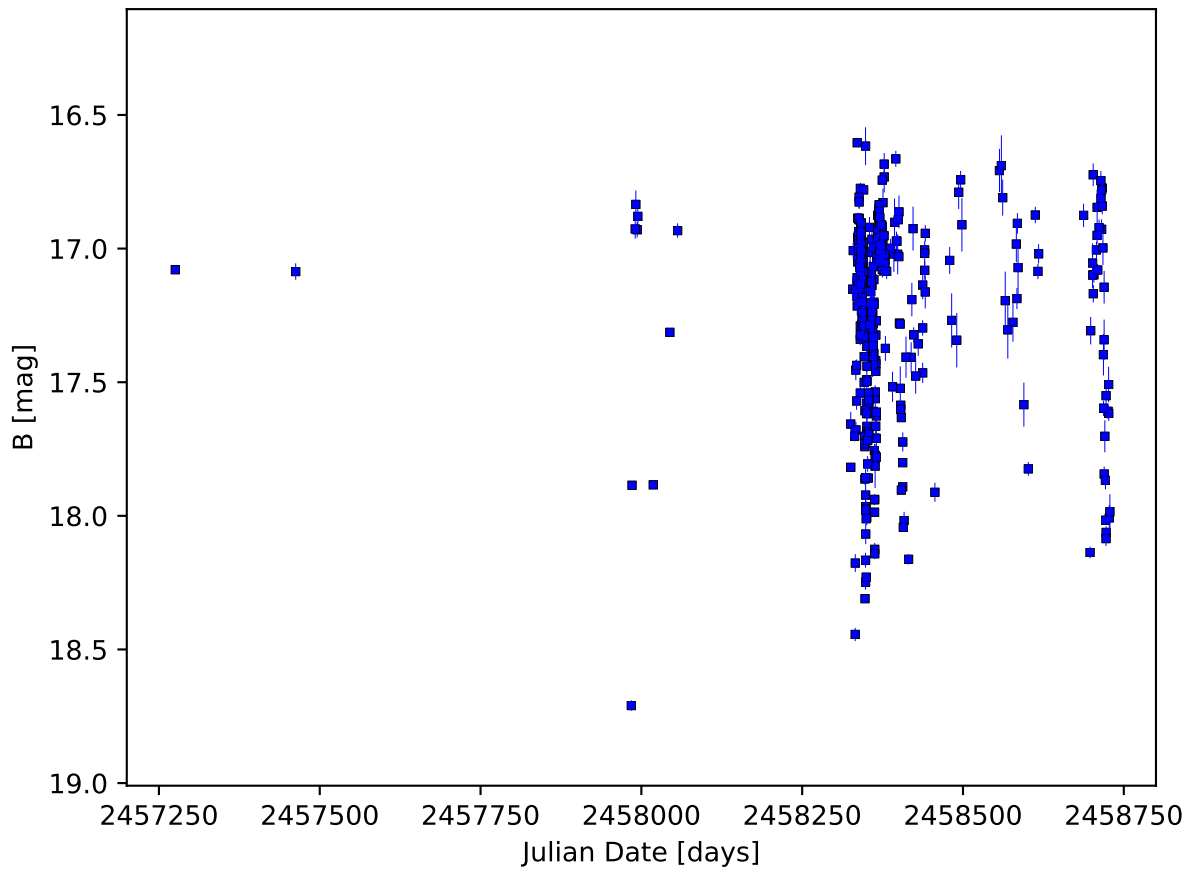
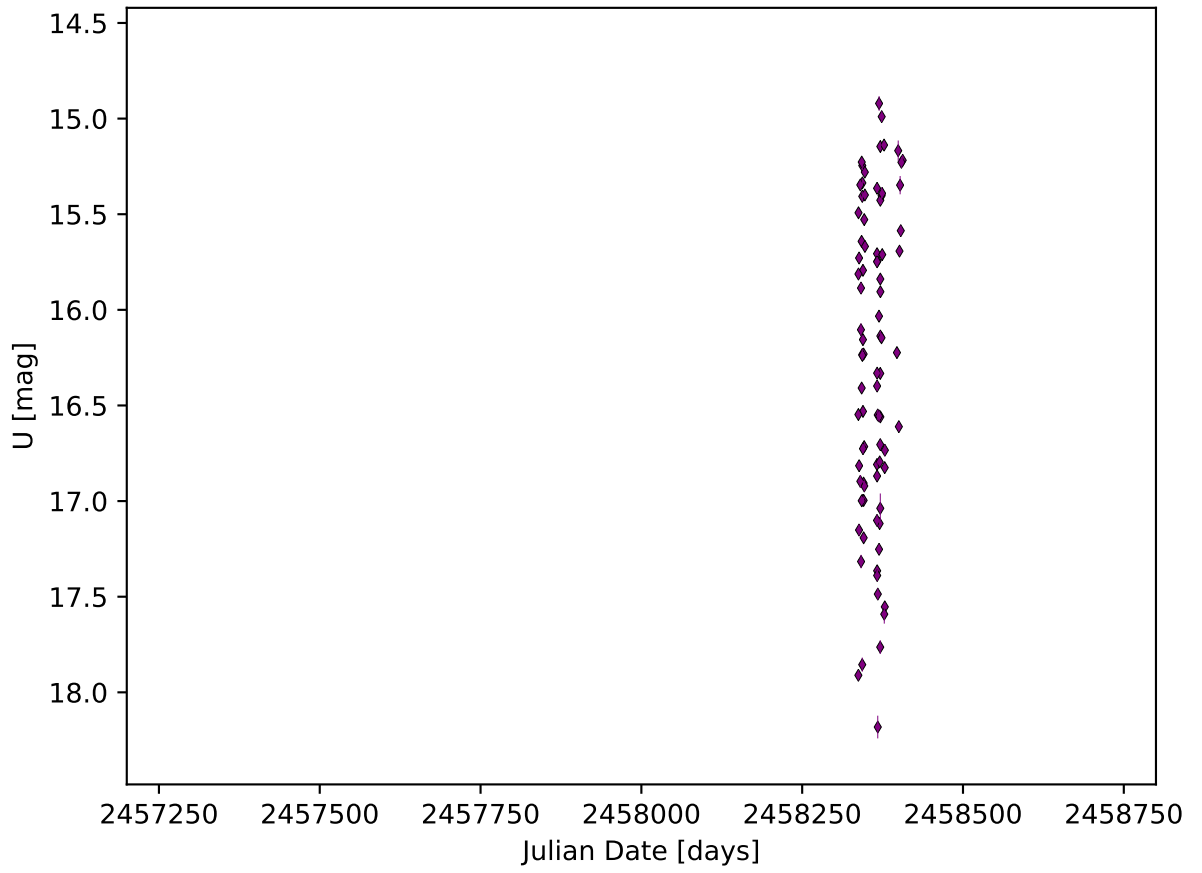


Figure 4.1: Long term HOYS U and B light curves of V 1490 Cyg over the complete observing period.

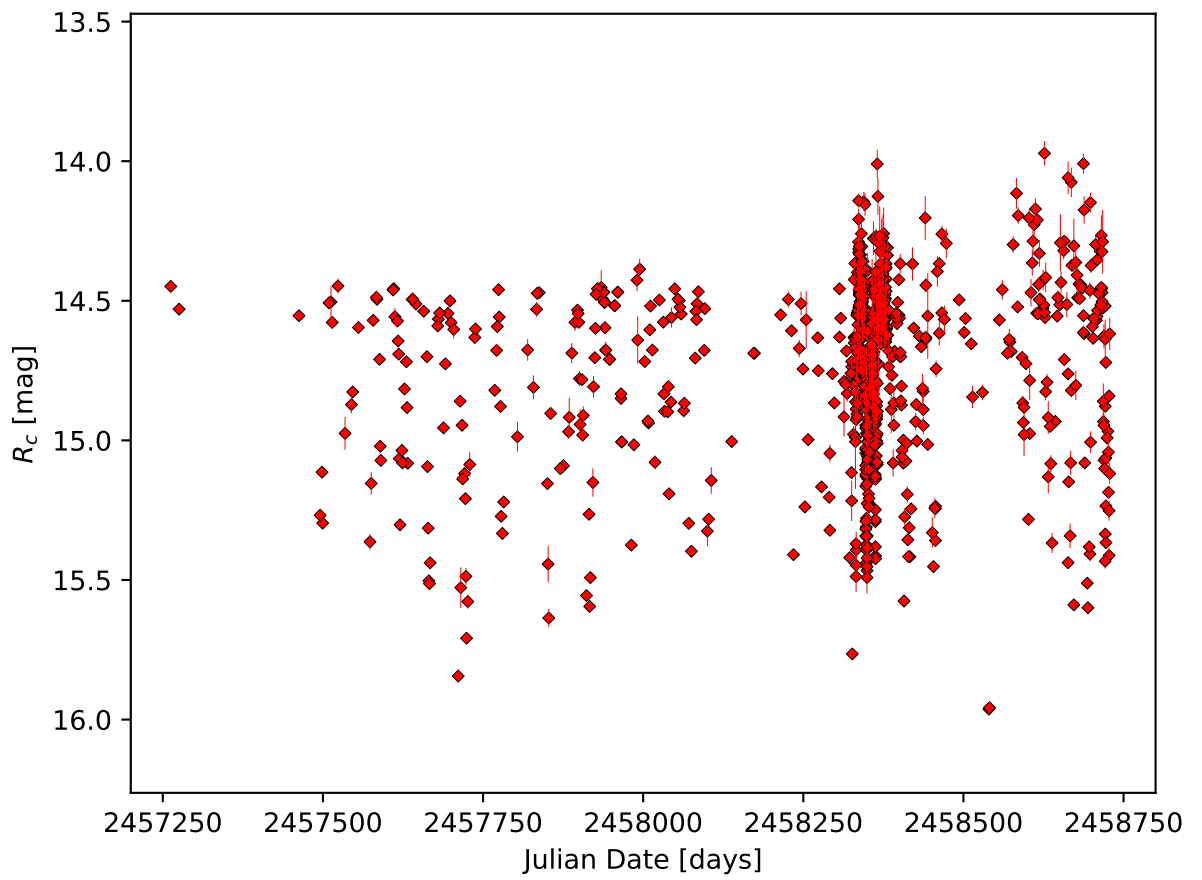
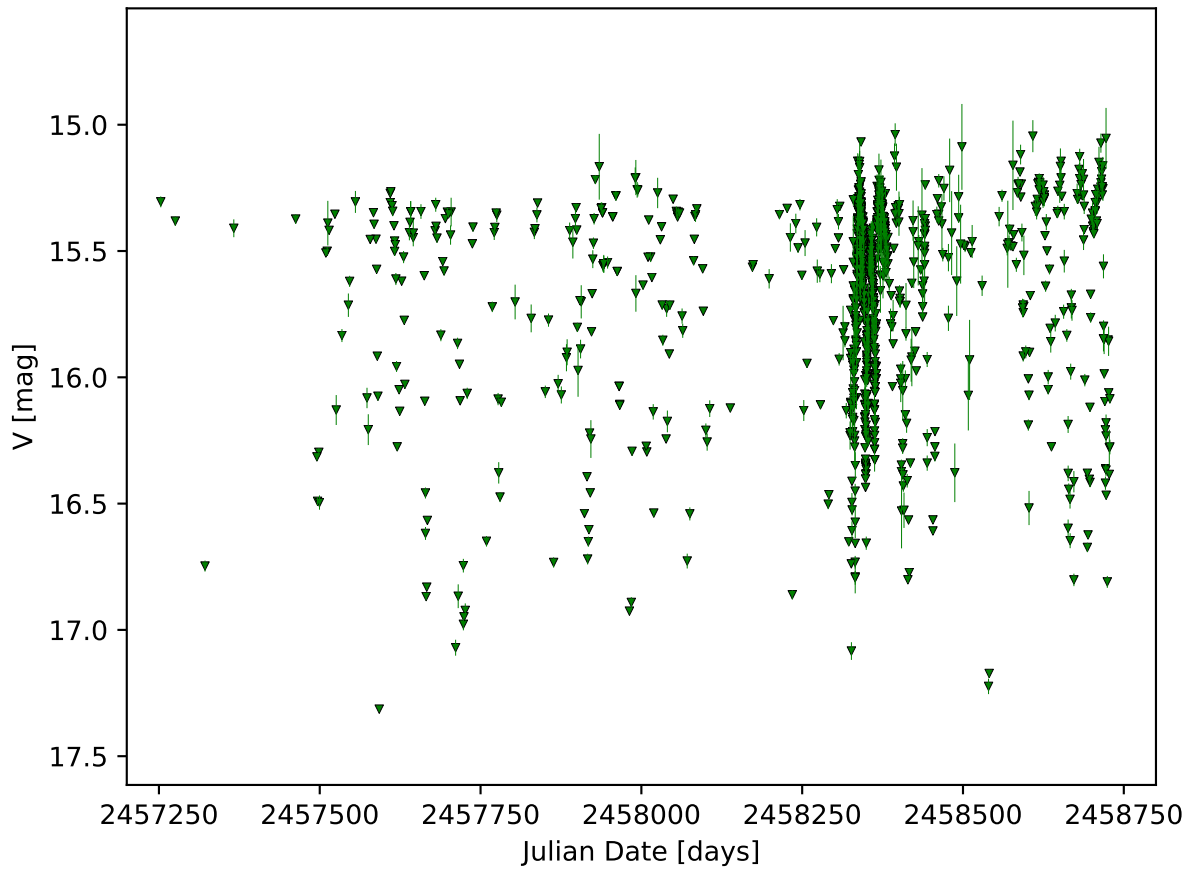


Figure 4.2: Long term HOYS V and R_c light curves of V 1490 Cyg over the complete observing period.

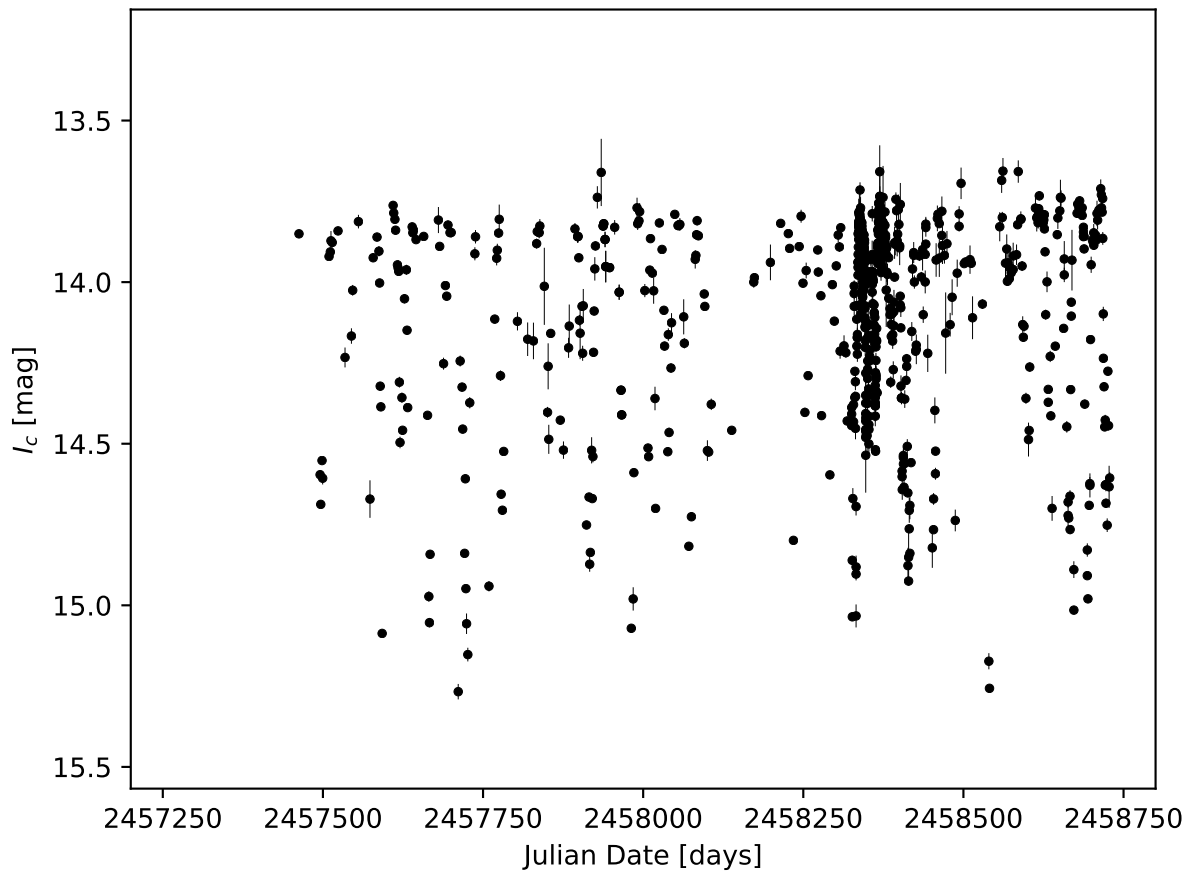
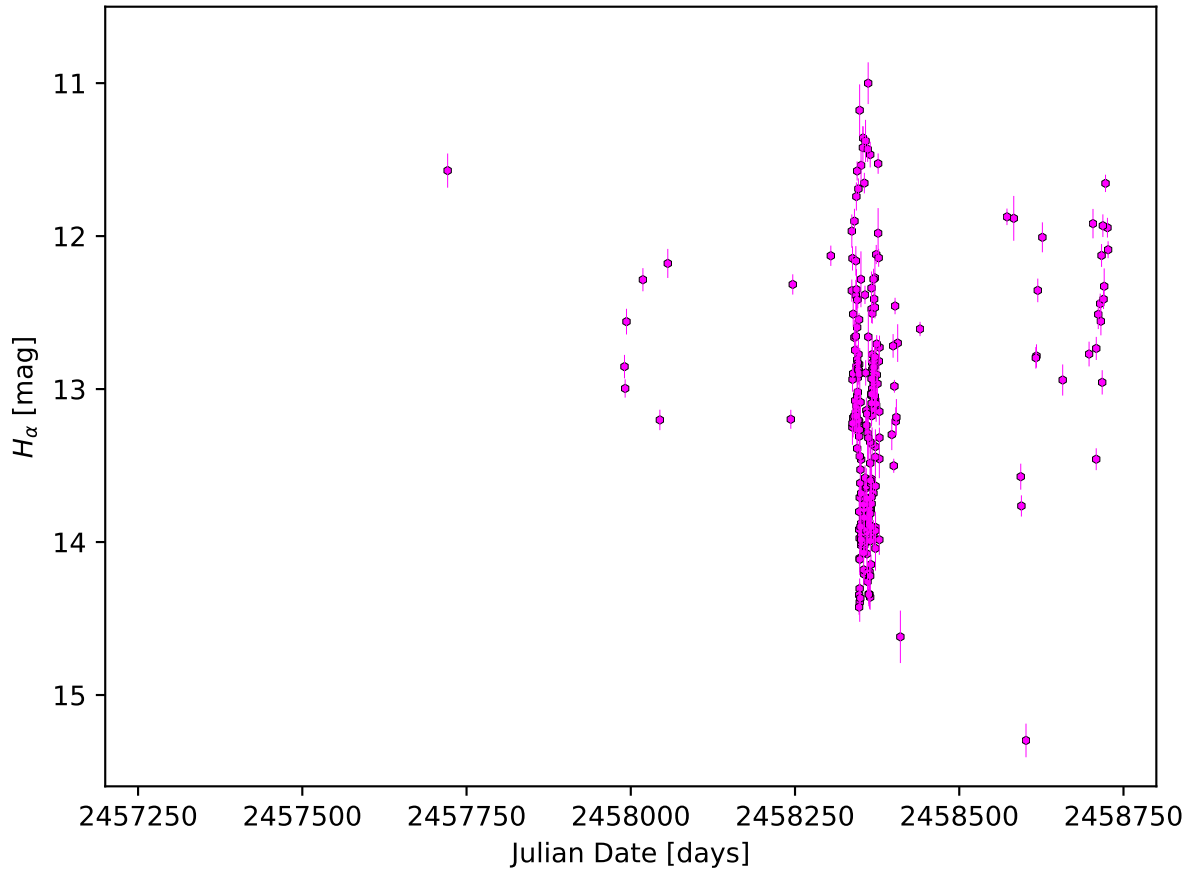


Figure 4.3: Long term HOYS H_α and I_c light curves of V 1490 Cyg over the complete observing period.

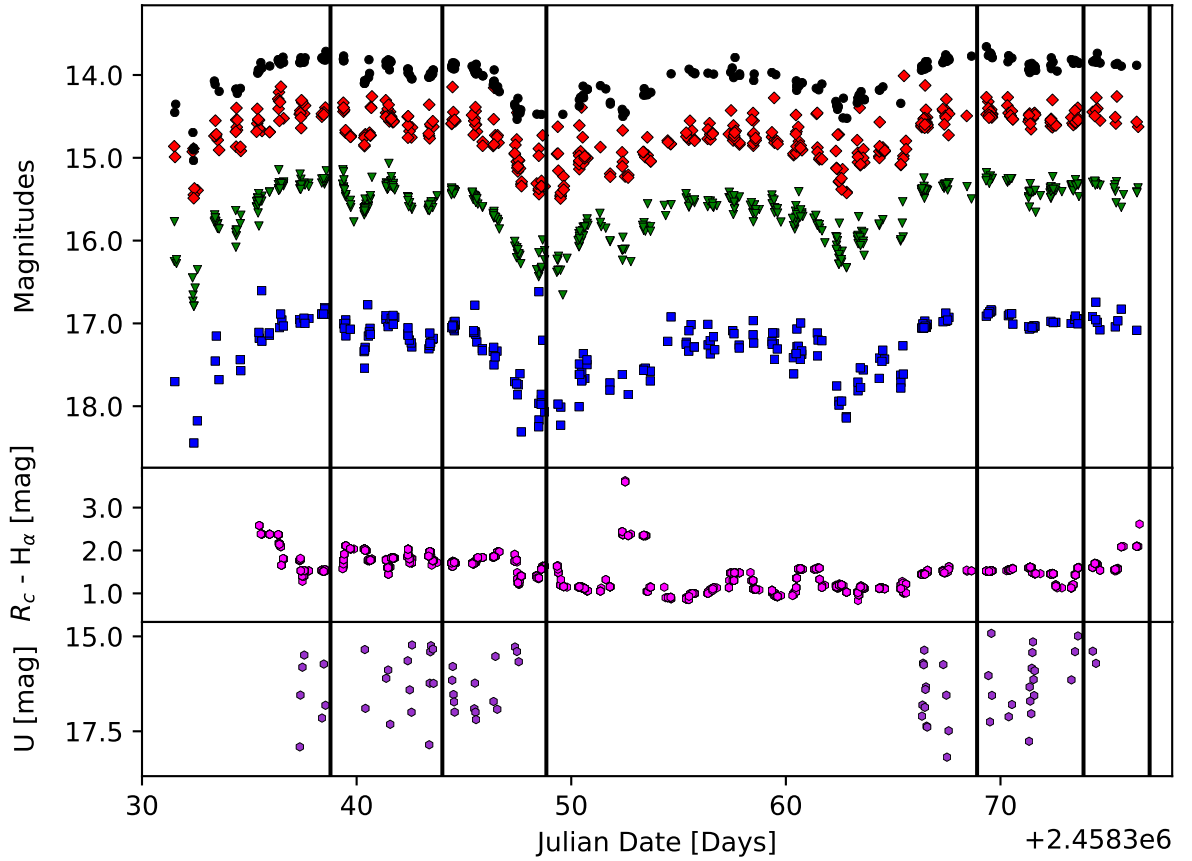


Figure 4.4: **Top panel:** HOYS light curves in B, V, R_c , and I_c of V 1490 Cyg for the high cadence campaign run between 1st August and 15th September 2018. **Middle panel:** $R_c - H_\alpha$ magnitudes for V 1490 Cyg for the same time period. **Bottom panel:** U magnitudes for V 1490 Cyg for the same time period. The vertical lines in all three panels indicate the times when the LCOGT spectra are taken.

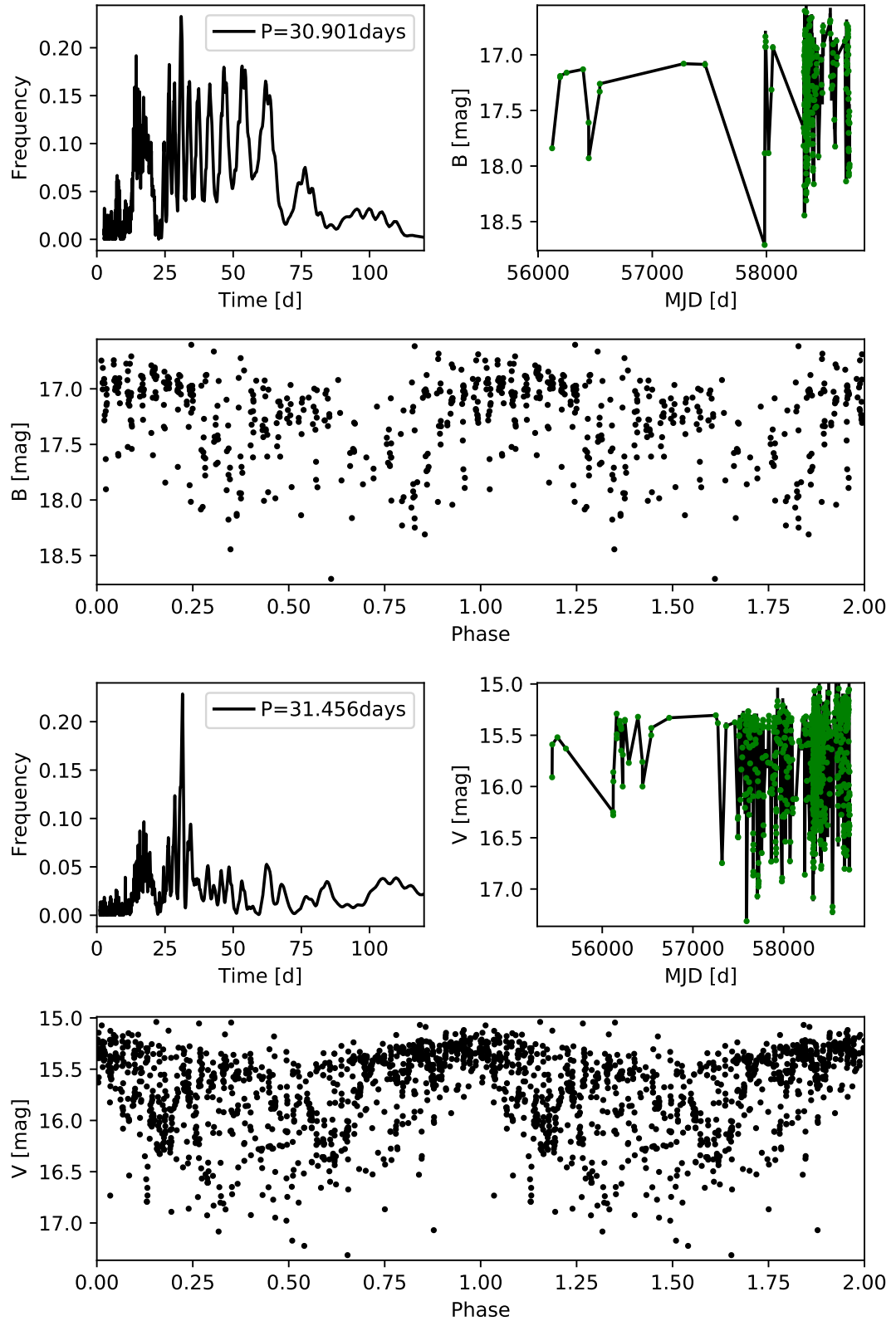


Figure 4.5: **Top Left:** Shown is a Lomb-Scargle periodogram (Scargle, 1982) of the V 1490 Cyg light curve in the B (top) and V (bottom) filter. Only data with a magnitude uncertainty of less than 0.2 mag has been included, as well as the data from Ibryamov et al. (2018a). **Top right:** The full light curve of V 1490 Cyg. **Bottom:** The phase plot of V 1490 Cyg showing two full periods.

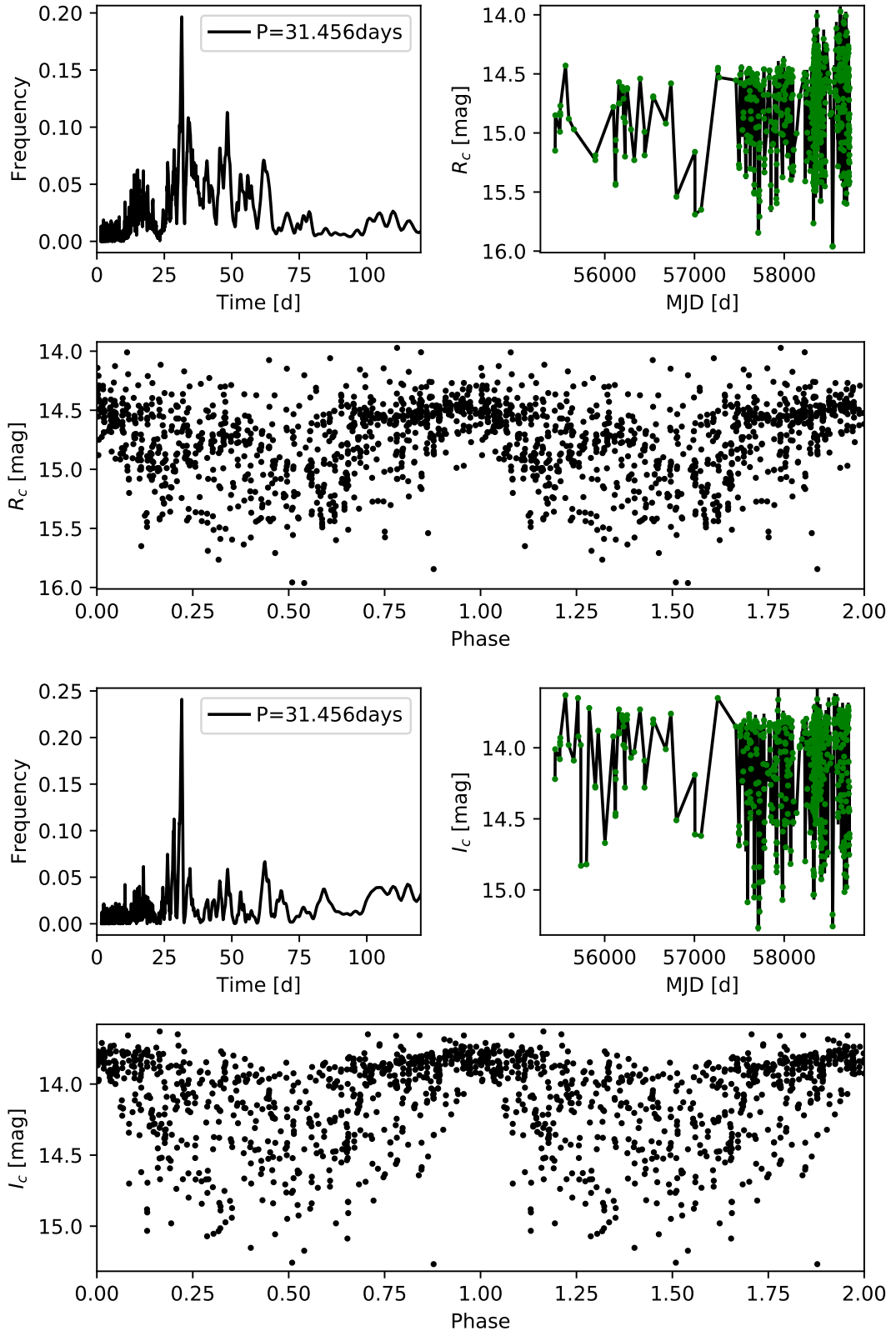


Figure 4.6: **Top Left:** Shown is a Lomb-Scargle periodogram (Scargle, 1982) of the V 1490 Cyg light curve in the R_c (top) and I_c (bottom) filter. Only data with a magnitude uncertainty of less than 0.2 mag has been included, as well as the data from Ibryamov et al. (2018a). **Top right:** The full light curve of V 1490 Cyg. **Bottom:** The phase plot of V 1490 Cyg showing two full periods.

R_c , and I_c observations were included from Ibryamov et al. (2018a, 2019) who collected long-term photometric data of V 1490 Cyg between September 2010 to October 2017. This effectively doubles the baseline of the data, extending the observation period from September 2010 to September 2019. The mean period for the three filters then becomes 31.447 ± 0.011 days, which is used for the purpose of this thesis throughout.

All Ibryamov et al. (2019) CCD observations of V 1490 Cyg were obtained with the 50/70 cm Schmidt telescope located at the Rozhen National Astronomical Observatory in Bulgaria. A total of 119 observational nights were used to estimate the brightness of the object. Observations were performed with the FLIPL16803 CCD camera. All technical parameters and specifications for the camera used are given in Ibryamov et al. (2015). The images were taken through a standard Johnson-Cousins (BVR_cI_c) set of filters. Frames were dark subtracted and flat-field corrected. Photometry was performed using an IDL based DAOPHOT subroutine. A reference of 11 stars reported in Ibryamov et al. (2018b) were used as a comparison sequence in BVR_cI_c . All data were analysed using the same aperture, which was chosen to have a $4''$ radius, while the background annulus was taken from $9''$ to $14''$. The mean value of errors in the reported magnitudes is $0.01 - 0.02$ mag for the I_c - and R_c -band data and $0.01 - 0.03$ mag for the V- and B-band data.

The phase zero point (the object is bright) occurs at $JD = 2458714.0$, which corresponds to 12:00 UT on 18th August 2019. The periodograms in Figs. 4.5, 4.6 indicate that the object is most likely to be observable in its bright state within about ± 5 days (15% of the period) from the nominal phase = 0 point.

Note that despite the much smaller amount of B-band data in the light curve, the periodogram shows a peak at the above determined period (see Fig. 4.5). The peak, whilst significant, is surrounded by noise when compared to the other filters.

4.2 Asymmetry of the Light Curve of V 1490 Cyg

Light curves may also be asymmetric with respect to a reflection along the magnitude axis. Some stars show sharp increases in flux with others displaying prominent downward dips. It is believed that this behaviour is connected with the physical mechanisms causing variability. Upon visual inspection of V 1490 Cyg's light curve, shown in Figs. 4.1, 4.2 and 4.3, one can see a clear dipping pattern in B, V, R_c and I_c filters. Cody et al. (2014) developed an asymmetry metric M to determine to what extent such asymmetry occurs.

$$M = \frac{\langle d_{10\%} \rangle - d_{med}}{\sigma_d} \quad (4.1)$$

Following the method established in Cody et al. (2014), M was determined for the V data of V 1490 Cyg, using Eqn. 4.1. $\langle d_{10\%} \rangle$ is the mean of all magnitudes in the top and bottom ten percent of the V-band light curve, d_{med} the median of all V magnitudes and σ_d the overall RMS of the V-band data-points from the mean.

As detailed in Cody et al. (2014), objects with negative values are classified as bursters. These are objects that show short duration increases in brightness compared to their normal magnitudes. Conversely, objects with positive values for M are dippers, which have short duration decreases in brightness compared to their normal state.

Cody et al. (2014) use ± 0.25 as thresholds for M to identify bursters and dippers. In the analysis of targets in Froebrich et al. (2018a), a slightly more conservative value was employed, identifying a burster as having $M < -0.5$, and a value of $M > +0.5$ considered a dipper. Objects with M values between these limits are considered to have a symmetric behaviour. This threshold was raised to $M \pm 0.75$ for the most extreme bursters and dippers. The flux asymmetry (M) for the Visual light curve of V 1490 Cyg is calculated to be 0.819. Repeating this analysis for data obtained in the B-, R_c - and I_c -bands yields values of 0.822, 0.550 and 0.96 respectively. Following the criteria set above, this indicates that V 1490 Cyg may be classified as an extreme dipper, agreeing with the findings of Froebrich et al. (2018a).

4.3 Analysis of the Variability Fingerprints

In order to further analyse the source variability, a *variability fingerprint* of the source was determined in each filter. This allows for a detailed investigation into the variability timescales and amplitudes of V 1490 Cyg. The method partially follows Findeisen et al. (2015), determining all possible time (t) and magnitude (m) differences for two measurements i, k for all data-points in a light curve that are taken in the same filter. Therefore, $\Delta t = t_i - t_k$ and $\Delta m = m_i - m_k$, where $t_i > t_k$. The differences are then used to populate a 2D Δt vs. Δm histogram, where the bins in Δt are log10-spaced. These histograms are smoothed using a bi-cubic interpolation and normalised to an integral of one for each bin of Δt . This ensures that the values in these variability fingerprints represent the probability (p) that the source shows a change of Δm for a given time interval, Δt , between observations.

Figures 4.7, 4.8 and 4.9 show these variability fingerprints for V 1490 Cyg for the five broad-band filters, as well as for $R_c - H_\alpha$. The plots for B, V, R_c and I_c show extremely similar behaviour, the B-band data suffers from a smaller number of observations compared to the other filters. For time intervals between observations of less than a few days the object is most likely not variable and is observed at the same magnitude. The width of the high probability ($p > 10\%$) behaviour corresponds very well to the typical photometric errors measured in the photometry of the object after the calibration procedure (see Fig. 3.6 in Chapter 3.2.2).

Between 10 day and 30 day intervals, the probability to find the object changed within its range of variability is almost homogeneously distributed. At roughly a 30 day interval the object is then again most likely to be observed at an unchanged magnitude, representing the semi-periodicity of the source determined in Chapter 4.1. However, there is still a significant probability that the source is not exactly returning to the same brightness after one period. This indicates that the internal structure of the dips varies each time it is observed. This is investigated in more detail in Chapter 4.4.

For larger than 30 day time intervals, the fingerprints show that the object is most likely

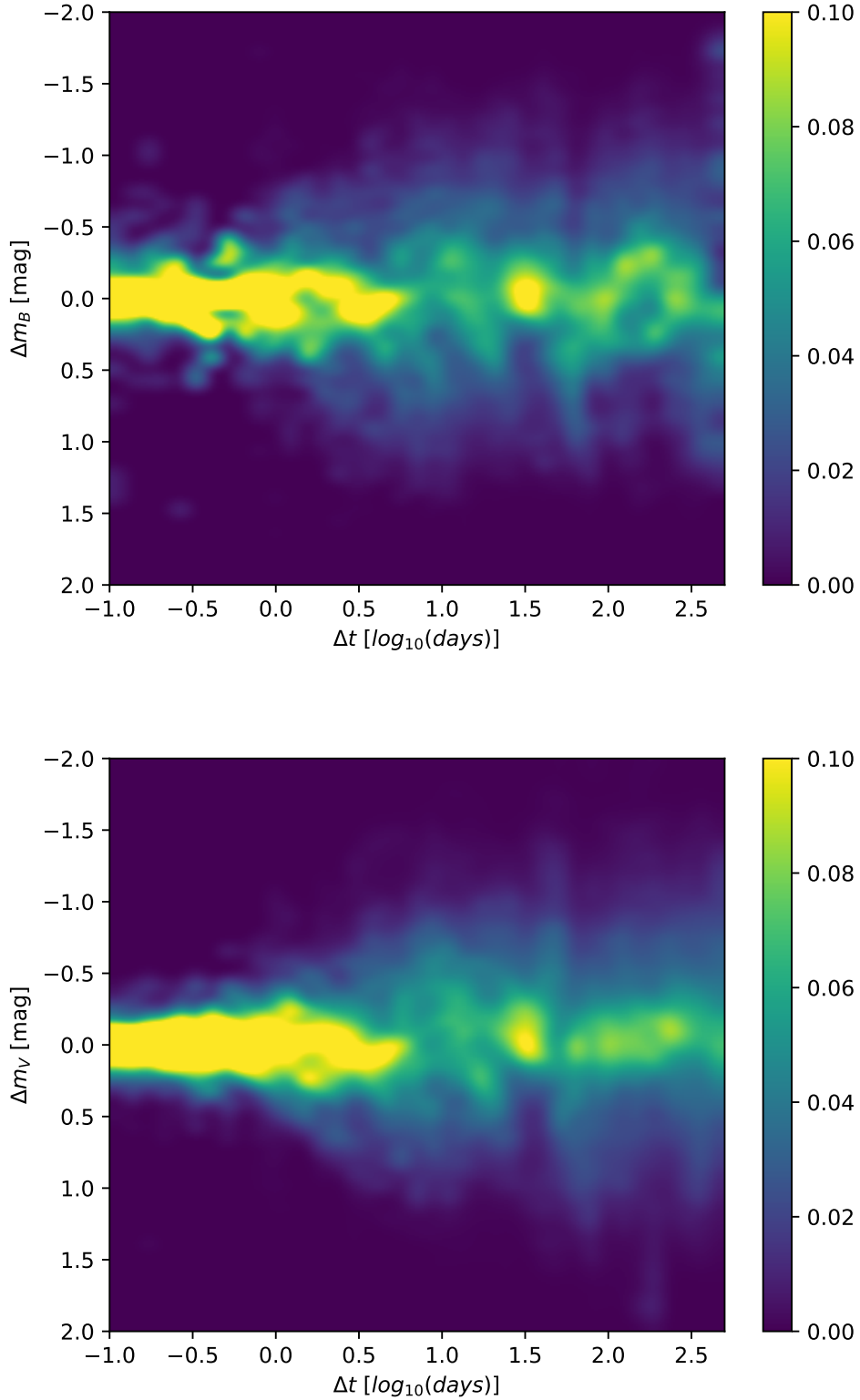


Figure 4.7: Variability fingerprint plots of B (top) and V (bottom) data for V 1490 Cyg. The colours indicate the probability of observing the object to undergo a change in magnitude for a given time gap between observations. Clearly observed is the periodicity of V 1490 Cyg at $\log(\Delta t) \approx 1.5$, which equates to the determined period of 31.447 d. The bin size is 0.08 mag and a factor of 1.237 for Δt .

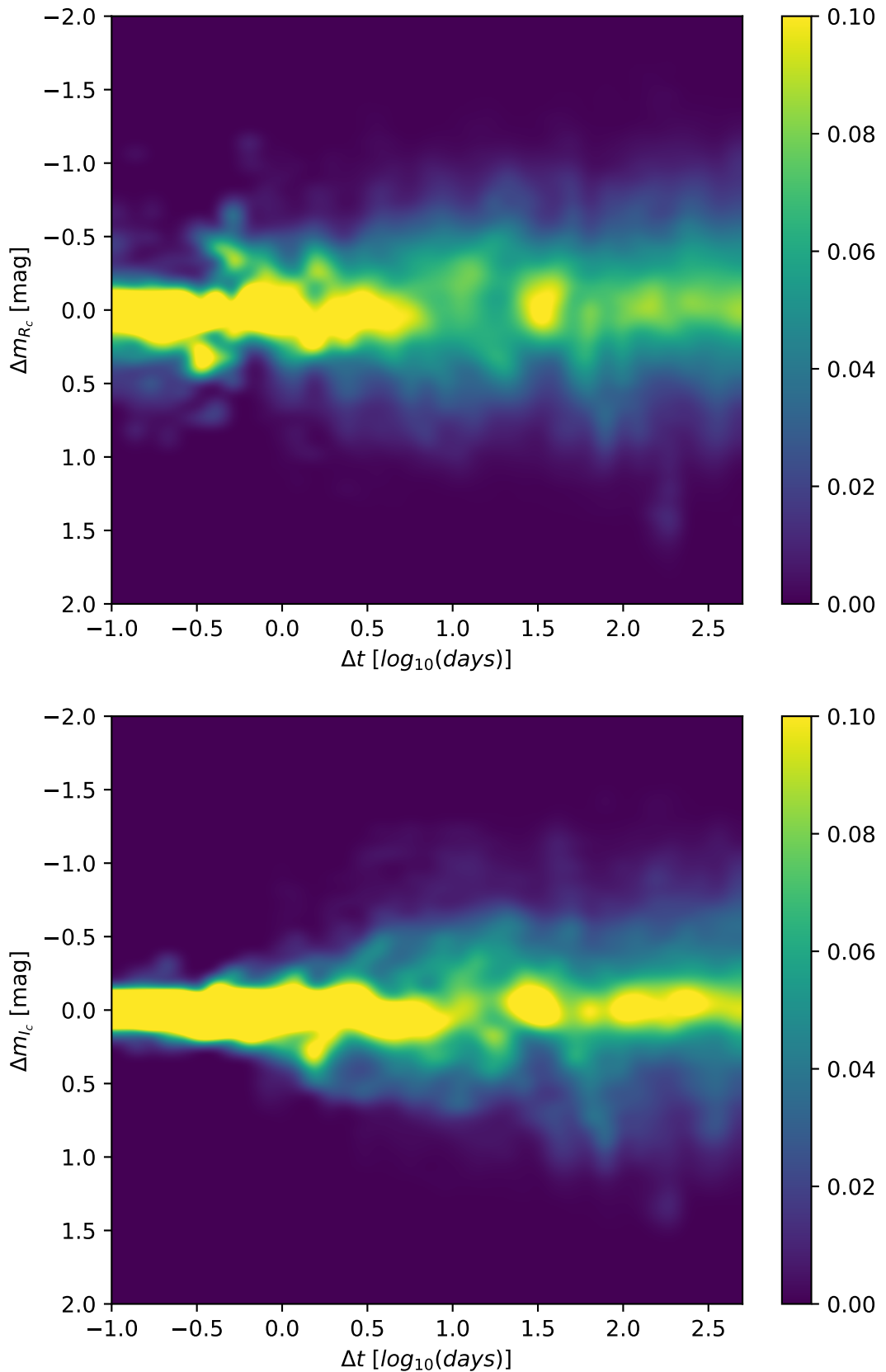


Figure 4.8: Variability fingerprint plots of R_c (top) and I_c (bottom) data for V 1490 Cyg. The colours indicate the probability of observing the object to undergo a change in magnitude for a given time gap between observations. Clearly observed is the periodicity of V 1490 Cyg at $\log(\Delta t) \approx 1.5$, which equates to the determined period of 31.447 d. The bin size is 0.08 mag and a factor of 1.237 for Δt .

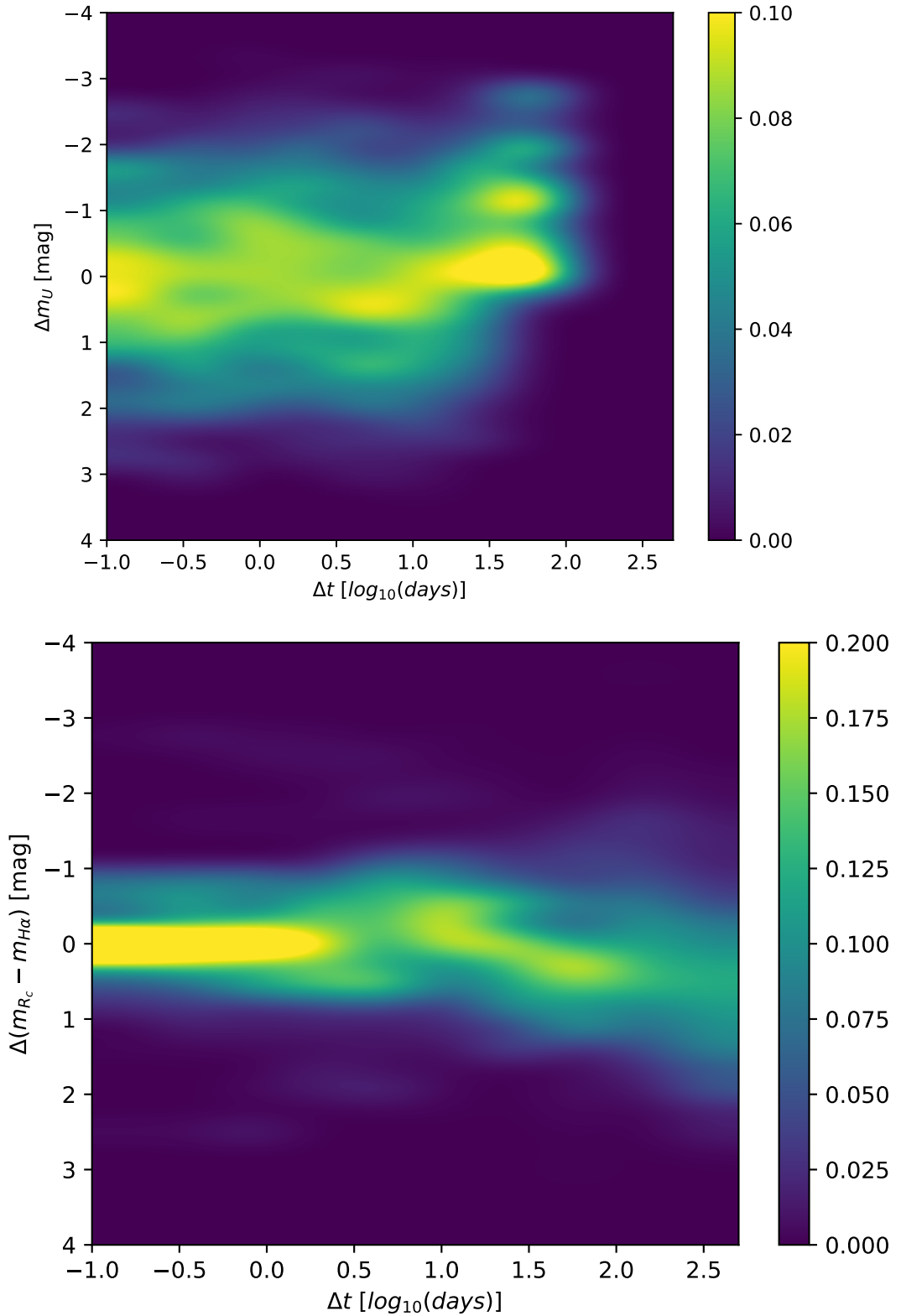


Figure 4.9: Variability fingerprint plots of U (top) and $R_c - H_\alpha$ (bottom) data for V 1490 Cyg. The colours indicate the probability of observing the object to undergo a change in magnitude for a given time gap between observations. Clearly observed in the B, V, R_c , I_c fingerprints is the periodicity of V 1490 Cyg at $\log(\Delta t) \approx 1.5$, which equates to the determined period of 31.447 d. The bin size is 0.27 mag and a factor of 2 for Δt .

to not change in brightness, but still has a significant probability to show variations within the min/max values found for each filter. Thus, the overall behaviour of the object remains unchanged for timescales beyond one period. From time intervals of one day upward, there is a non-zero probability that the object starts to vary by more than the photometric uncertainty. In the Δt vs. Δm space, this trend is almost linear from one day to about half the period, after which the variability does not increase any further. This short term variability is also very evident in the detailed light curve presented in Fig. 4.4.

Compared to the B, V, R_c , and I_c fingerprints, the behaviour for U and $R_c - H_\alpha$ is different (see Fig. 4.9). This difference is not just caused by the much reduced number of observations available but also, especially in U, the much shorter total time interval covered by the observations.

In the U-band, the variability for short time intervals is clearly different from the photometric uncertainties and also does not systematically increase towards one period. In essence, for U the full range of variability is reached already within time intervals of less than one day. Furthermore, the amount of variability is much larger. For example, the U-band magnitude changes by up to 3 mag in a single night. Variability in the U-band excess is indicative of accretion rate changes (Kalari et al., 2015); the correlation between the U-band excess luminosity and the accretion luminosity has been established both empirically (Gullbring et al., 1998; Herczeg and Hillenbrand, 2008) and theoretically (Calvet and Gullbring, 1998). This indicates short term (hours) accretion rate fluctuations in this object by a factor of up to ten or slightly larger, which is discussed further in Chapter 5.4.

It is possible for this high degree of variability to be seen with the naked eye. Figure 4.10 shows a 3×3 grid of observations of the source, taken in sequence over the course of approximately 7 hours. Shown in the bottom panel is the light curve in U over the observing period. The highlighted object is V 1490 Cyg. One is able to see the source dim and brighten in accordance with flux change.

The $R_c - H_\alpha$ fingerprint at small timescales, less than a few days, is similar the B, V, R_c and I_c filters, in that it is dominated by the photometric uncertainties, which are higher for the H_α images. There is a non-negligible probability that the source varies by up to 1 mag even at those short time intervals. This is caused by short bursts of variability, one of which is evident in the detailed light curve in Fig. 4.4. However, there is no strong indication that the $R_c - H_\alpha$ magnitude follows the same periodic behaviour that can be seen in the broad-band filters. Generally the variability in $R_c - H_\alpha$ increases slightly with an increase in time interval between observation. The apparent trend of a slight long term decrease in $R_c - H_\alpha$ visible in the fingerprint plot is not real, as it hinges on a single H_α data-point.

4.4 Column Density Distribution of Consecutive Dips

The quasi-periodic nature of V 1490 Cyg found in Chapter 4.1 indicates orbiting material held in place within the inner disk for at least the duration of the light curve, which is more than 4 years. As evident in the variability fingerprint plots shown in

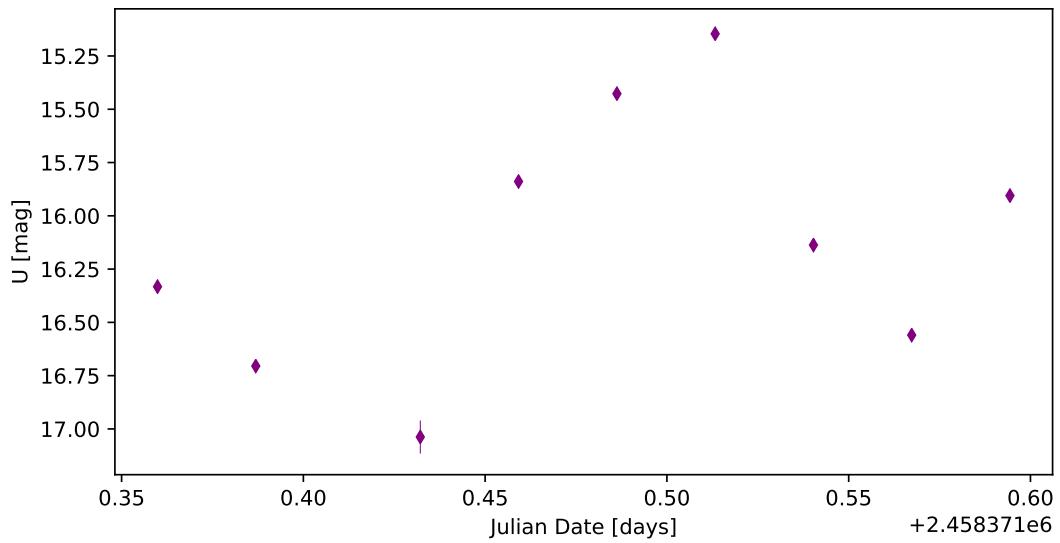
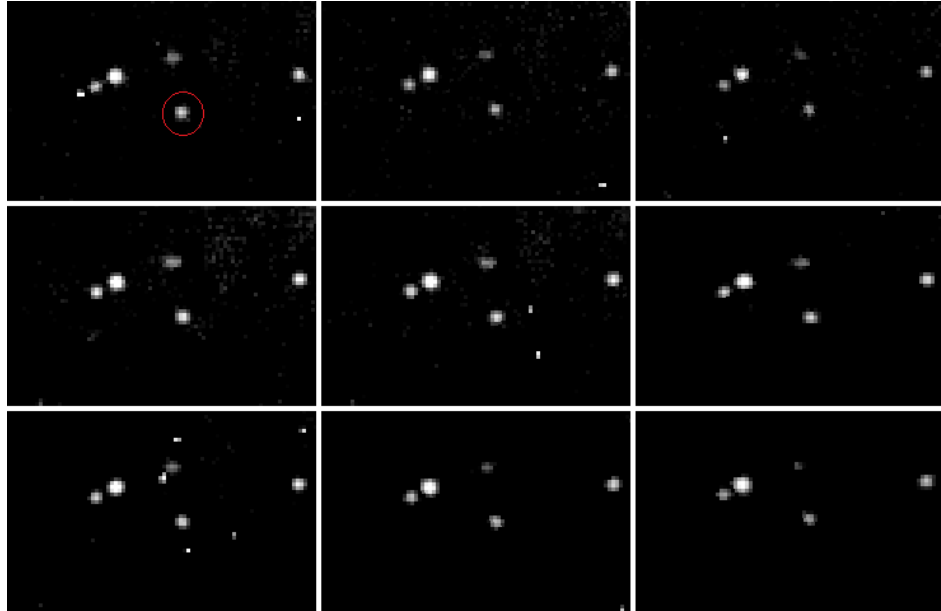


Figure 4.10: **3 × 3 grid:** Observations are ordered left to right and top to bottom sequentially by time. The highlighted object is V 1490 Cyg exhibiting dimming and brightening as shown in the light curve below. Each image is approximately $2 \times 1^\circ$ on the sky. **Bottom:** A section of the U-band light curve of V 1490 Cyg. The data displayed was taken on 9th September 2018 (JD 2458371). It shows the high variability of the star over timescales of hours. The observed variability order is matched to the 3×3 grid above.

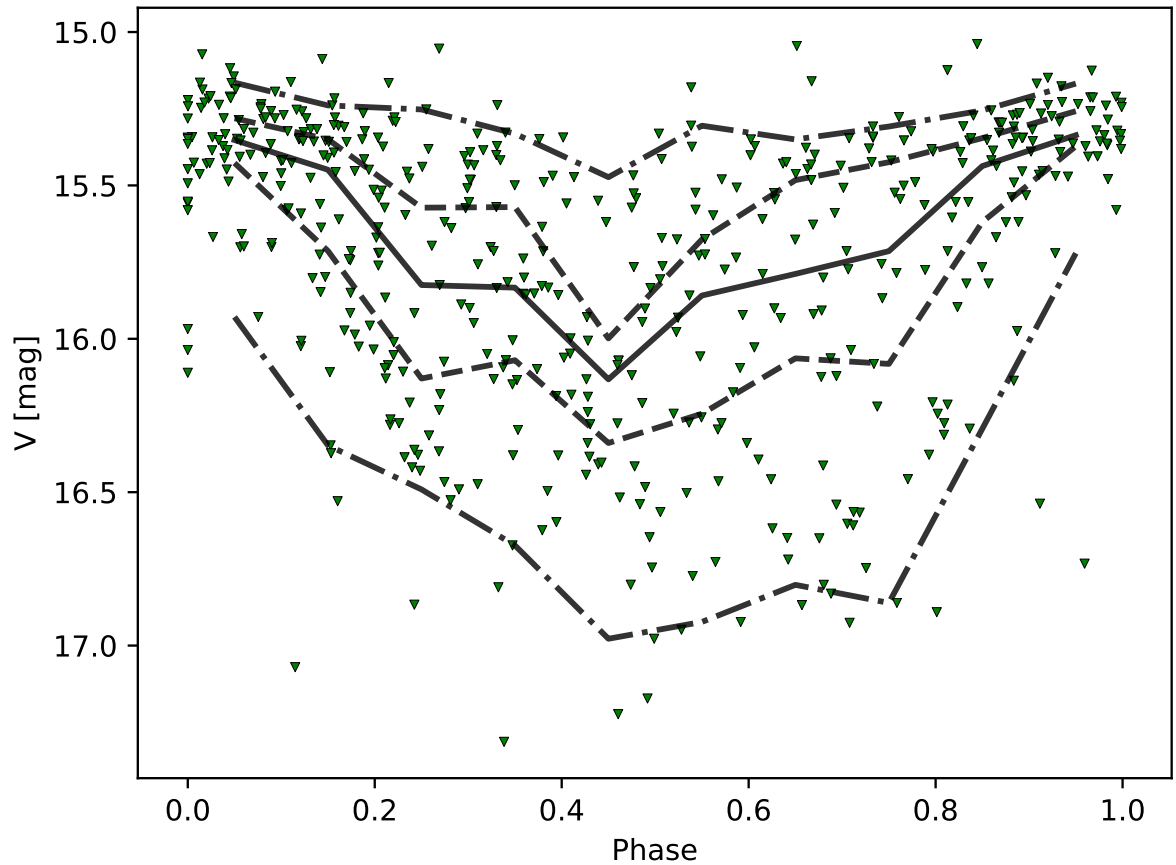


Figure 4.11: Phased light curve of V-band data for V 1490 Cyg . The solid line indicates the running median magnitude. The two most extreme dashed and the dash-dotted lines indicate the range within which 95 % of the data-points can be found. The other two dashed and the dash-dotted lines indicate the 68 % range for the data points. Note that the high cadence data (shown in Fig. 4.4) has been removed from this plot as it otherwise would dominate the typical shape due to the large amount of data in that 6 week period.

Figs. 4.7, 4.8 and 4.9, there is a significant probability that the source does not return to the exact same brightness after one full period. This indicates variation in the column density distribution of the material along its orbital path. This section will investigate any potential systematic changes in the column density distribution, which can hint at the timescales and/or mechanisms by which the material is either moved into and out of the orbiting structure or redistributed within it.

Figure 4.11 shows the folded V-band light curve of V 1490 Cyg with the high cadence data from Aug. – Sep. 2018 removed as it would otherwise dominate the analysis. The plot has the running median overlaid which indicates the typical column density distribution of material along the orbit. As one can see, the median occultations are up to about 0.7 mag deep and have a broad minimum. Figure 4.11 also shows the typical one- and two-sigma deviations from the median, which are indicated by the dashed and dot-dashed lines, respectively. They indicate that in some cases there is almost no detectable occultation, while the dips can, in extreme cases, be up to 1.7 mag deep in the V-band, during a larger part of the period.

The HOYS data now covers about 40 complete periods of V 1490 Cyg. It is now possible to investigate how the column density distribution along the orbital path varies as a function of the time interval between observations. In essence, one could construct the structure function of the column density.

The mean V-band magnitude difference $\Delta(m)$ was determined between all observations with a time separation of one period ± 1 day and again for a separation of 2 periods ± 1 day. This plot is shown in Fig. 4.12 with the upper left panel showing one period separated observations and the upper right showing the analysis for two periods. The lower two panels display the absolute mean V-band magnitude differences of the same data. No systematic trends are obvious, suggesting that material in the line-of-sight is replaced on timescales less than the orbital period.

To examine structure within each occultation, the phase space of consecutive dips was divided into 10 bins, each covering 10% of the phase. $\Delta(m)$ determined above was mean and median averaged for each bin and plotted with error-bars consisting of the RMS scatter. These results, mean (left) and median (right), are displayed in Fig. 4.13. Such analysis may be done for all pairs of V-band measurements which are N times the period (± 1 day) apart from each other. Figure 4.14 show this for N running from 1 to 10. The values for $\Delta(m)$ scatter less for all values of N , when the phase is close to 0 or 1, compared to phase values near 0.5. This is expected from Fig. 4.11.

To further analyse shape variations across N period separated dips, Fig. 4.15 displays the RMS magnitude scatter for bins in phase space. Bins are determined as for Fig. 4.13. For all observation matches within the bin, upper limit inclusive, RMS scatter was calculated and plotted, with the mean value shown in hatching.

The shape of each dip appears random across all values of N . This evidence further supports timescales of held material less than that of one full period. For material to build up across multiple periods before releasing onto the central object, lower N would show similar trends in their shape. Values of N greater than the timescale between which material is released would then become more random with increasing N . This behaviour is not observed in Fig. 4.15. There are therefore no systematic trends

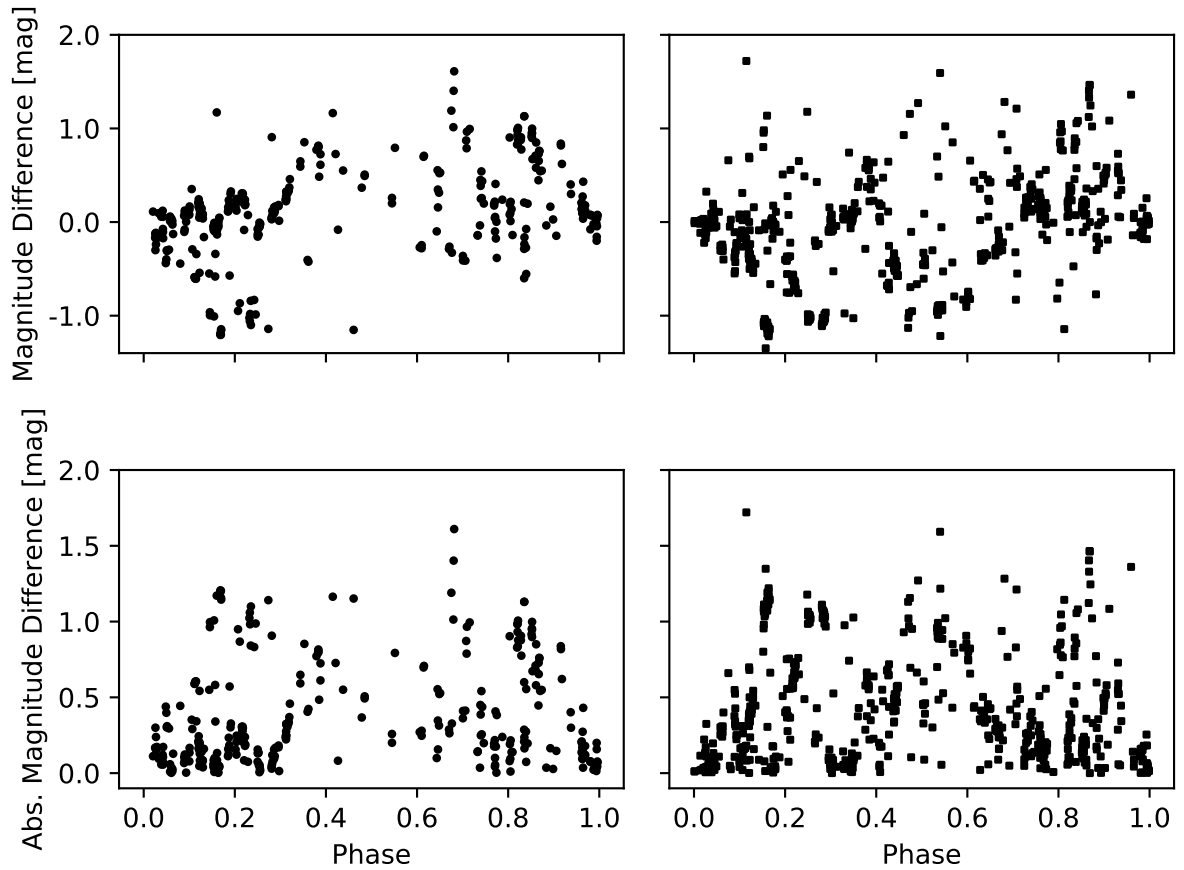


Figure 4.12: **Top:** The two panels show the magnitude difference between observations in phase space and the mean magnitude of observations 1 period ± 1 day (left) and 2 periods ± 1 day (right) away. **Bottom:** The two panels show the absolute magnitude difference between observations in phase space and the mean magnitude of observations 1 period ± 1 day (left) and 2 periods ± 1 day (right) away.

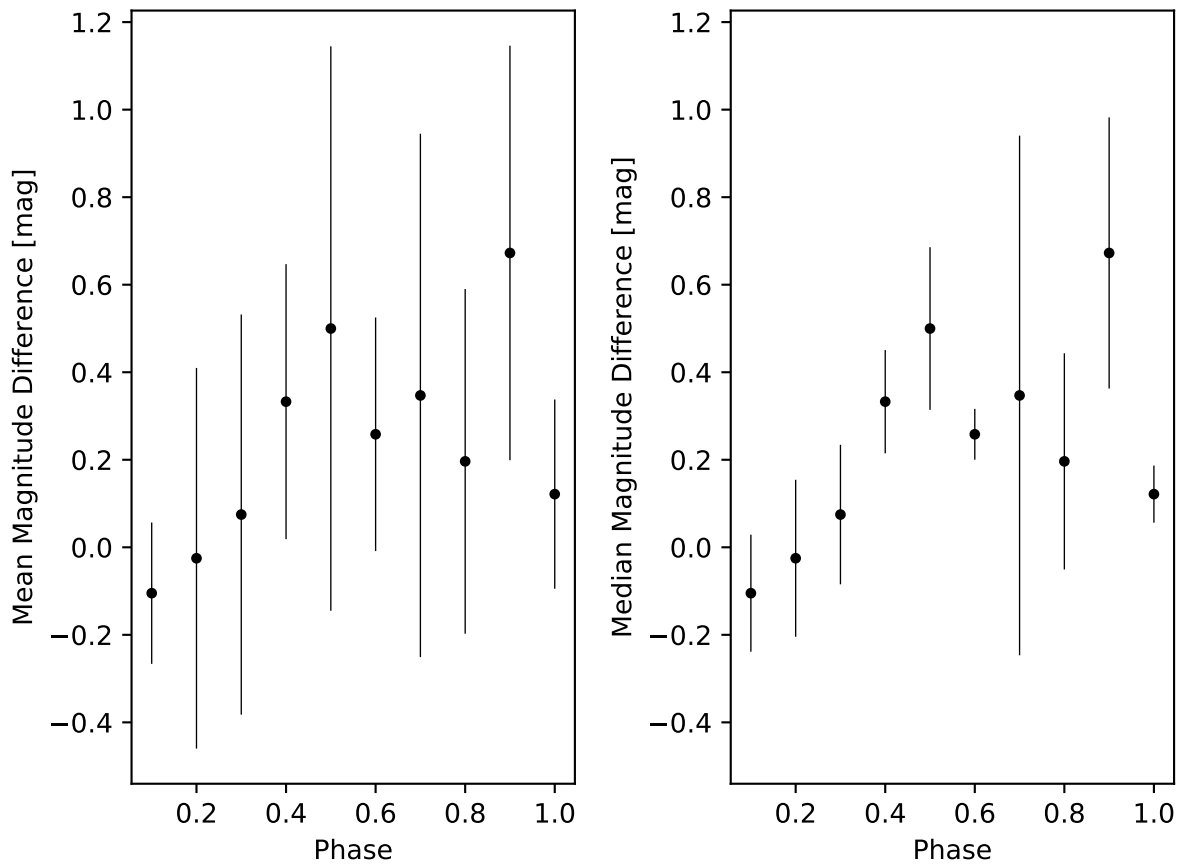


Figure 4.13: **Left:** Mean magnitude difference for consecutive dips. Error-bars show mean RMS scatter. **Right:** Median magnitude difference for consecutive dips. Error-bars show root median square scatter.

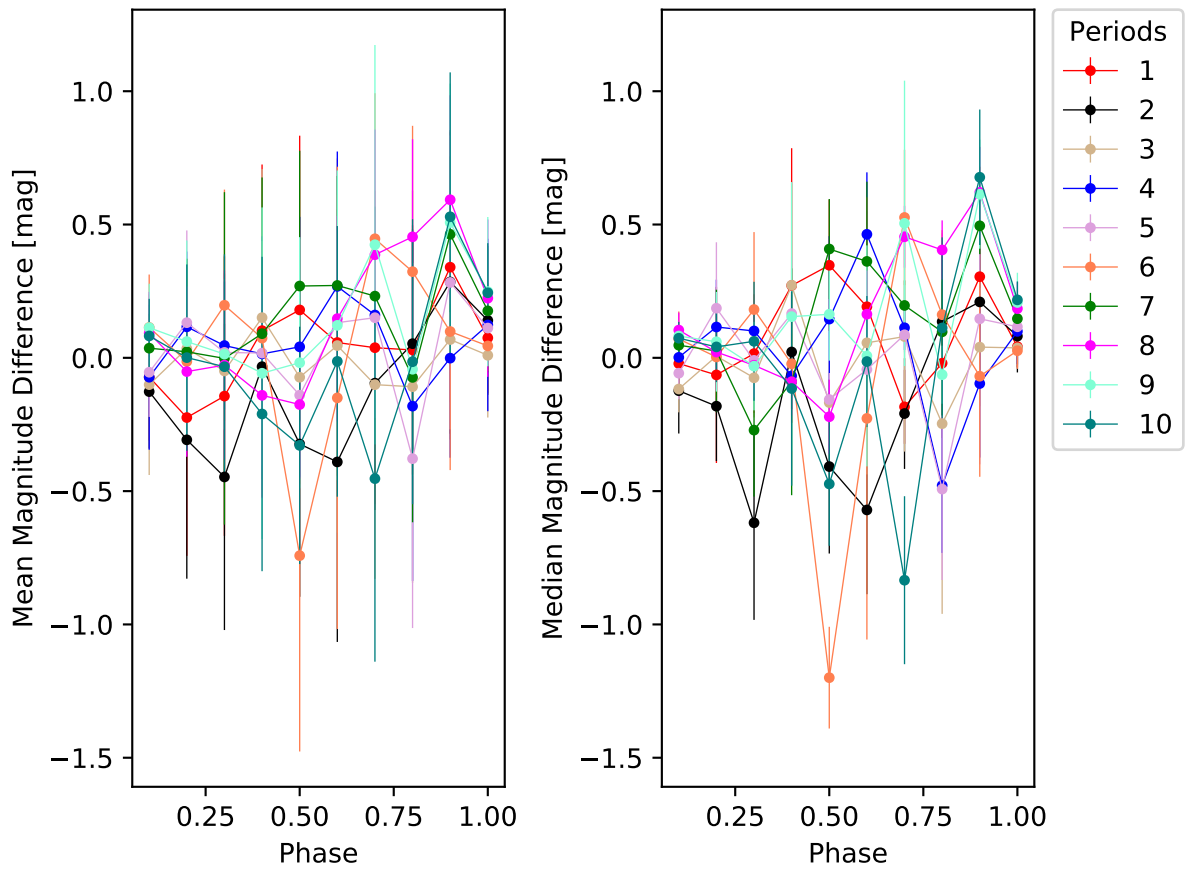


Figure 4.14: **Left:** Mean magnitude difference across phase space for N - consecutive dipo. **Right:** Median magnitude difference across phase space for N - consecutive dipo.

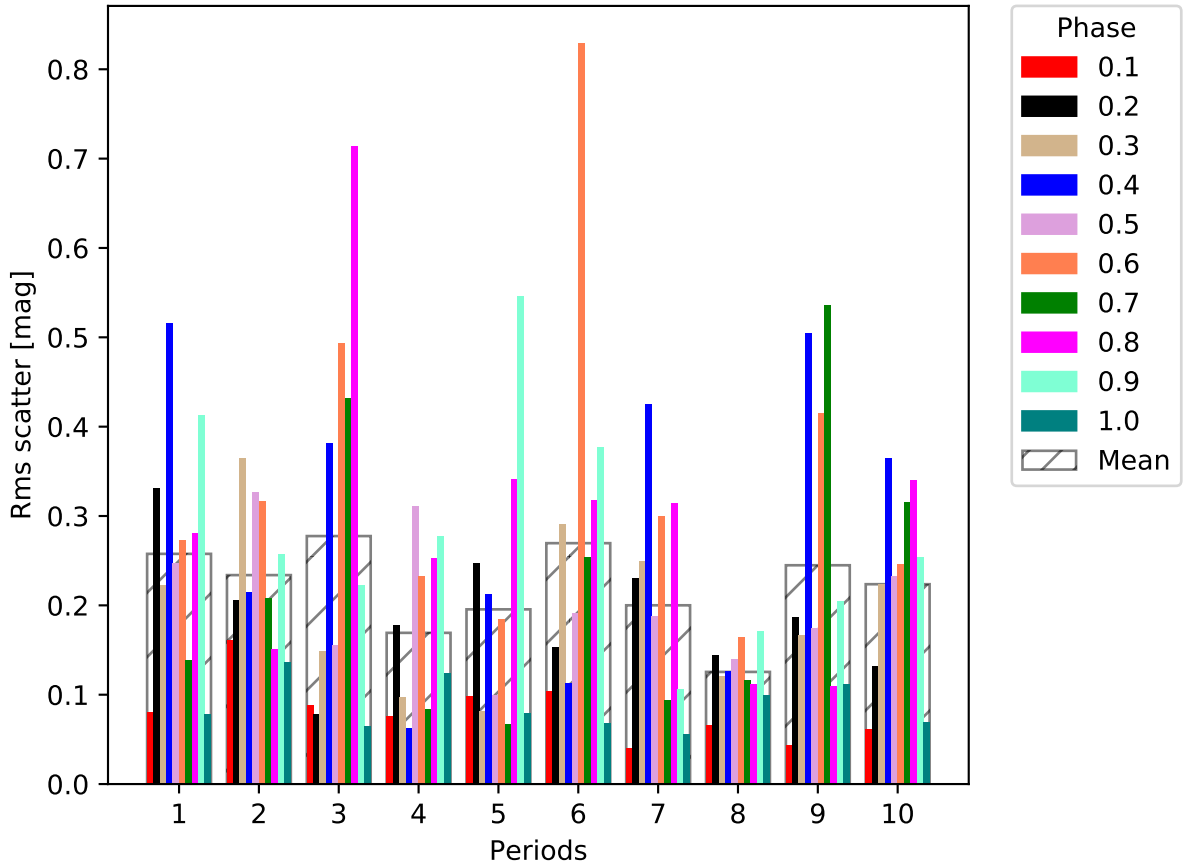


Figure 4.15: RMS scatter between consecutive dip events in phase space. The bin size is 0.1, with upper limit inclusive. Mean scatter is indicated in hatching.

for the value of the structure function with N , neither for a particular part of the phase space, nor when averaged over the entire period.

Starting from the beginning of the HOYS data, consecutive dips were numbered incrementally in units of the period of the source. Median magnitude differences were determined between dips for N equalling one and two, shown in the top and bottom plots in Fig. 4.16. Dips are labelled 'odd' and 'even' arbitrarily to better distinguish patterns that might arise from dip to dip. Even dips are shown by light red bars with cross hatching and odd by light blue bars with diagonal hatching. Any bars with no associated error indicate dips for which there is only one measurement.

One is able to see a random pattern of alternating dimming and brightening between 'odd' and 'even' dips, both for N equals one and two. This random nature of dip to dip events further supports the analysis that the orbital material held in the disk is homogeneous, showing no repeating structural patterns and moves through on a timescale less than the observed period.

Given the above found lack of correlation of column density from dip to dip, the total amount of material along the orbital path during each dip is investigated.

Assuming a constant line-of-sight thickness, the mass is proportional to the integrated depth of the V-band light curve for each dip. The results of this calculation are shown in Fig. 4.17. Using a trapezium interpolation between V-band data-points, the values

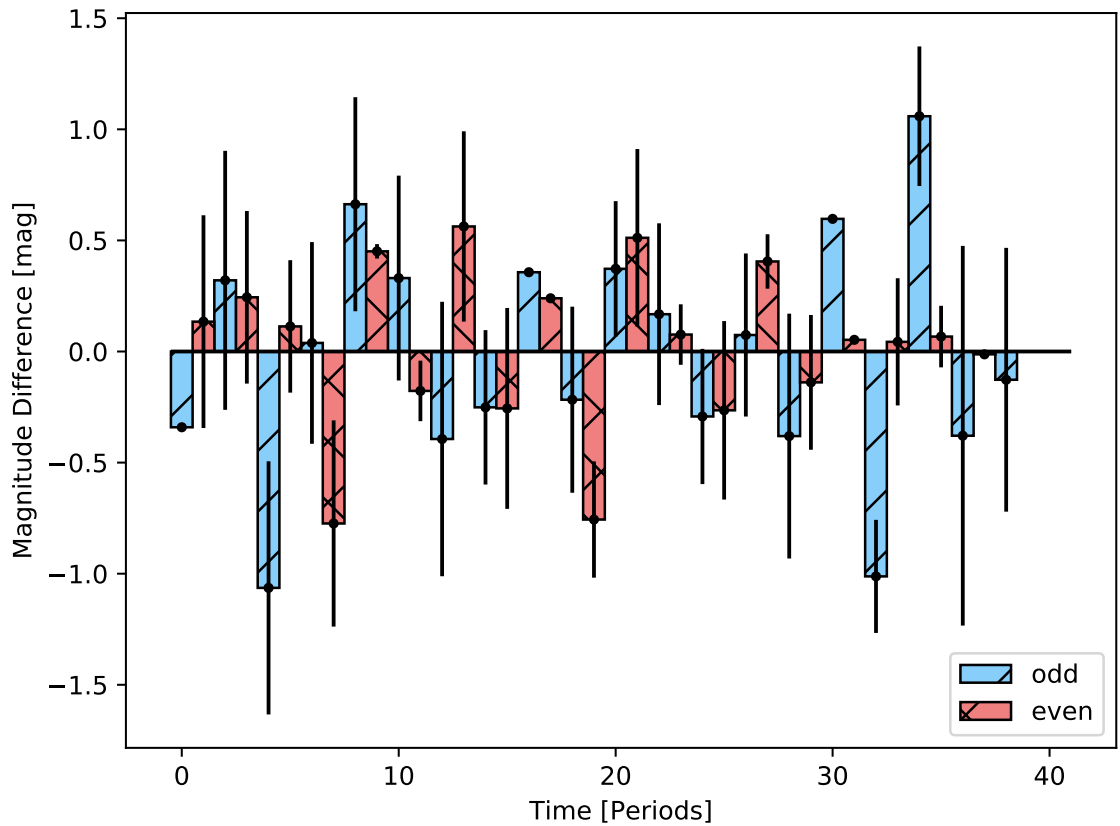
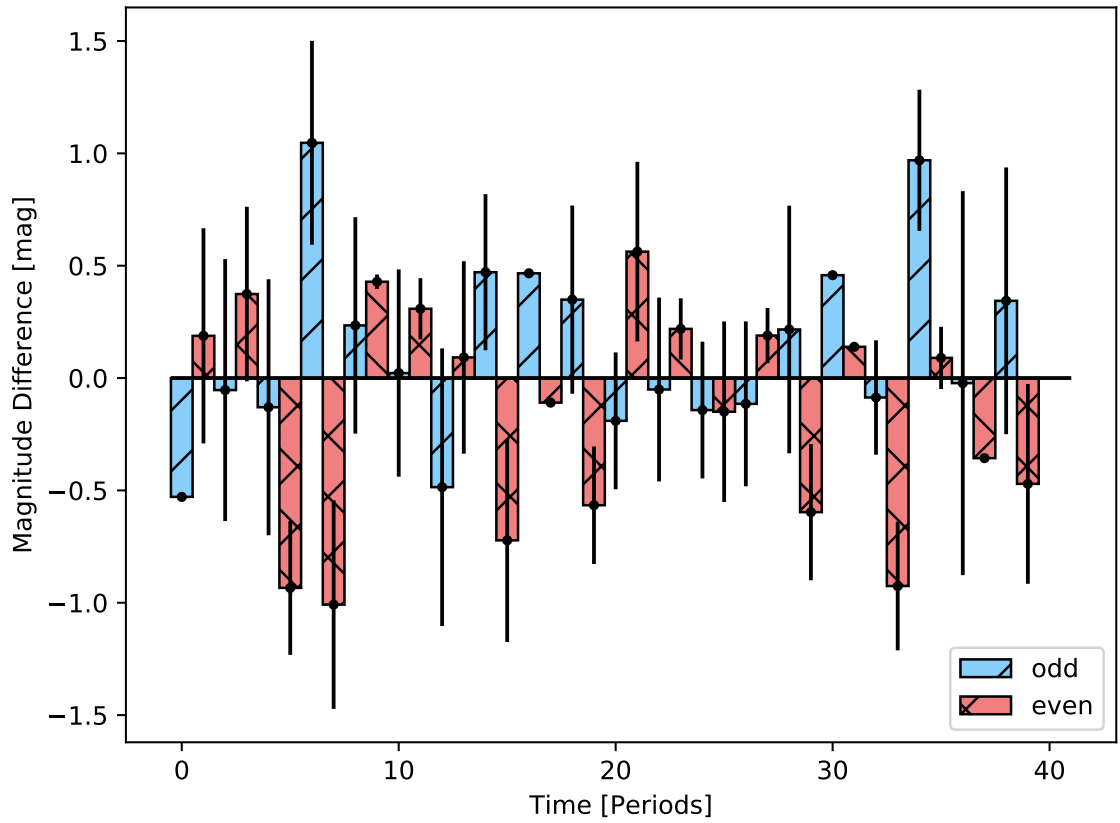


Figure 4.16: Average V-band magnitude difference (bars) and scatter (error-bars) in phase space in the dip depth between consecutive dips. For better visibility, different hatching styles are used to indicate 'odd' and 'even' periods, starting arbitrarily at the beginning of the HOYS data.

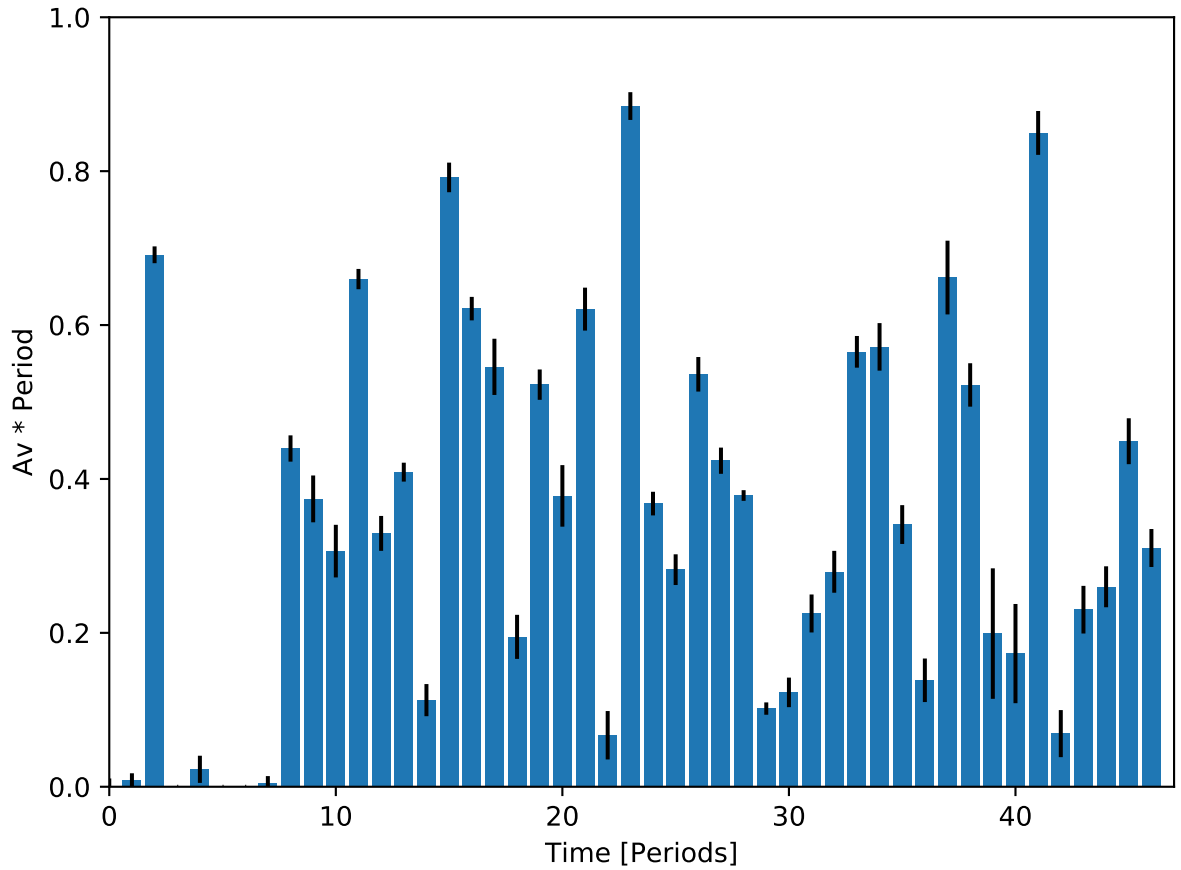


Figure 4.17: This plot shows the integrated column density times duration, a measure for the mass of material contained in the orbiting structure around V 1490 Cyg for the consecutive dips. The dips are numbered arbitrarily starting at our first available HOYS data. The value of one on the y-axis corresponds to about $2 \times 10^{-11} M_{\odot}$ or 0.5% of the lunar mass.

displayed in the figure may be determined. Error-bars are solely based on the photometric uncertainty and do not consider gaps in the data. As one can see, the amount of mass in the occulting structure varies by up to a factor of 10 for both mass increase and decrease. This again suggests that the material in the line-of-sight is moving in and out of the structure on timescales of the order of, or shorter than, the period of the occultations. The mass flow rate varies when averaged over one period, in agreement with the $R_c - H_\alpha$ and U-band variability discussed in previous sections.

Making some simple assumptions about the star and the geometry of the occulting structure, an order of magnitude estimate of the mass in each dip can be obtained. From the classification of the source as a low mass YSO (Ogura et al., 2002), V 1490 Cyg is assumed to have a central mass of $0.5 M_\odot$. For the above calculated period of 31.447 ± 0.011 d, the occulting material is held at roughly 0.25 AU from the central star.

Dimensions of the orbiting structure in the two directions perpendicular to the orbital path are assumed to be 0.05 AU. For dust scattering properties in agreement with $R_V = 5.0$ (see Chapter 4.5), a value of one in Fig. 4.17 may be converted to approximately $2 \times 10^{-11} M_\odot$. This value is approximately 0.5% of the lunar mass. The typical mass flow accretion rate of material through the structure in V 1490 Cyg is therefore on the order of $10^{-10} M_\odot/\text{yr}$. This value is consistent with the low levels of accretion seen in T Tauri stars (Alcalá et al., 2017).

4.5 Colour Dependence of Periodic Dips

The quasi-periodic dips in the light curve of V 1490 Cyg are potentially caused by orbiting material in the accretion disk. Accretion variability describes the fluctuations seen in both U and H_α filters. However, as variability occurs at longer timescales for B, V, R_c and I_c , another mechanism is assumed to be the cause.

Investigating V 1490 Cyg's behaviour in the V vs. $V - I_c$ parameter space allows for an analysis of the extinction properties of the occulting material in the line-of-sight during each dip. This follows Froebrich et al. (2018a) whereby the angle, α , is a measure of the slope, determined counter-clockwise from the horizontal.

Fitting a linear function, given by Eq. 4.2, to the N data-points in the $V - I_c$ vs. V colour-magnitude diagram gives the slope, indicated as a solid green line in Fig. 4.19. The fitting utilised a linear least-squares optimisation. α -values are converted into degrees to avoid the usage of large numerical values.

$$V = V_0 + \alpha (V - I_c) \quad (4.2)$$

Using a standard reddening law (Mathis, 1990), disk material made from normal ISM dust would have α -values between 60° ($R_V = 3.1$) and 66° ($R_V = 5.0$).

Exact values for α also depend on the filter transmission curves used in the observations. However, there will be a general trend of increasing α -values with increasing

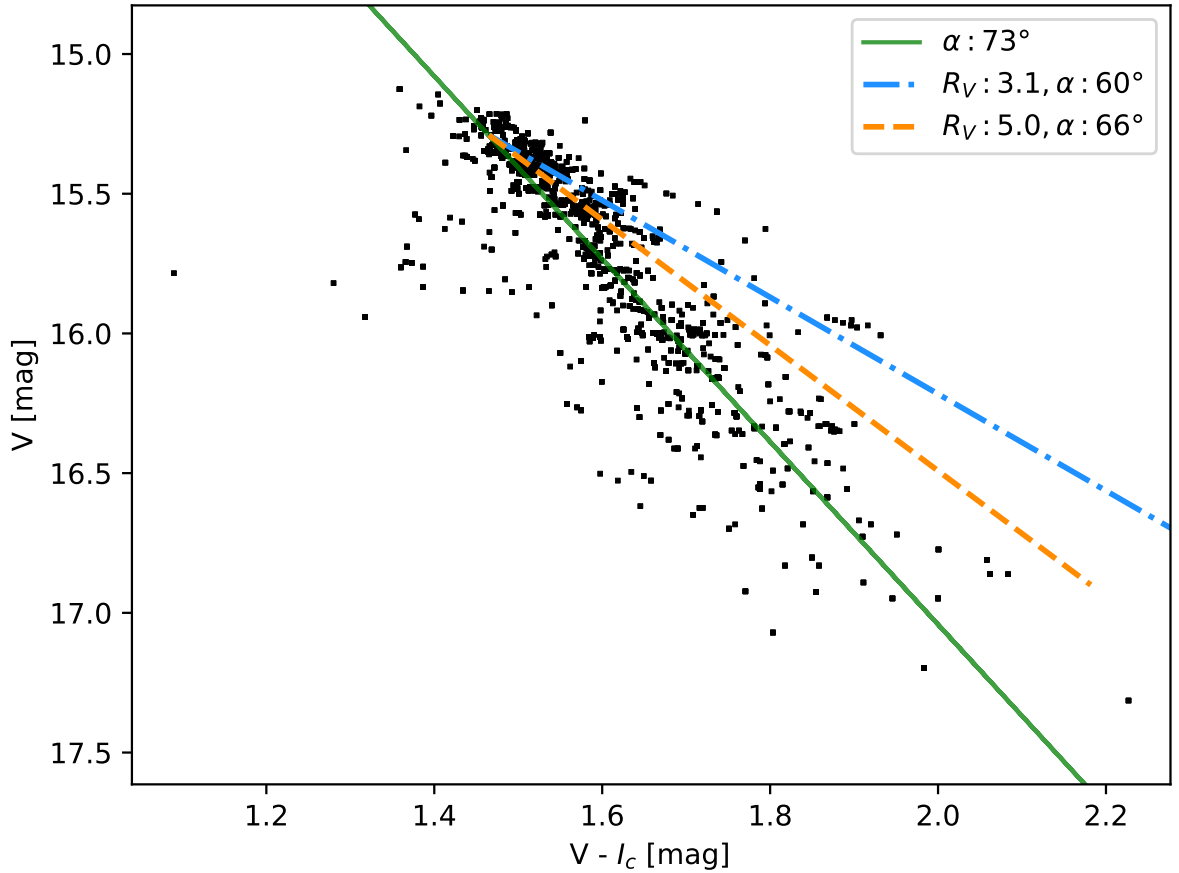


Figure 4.18: The V vs. $V - I_c$ colour magnitude plot for the HOYS data of V 1490 Cyg. The blue dash-dot line corresponds to behaviour expected for occultations by material with $R_V = 3.1$, while the orange dashed line is for $R_V = 5.0$. The solid green line indicates the determined angle for V 1490 Cyg of 73° .

typical grain size. Occultations by very large grains compared to the observed wavelengths, or by optically thick material should generate colour independent dimming ($\alpha = 90^\circ$). If occultations cause a change in the dominant source of the light observed, such as from direct light to scattered light, other colour changes, including bluening during deep dimming events can occur.

Light curves with $\alpha < 55^\circ$ are therefore not consistent with variability due to changes in extinction alone, but may be caused by changes in accretion rates or hot/cold surface spots (Froeblich et al., 2018a; Guo et al., 2018). Objects that show α approximately equal to 45° , change their brightness in the V-band but not at a detectable level in the I_c -band. This can in principle be caused by non-variable red sources which are at the detection limit in V but detected at high signal-to-noise in the I_c -band. Alternatively, these objects can be interpreted as sources with large fluctuations at visual wavelengths and small, undetected variations in the infrared.

Many sources will have properties that indicate a mix of more than one of these physical reasons for variability (Guo et al., 2018). Hence, such categories bounding the α -value are only suggestive of the main reason of variability for an object. Figure 4.18 shows the V vs. $V - I_c$ diagram for V 1490 Cyg.

Since the determined value of α can be very sensitive to small changes in the V and $V - I_c$ values, only high signal-to-noise measurements are included in this analysis. In particular, only V and I_c magnitudes that have a determined uncertainty of less than 0.05 mag after the colour correction (see Chapter 3.2.2) are included. Furthermore, since the object is constantly changing its brightness, the V and I_c data needs to be taken as simultaneously as possible, only pairs of V and I_c data taken within one day are used to determine α -values.

$$\alpha = \tan^{-1} \left(\frac{V_B - V_N}{(V_B - V_N) - (I_{cB} - I_{cN})} \right) \quad (4.3)$$

To further investigate the colour dependence of the occulting material, α was determined as a function of visual extinction for each observation N . A baseline brightness in V and I_c was established to determine α , representing the bright state of the source. All data taken at a phase within 0.1 from the phase zero point were selected, as determined in Chapter 4.1, and use their median magnitude as the baseline brightness for the source. This equates to 15.29 mag in V and 13.86 mag in I_c . Values of α were then determined for each observation through Eq. 4.3, where V_B and I_{cB} represent the baseline brightness in each filter and V_N and I_{cN} indicate the magnitude in V and I_c for each observation N . The uncertainty in α is determined from error propagation of the individual photometry errors obtained during the colour correction.

In Fig. 4.19, the α -values are plotted against the depth of the occultation in the V -band, the A_V of the occulting material. Only points that correspond to measurements taken at an occultation depth of more than 5 times the nominal uncertainty of the V -band data are included, i.e. when the dip is more than 0.25 mag deep. The median value for α is 73° with a scatter of 4° . This angle is systematically higher than what can be expected for normal interstellar dust grain dominated scattering. Hence, the disk material in V 1490 Cyg does show signs of the onset of grain growth in the higher column density material.

There is no significant systematic trend of α with A_V , the occulting material has the same scattering properties (within the measurement uncertainties) independent of the column density (or density) of the material or time, for an extinction above 0.25 mag in V . There are a few outlying points which are significantly away from the other data. These points occur at 'random' places in the light curve and thus are not caused by single, or multiple dip events with material with different scattering properties. Hence, the outliers are most likely caused by erroneous data where the initial magnitudes have been influenced by cosmic ray hits, or where the up to one day time gap between the V and I_c observations causes unrealistic values for α . As one can see in Fig. 4.4, significant brightness variations in the source can happen at sub one day timescales on occasion.

As noted above, small uncertainties in the V and I_c magnitudes can lead to large uncertainties in the α -value. The $V - I_c$ colour is used in the calibration of the magnitudes (see Chapter 3.2.2). Thus, if initially not exactly correct, the calibration will give systematically different magnitudes and hence might cause systematic and/or random offsets in the α -values determined. As evident from the light curves and Fig. 4.18, the $V - I_c$ colour of the source varies by a maximum of about 0.5 mag between the bright and faint state. To test the influence on the determination of α , the following experi-

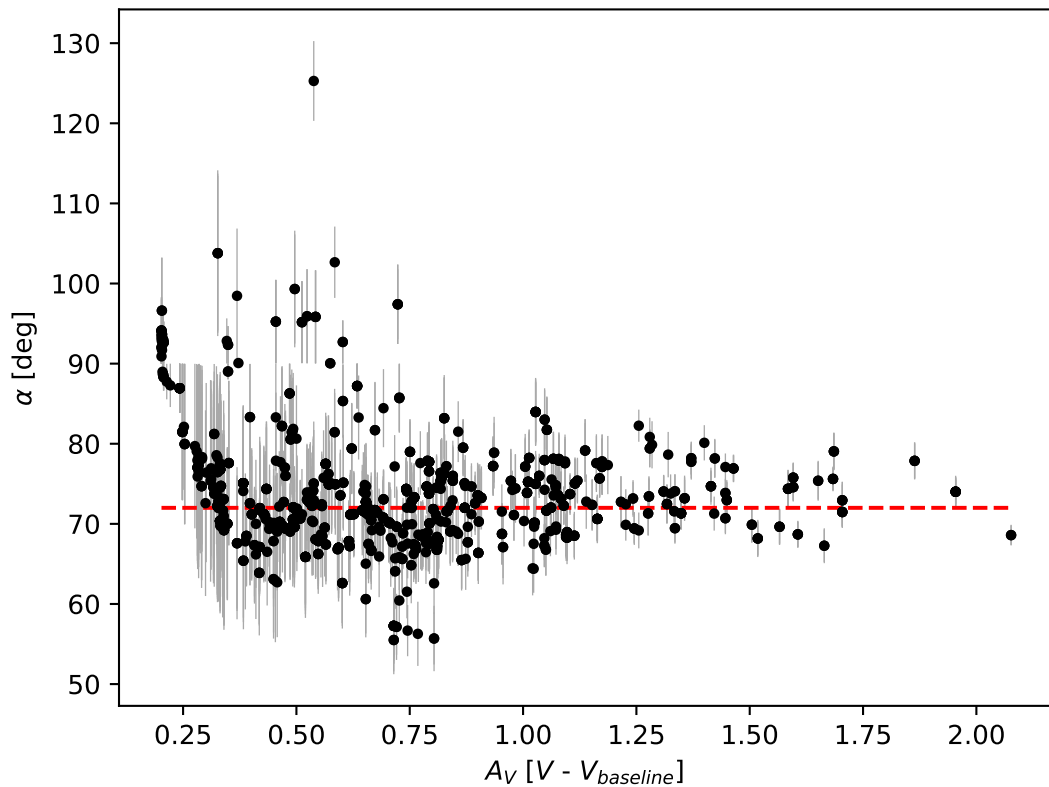
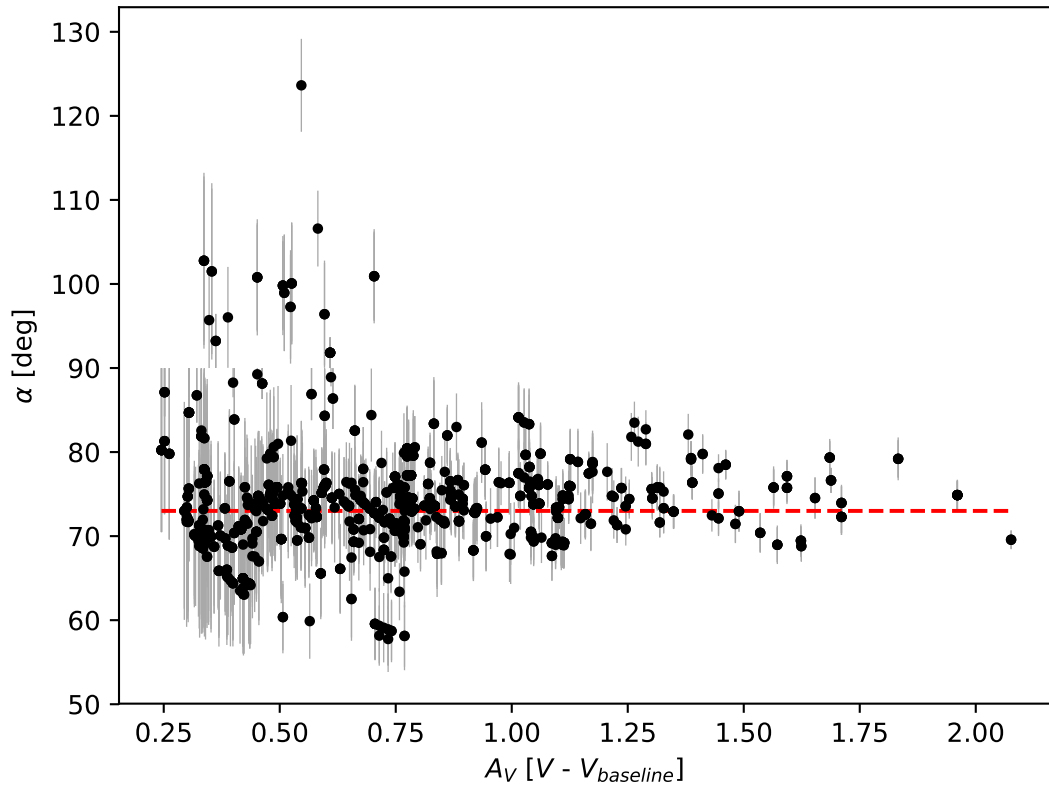


Figure 4.19: α -values in the V vs. $V - I_c$ parameter space during dips as a function of dip depth (A_V). Points were removed within 5σ of the V-band baseline of 15.29 mag. The red dashed line indicates the median α -value of $(73 \pm 4)^\circ$ for the top figure and $(72 \pm 4)^\circ$ for the bottom figure. The bottom figure shows the same analysis as the top for a colour correction with a systematic calibration offset, produced by overestimating the $V - I_c$ colour by 0.5 mag.

ment has been run.

The entire calibration procedure was re-run with a systematically overestimated $V - I_c$ colour by 0.5 mag; this is a worst case scenario. This of course has a systematic effect on the newly calibrated magnitudes of the star. Note that the colour dependence of the calibration is, however, rather weak (see Fig. 3.4). All α -values were then re-determined and compared to the original numbers. There are no significant changes to the scatter and uncertainties for α other than a systematic shift by 1° (to 72°) of the median value. Thus, the results for the scattering properties are robust, and the α -values do not suffer any systematic uncertainties bigger than 1° caused by the calibration procedure. These results may be seen in the bottom plot of Fig. 4.19.

A detailed look at Fig. 4.18 reveals that for dips of magnitude less than 15.6 mag in V , the scattering behaviour of the material is not following the same slope as determined for the high A_V material. A linear least-squares optimisation was performed of all low extinction points, finding that in the V vs. $V - I_c$ diagram they are consistent with $R_V = 5.0$ scattering material. This suggests that the material in the occulting structure consists of low column density material with roughly ISM dust properties. Embedded in this envelope are denser small scale structures that are made up of most likely larger dust grains. The scattering properties of the material are consistent and do not change over time.

Discussion

All data collation and subsequent analysis in Chapters 5.1 – 5.4 was completed by my supervisor, Dr. Dirk Froebrich. The discussion and interpretation of these sections are however my own. This analysis is needed, in combination with the work presented thus far, to ascertain the nature of V 1490 Cyg, which is discussed in Chapter 5.5.

5.1 Distance of V 1490 Cyg

V 1490 Cyg is assumed to belong to the large star forming region IC 5070 due to its projection onto it. The nebula has previously been estimated by various authors to be at a distance of approximately 600 pc (Reipurth and Schneider, 2008; Guieu et al., 2009). Now, through use of Gaia DR 2¹, this distance may be re-evaluated. V 1490 Cyg is identified by Gaia as Gaia DR2 2163139770169674112 and has a recorded Gmag value of 15.0771 ± 0.0344 mag. Its proper motion is given as -0.539 ± 0.377 mas/yr in RA and as -2.418 ± 0.370 mas/yr in DEC. This combined with a parallax of 0.4560 ± 0.2377 mas indicates a distance to the source of 2.2 kpc with a very high uncertainty. Such a large distance when compared with IC 5070 could indicate that the source is actually much further away and not associated with the nebula.

To investigate this disparity, all Gaia DR 2 sources within 20' of V 1490 Cyg were downloaded and examined. Limiting the selection to stars with a signal-to-noise (S/N) ratio of three or higher for the parallax, when plotting proper motions against distance, the IC 5070 region is identified as a distinct cluster. These plots are shown in Fig. 5.1 with members of IC 5070 having proper motions ranging from -0.35 to -2.00 mas/yr in RA and from -2.00 to -5.00 mas/yr in DEC. From the values determined by Gaia for V 1490 Cyg, the source appears to fit well within these parameter ranges of proper motion.

The cluster is however, not identifiable in proper motion space alone. IC 5070's over-

¹<https://www.cosmos.esa.int/web/gaia/data-release-2>

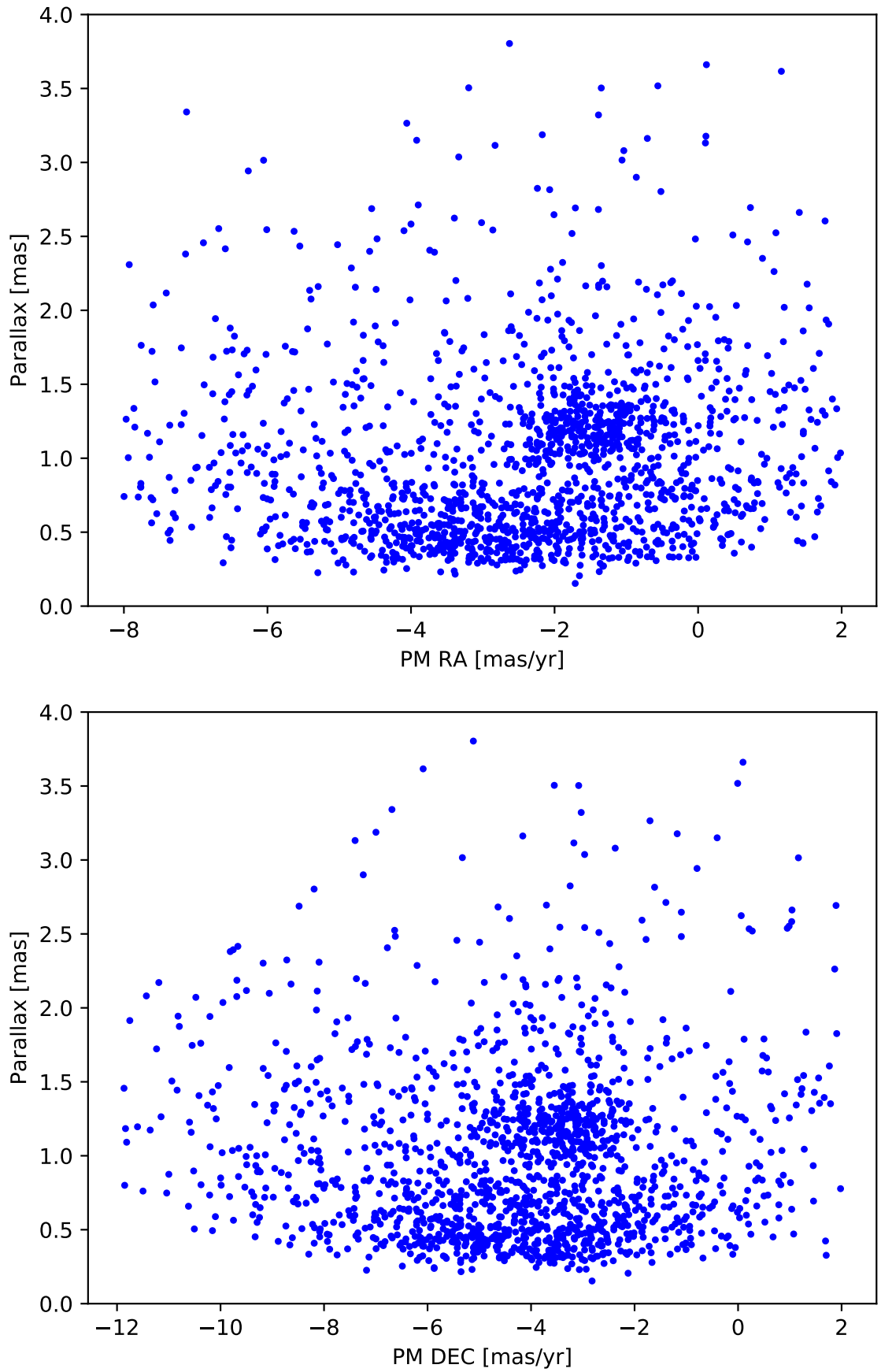


Figure 5.1: Gaia DR2 parallax vs. proper motion in RA (top) and DEC (bottom) of stars in the IC 5070 region with a parallax S/N ratio of better than 3. IC 5070 is identifiable as cluster of points with distinct proper motion and distance.

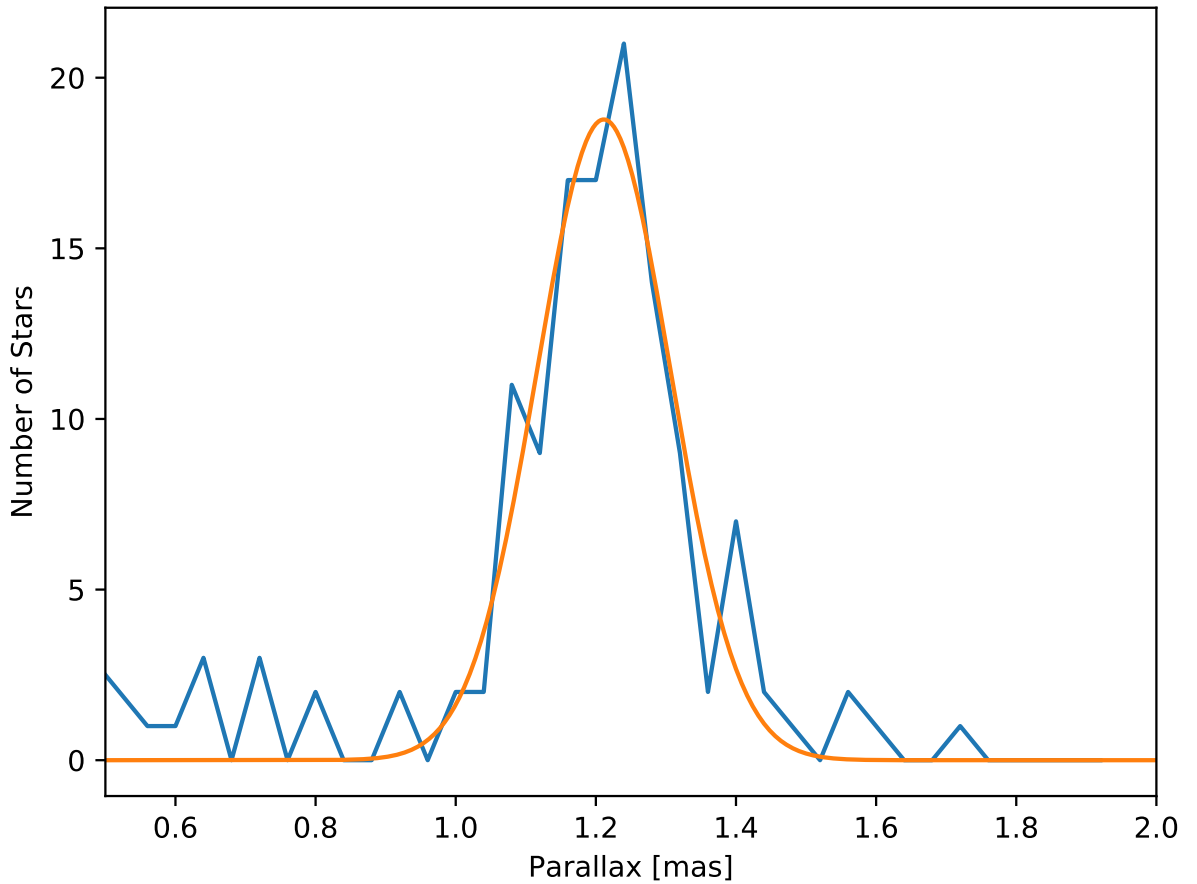


Figure 5.2: Distribution of Gaia DR2 parallaxes in the IC 5070 region with a parallax S/N ratio of better than 10 and proper motions corresponding of IC 5070 member stars. Over-plotted is a Gaussian fit to the data, indicating a mean parallax of 1.20 mas with a scatter of 0.09 mas.

density appears to extend from parallaxes of 1.0 to 1.5 mas. Fitting a Gaussian to the distribution gives a parallax of approximately 1.20 mas with a standard deviation of 0.09 mas. This was done for objects with a parallax S/N better than 10. The fitting may be seen in Fig. 5.2. Applying the suggested zero-point correction of -0.0523 mas (Leung and Bovy, 2019) indicates a distance for IC 5070 of approximately 870^{+70}_{-55} pc.

Therefore, V 1490 Cyg has a parallax different to the average cluster member with a very low S/N ratio. To examine this further, typical parallax errors of a subset of 49 stars were determined. All selected stars have Gmag values within 1 mag of V 1490 Cyg with proper motions for RA and DEC in the ranges stated above for potential association with IC 5070. The median parallax error was found to be 0.046 mas/yr with a scatter of 0.021 mas/yr. Hence the parallax error of 0.2377 mas/yr for V 1490 Cyg represents an outlier of greater than 9σ . The total number of Gaia observations of the source, when compared to stars in the same field, is not abnormal. Hence there is no general issue with crowding in this field. However, the astrometric excess noise and all other quality indicators are much higher for this object. The reduced unit weight error (ruwe) was found to be 5.19, with low_ruwe set as false, confirming that the Gaia resolution was poor. This indicates that the object's parallax measurements could be influenced by a variety of factors.

V 1490 Cyg is shown to be highly variable and very red in colour. This appears to be the most likely cause of error and will be confirmed with the advent of a future Gaia Data Release. Other potential causes are crowding for this source, caused by the scan angles used so far, or the source being a binary. The binary interpretation will be briefly discussed in Chapter 5.2. Furthermore, the object's photo-centre position could change due to the variability which might confuse the Gaia measurement.

Thus, the Gaia DR2 parallax of the source cannot be trusted and the above determined IC 5070 distance of 870^{+70}_{-55} pc is used for both the region and the source in this thesis.

5.2 Potential Binarity of V 1490 Cyg

The large Gaia parallax error of V 1490 Cyg indicates that the star could be a binary, unresolved in the optical images of this data-set. Investigation of the highest resolution imaging data available for the source, reveals three faint, red near infrared (NIR) objects around the star. The data comes from the UKIRT Infrared Deep Sky Galactic Plane Survey (UGPS) (Lucas et al., 2008), with the NIR images showing separations of 5.6, 2.7 and 2.5'' for the three objects. However, they are fainter than V 1490 Cyg by 2.5, 4.5 and 7.0 mag in K, and by 3.6 and 5.6 mag in J, with the closest source having no J detection.

V 1490 Cyg itself has the maximum possible value of $p_{\text{star}} = +0.999999$, indicating its point spread function (PSF) is consistent with a single unresolved source. The ellipticities in all three filters (JHK) are between 0.07 and 0.10. This indicates that the source is not elongated at a level above 0.1 of the full width half maximum of the PSF. The seeing in the images is about 0.56''. Thus, any companion, of equal brightness, not detectable in UGPS would have to be closer than 0.05'' or 44 AU maximum separation from the source, at the adopted distance of 870 pc.

The period of 31.447 days indicates material at sub-AU distance from the star, as discussed in Chapter 4.4. Hence, the periodic variability of the source does not support a wide binary scenario for stars of comparable luminosities. In the V-band, occultations in EB systems can reach depths of up to 2 mag. For equal luminosity binary objects with one occulted partner, maximum dip depth should only be approximately 0.75 mag. For stars of unequal luminosity, the dips can be deeper.

In such cases, the colour of the occulted system should eventually be dominated by the colour of the fainter object. However, as shown in Chapter 4.5, there is no indication that the dimming is caused by anything other than interstellar dust grains of homogeneous scattering properties. In particular for deep dips, there is no deviation in the changes of colour from the prediction of extinction from dust. Thus, it seems highly unlikely that, if there is a wide companion, it is contributing a sizeable fraction of the system luminosity.

5.3 Literature NIR and MIR data for V 1490 Cyg

To classify the evolutionary stage of the source, NIR and mid infrared (MIR) photometry of the source was collected from the literature. This data is summarised in Table 5.1 with the analysis taking place below in Chapter 5.4. The NIR photometry and observing dates from 2MASS (Skrutskie et al., 2006), UGPS (Lucas et al., 2008) data release DR 11, as well as the MIR observations from NEOWISE (Mainzer et al., 2011, 2014) in the W1 and W2 bands from the WISE satellite (Wright et al., 2010) were extracted.

For the latter, all NEOWISE measurements have been averaged, taken over the usually one to three day repeated visits for the source and with the RMS used as the uncertainty. The individual NEOWISE visits are too short to see any changes related to the dipping behaviour. Additionally, for completeness, WISE photometry released from the WISE all sky catalogue (Cutri and et al., 2012) and the ALLWISE catalogue (Cutri and et al., 2013), as well as the Spitzer IRAC and MIPS photometry presented in Guieu et al. (2009) and Rebull et al. (2011) has been obtained. For those additional data, no actual observing dates are available in the papers.

Due to the variability of V 1490 Cyg, only the data shown in the upper section of the table should be used to classify the source. These are the data for which there is a known observing date, which is particularly important for the shorter wavelength data where the extinction is higher. As there is no contemporary optical data to determine the depth of extinction during past dipping events, only photometry taken during the phase of the light curve where the object is most likely at its maximum brightness should be used. Considering the folded light curves in Figs. 4.5, 4.6 and the period of 31.447 ± 0.011 days determined in Chapter 4.1, the phase and its uncertainty for all NIR and MIR data with known observing dates have been estimated. The star is considered to be in its bright state if the phase is within 0.15 from zero/one. These measurements are highlighted in Table 5.1 in bold face.

5.4 Evolutionary Stage of V 1490 Cyg

To establish the evolutionary stage of the source, NIR and MIR magnitudes had to be estimated, uninfluenced by the variable circumstellar extinction. It may be seen from Table 5.1 that none of the available NIR data has been taken near the bright state of the source, as defined in Chapter 4.1. Magnitude variations of the four potential observations near maximum brightness in bands W1/W2 are of the order of several tenths of a magnitude. As evident in the folded light curves in Figs. 4.5 and 4.6, the source can vary quite significantly, even for observations close to its bright phase. Hence the brightest of the JHK/W1/W2 magnitudes are used for classification. Resulting colours are, however, potentially uncertain by a few tenths of a magnitude. Similarly, the brightest of the W3/W4 measurements from the WISE all sky and ALLWISE catalogues are chosen. Therefore, colours of $H - K = 0.37$ mag, $W1 - W2 = 0.43$ mag and $W3 - W4 = 2.1$ mag may be determined.

According to Koenig and Leisawitz (2014), this places the source at the blue end of

Table 5.1: Summary of literature NIR/MIR data for V 1490 Cyg. A list of the Julian date of the observations, the filter/band the observations are in, the magnitude and uncertainty, the survey the data is taken from and the phase and its uncertainty for the observation. The top portion of the table lists data with available observing dates, while in the bottom section time averaged WISE and Spitzer photometry is listed for completeness. The NEOWISE data is averaged over the 1 – 3 days for each sequence of visits. The phase has been determined following the period determined in Chapter 4.1. The uncertainty in the phase has been propagated from the nominal 15 minute uncertainty in the period. All magnitudes measured within 0.15 of phase zero are highlighted in bold, to indicate measurements that are most likely less influenced by the unknown variable circumstellar extinction.

Date [JD]	Filter	mag	Δ mag	Survey	Phase	Δ Phase
2451707.8263	J	11.85	0.023	2MASS	0.206	0.078
2451707.8263	H	11.008	0.032	2MASS	0.206	0.078
2451707.8263	K	10.637	0.026	2MASS	0.206	0.078
2457589.9499	J	12.0472	0.0006	UGPS	0.256	0.013
2457589.9555	H	11.0429	0.0004	UGPS	0.256	0.013
2457589.9597	K	10.7314	0.0006	UGPS	0.256	0.013
2455861.7314	K	10.8222	0.0006	UGPS	0.299	0.032
2456809.4858	W1	9.9188	0.0622	NEOWISE	0.437	0.021
2456809.4858	W2	9.449	0.0258	NEOWISE	0.437	0.021
2456987.9896	W1	10.225	0.118	NEOWISE	0.113	0.019
2456987.9896	W2	9.649	0.0705	NEOWISE	0.113	0.019
2457171.2939	W1	10.057	0.03	NEOWISE	0.942	0.017
2457171.2939	W2	9.581	0.0243	NEOWISE	0.942	0.017
2457346.0040	W1	10.061	0.015	NEOWISE	0.498	0.015
2457346.0040	W2	9.536	0.0346	NEOWISE	0.498	0.015
2457349.4515	W1	10.006	0.022	NEOWISE	0.608	0.015
2457349.4515	W2	9.5	0.0182	NEOWISE	0.608	0.015
2457535.4401	W1	10.191	0.057	NEOWISE	0.522	0.013
2457535.4401	W2	9.646	0.0279	NEOWISE	0.522	0.013
2457538.7336	W1	10.04	0.032	NEOWISE	0.627	0.013
2457538.7336	W2	9.493	0.0171	NEOWISE	0.627	0.013
2457708.6578	W1	9.9273	0.0701	NEOWISE	0.030	0.011
2457708.6578	W2	9.4918	0.0551	NEOWISE	0.030	0.011
2457902.4970	W1	9.9078	0.0227	NEOWISE	0.194	0.009
2457902.4970	W2	9.4613	0.0146	NEOWISE	0.194	0.009
2458069.3243	W1	9.9929	0.0441	NEOWISE	0.500	0.007
2458069.3243	W2	9.4577	0.0568	NEOWISE	0.500	0.007
2458266.6522	W1	9.873	0.0221	NEOWISE	0.774	0.005
2458266.6522	W2	9.3924	0.0196	NEOWISE	0.774	0.005
2458429.9023	W1	9.8158	0.0257	NEOWISE	0.966	0.003
2458429.9023	W2	9.3902	0.0408	NEOWISE	0.966	0.003
	W1	9.929	0.023	WISE all sky		
	W2	9.412	0.021	WISE all sky		
	W3	7.300	0.028	WISE all sky		
	W4	5.209	0.036	WISE all sky		
	W1	9.937	0.023	AllWISE		
	W2	9.443	0.021	AllWISE		
	W3	7.427	0.029	AllWISE		
	W4	5.163	0.037	AllWISE		
	3.6	9.956		IRAC		
	4.5	9.581		IRAC		
	5.8	9.036		IRAC		
	8.0	8.211		IRAC		
	24	5.387		MIPS		

the classification as a CTTS in the $W1 - W2$ vs. $H - K$ diagram. In the $W3 - W4$ vs. $W1 - W2$ diagram, the source sits on the borderline between CTTS and transition disk objects. Using the WISE data and following Majaess (2013), the slope (α_{SED}) of the spectral energy distribution was determined as -0.67 . This again places the source in the CTTS category.

Using the intrinsic colours, $B - V$ and $V - I_c$, an estimate to the spectral type of V 1490 Cyg can be determined. Data taken from Fitzgerald (1970), and Ducati et al. (2001), provides UBV measurements for spectral classes O5 to M8. By converting $V - I$ data to the Cousins system, using relations found by Bessell (1979), the HOYS data allows for a rough guess at a spectral class of V 1490 Cyg, assuming its spectral class remains consistent until it reaches the main sequence. Taking the bright measurements of V 1490 Cyg for B , V and I_c , given in table 4.1, colours of $B - V = 1.57$ and $V - I_c = 1.40$ can be found. These values roughly yield a spectral type of M0 for V 1490 Cyg.

The spectra from LCOGT in Chapter 3.3 allow use of the H_α equivalent width to classify the source. In the six spectra obtained, the equivalent width of the H_α line varies between -3.2 \AA and -8.6 \AA . The most widely used dividing line between CTTS and WTTS is -10 \AA (Martín, 1998). However, this is not a fixed value due to the variability of the line. The source is, however, still accreting and all available accretion rate indicators show variability. The H_α EW (see Fig. 3.7 and Table 3.2) is clearly variable by at least a factor of two. Furthermore, the $R_c - H_\alpha$ magnitudes also vary by at least one magnitude. Finally, as can be seen in Fig. 4.9, the U-band is highly variable by at least ± 2 mag, even on very short timescales of hours. Since the U-band excess is generally acknowledged as one of the best tracers of accretion rate (Gullbring et al., 1998; Calvet and Gullbring, 1998; Herczeg and Hillenbrand, 2008), this indicates strongly variable accretion in V 1490 Cyg.

Thus, V 1490 Cyg is most likely a CTTS, with a currently low, but variable accretion rate. It is potentially at the start of the transition into a WTTS or transition disk object.

5.5 The Nature of V 1490 Cyg

The analysis presented in Chapters 4.1 – 5.4 shows that V 1490 Cyg exhibits semi-periodic occultation events of dust in the inner accretion disk, at a distance of 0.25 AU from the source. The occulting material displays ISM properties at low A_V and shows grain growth at high column densities. The source is still accreting and is at the borderline between CTTS/WTTS or transition disk objects.

Below, three possible explanations for the nature of the source are presented, listed in order of decreasing probability: i) A protoplanet-induced disk warp; ii) A magnetically-induced disk warp; iii) The Hill sphere of an accreting protoplanet.

Attempting the verification or falsification of these explanations will require high resolution spectroscopy over several orbital periods which is strongly encouraged. This however, could be extremely difficult to achieve as the star is young and highly variable, even on short timescales.

5.5.1 Protoplanet-induced Disk Warp

Recent Atacama Large Millimeter/sub-millimeter Array (ALMA) observations have discovered several warped protostellar disk systems (Sakai et al., 2019). For some of these systems, observations rule out the influence of a secondary star, potentially suggesting unseen protoplanets to be the cause of the warping (Nealon et al., 2018). A protoplanet that is capable of driving warping features in the disk would be required to maintain an orbit that is inclined to the disk plane over long timescales. This is, however, in contradiction with current planet formation theory which assumes a flat protoplanetary disk. One possible explanation would be a stellar binary companion, co-orbiting with V 1490 Cyg. However, a stellar mass would disrupt the disk if within, or close to, the outer disk.

A co-planar protoplanet could become inclined, or eccentric, during, or after, formation, whereby planet-planet interactions are able to move a protoplanet to an inclined orbit (Nagasawa et al., 2008). Measurements of disk inclination in objects such as TW Hya hint at a small warp or misalignment, at distances less than 1 AU for even minor deviations in inclination from the disk plane (Qi et al., 2004; Pontoppidan et al., 2008; Hughes et al., 2011). Additionally, there is some evidence indicating large inner disc misalignment's with the outer disc, as in the case of both AA Tau (Loomis et al., 2017) and other YSOs (Benisty et al., 2018).

Chapter 4.5 showed that the material in the occulting structure appears to consist of low column density material, with roughly ISM dust properties. Embedded in this envelope are denser, small-scale structures that are most likely composed of larger dust grains. This, combined with the fact that the source is situated in a ~ 3 Myr star forming region (Bally et al., 2008) suggests that planet formation should be ongoing.

The source exhibits dips across the majority of the observed periods, demonstrating semi-stability in the occulting structure. Orbital resonance between the disk and an inclined orbiting protoplanet could cause a build up of material at the distances observed. Such a protoplanet could be closer to, or further from the source in relation to the observed orbiting structure, depending on the resonance ratio.

5.5.2 Magnetically-induced Disk Warp

The regular dips exhibited by V 1490 Cyg suggests it could be an AA Tau type source. However, its period of 31.447 days is particularly long when compared with other AA Tau type objects. Average rotational periods of CCTSs are 3 days – 4 days (Alencar et al., 2010), with AA Tau itself having a period of 8.2 days (Bouvier et al., 2003). Hence, typical values range between 3 days – 10 days.

In AA Tau type objects, the periodic dips are caused by a warp of the inner disk due to a misalignment between the rotation axes of both the disk and the star. The warp is therefore located at the co-rotation radius of the disk (Bouvier et al., 1999, 2007; Cody et al., 2014; McGinnis et al., 2015). Assuming a dipole magnetic field aligned with the star's rotation axis, material in the disk would be magnetically displaced from the disk's plane and into the line-of-sight. If V 1490 Cyg is seen at a high inclination, the

inner disk warp will occult the stellar photosphere periodically, causing flux dips in the star's light curve. This obscuration could then explain such dimming behaviour as seen in Chapter 4.1.

However, for V 1490 Cyg to have a warped disk due to misalignment, the source would have to be a slow rotator. This would enable the co-rotation radius, and hence the disk warp, to occur further out than is seen for AA Tau.

5.5.3 Hill Sphere of Accreting Protoplanet

A third scenario, describing the observed semi-periodic variability, comes from material held in orbit, not by a magnetic structure, but by a more massive object. A protoplanet located at distances close to the central star within the disk will gravitationally exert influence on the disk material around it. The occultations observed could then be caused by material in the Hill sphere around this protoplanet.

The Hill sphere would present as an oblate spheroid of material, gravitationally bound to the protoplanet within the disk. Modelling by Papaloizou and Nelson (2005) suggests that for protoplanetary mass $\sim 0.1 M_J$, a rapid accretion phase begins. This is a similar mass to that for which either significant perturbation to the protoplanetary disk through local mass accretion or disk-planet interaction begins (Nelson et al., 2000).

On its own, structures of the mass observed in Chapter 4.4 will not survive for more than one orbit due to shearing. The periodic dips are stable in phase, if not in structure, for more than 40 orbits. This explanation is the least likely case as the duration of dips observed for the source span more than half the period in many cases. The deepest part of the occultations also move significantly in phase, disagreeing with predictions for this scenario.

Conclusions

In this thesis, a long-term, high cadence, multi-filter analysis of structures within the inner protostellar disk was performed. Utilising a largely amateur network to monitor the target source, reliable data were produced for analysis. Despite an in-homogeneous photometric data-set, accurate calibration may be achieved when a sufficient number of images, and number of non-variable sources in the fields, are available. Through a novel calibration technique, accurate photometry of 1 – 3 percent photometric error is achievable, overcoming colour-terms caused by various telescopes and filters used, alongside poor observing conditions such as thin/thick cirrus clouds.

The Orion variable, V 1490 Cyg, is actually a semi-periodic occulter, most likely caused by a warped disk due to an inclined protoplanetary orbit. Other causes investigated include magnetically-induced disk warping and a Hill sphere scenario around a protoplanet. A mean period of 31.447 ± 0.011 days was determined for V, R_c and I_c filters using a Lomb-Scargle periodogram search, yielding a distance to the orbiting material of ~ 0.25 AU. Variability was seen to occur on similar timescales for B, V, R_c and I_c data. However, U and R_c – H_α showed more extreme variation on timescales of hours to days. Such high variability suggests that the source is still accreting.

An analysis on the column density distribution of consecutive dips, constrains the timescale on which material is moved into, or out of, the orbiting structure. No significant trends were observed in the structure function, with the amount of mass in the occulting structure seen to vary by up to a factor of 10 for both mass increase and decrease. This suggests that the material in the line-of-sight is moving in and out of the structure on timescales of the order of, or shorter than, the period of the occultations. The mass flow rate varies by typically a factor of a few when averaged over one period, with the typical accretion rate of V 1490 Cyg found of the order $10^{-10} M_{\odot}/\text{yr}$. This is consistent with low levels of accretion as seen in other T-Tauri stars. The rate is a lower limit, assuming only the material in the observable structure contributes to the accretion rate; though caution should be used when relating eclipse depth changes alone to the accretion rate.

Investigating the orbiting structure in V vs. V – I_c parameter space, suggests that

the material in the occulting structure consists of low column density material, with roughly ISM dust properties. Embedded in this envelope are denser, small-scale structures, that are most likely composed of larger dust grains. The scattering properties of this material are consistent and do not change over time. Using measurements from Gaia DR2, an accurate distance to IC 5070 of 870^{+70}_{-55} pc was determined. Due to extremely high parallax error for V 1490 Cyg, the Gaia data for the source are unable to be trusted and the distance to IC 5070 was also assumed for V 1490 Cyg. Performing a colour analysis for NIR and MIR data taken from literature, most likely places V 1490 Cyg as a CTTS, with a currently low, but variable accretion rate. It is potentially at the start of the transition into a WTTS or transition disk object.

This analysis has shown that for quasi- or fully periodic variable stars, a vast amount of information is available. The HOYS data-set may be explored for other similar objects, based on what has been done for this source.

Bibliography

- Alcalá, J. M., Manara, C. F., Natta, A., Frasca, A., Testi, L., Nisini, B., Stelzer, B., Williams, J. P., Antonucci, S., Biazzo, K., Covino, E., Esposito, M., Getman, F., and Rigliaco, E. (2017). X-shooter spectroscopy of young stellar objects in Lupus. Accretion properties of class II and transitional objects. *A&A*, 600:A20.
- Alencar, S. H. P., Teixeira, P. S., Guimarães, M. M., McGinnis, P. T., Gameiro, J. F., Bouvier, J., Aigrain, S., Flaccomio, E., and Favata, F. (2010). Accretion dynamics and disk evolution in NGC 2264: a study based on CoRoT photometric observations. *A&A*, 519:A88.
- André, P. (1995). Low-Mass Protostars and Protostellar Stages. *Ap&SS*, 224(1-2):29–42.
- Andre, P., Ward-Thompson, D., and Barsony, M. (2000). From Prestellar Cores to Protostars: the Initial Conditions of Star Formation. In Mannings, V., Boss, A. P., and Russell, S. S., editors, *Protostars and Planets IV*, page 59.
- Andrews, S. M. and Williams, J. P. (2005). Circumstellar Dust Disks in Taurus-Auriga: The Submillimeter Perspective. *ApJ*, 631(2):1134–1160.
- Andrews, S. M. and Williams, J. P. (2007a). A Submillimeter View of Circumstellar Dust Disks in ρ Ophiuchi. *ApJ*, 671(2):1800–1812.
- Andrews, S. M. and Williams, J. P. (2007b). High-Resolution Submillimeter Constraints on Circumstellar Disk Structure. *ApJ*, 659(1):705–728.
- Ansdell, M., Gaidos, E., Rappaport, S. A., Jacobs, T. L., LaCourse, D. M., Jek, K. J., Mann, A. W., Wyatt, M. C., Kennedy, G., Williams, J. P., and Boyajian, T. S. (2016). Young “Dipper” Stars in Upper Sco and Oph Observed by K2. *ApJ*, 816(2):69.
- Arce, H. G., Shepherd, D., Gueth, F., Lee, C. F., Bachiller, R., Rosen, A., and Beuther, H. (2007). Molecular Outflows in Low- and High-Mass Star-forming Regions. In Reipurth, B., Jewitt, D., and Keil, K., editors, *Protostars and Planets V*, page 245.
- Arzamasskiy, L. and Rafikov, R. R. (2018). Disk Accretion Driven by Spiral Shocks. *ApJ*, 854:84.
- Audard, M., Ábrahám, P., Dunham, M. M., Green, J. D., Grosso, N., Hamaguchi, K., Kastner, J. H., Kóspál, A., Lodato, G., Romanova, M. M., Skinner, S. L., Vorobyov, E. I., and Zhu, Z. (2014). Episodic Accretion in Young Stars. In Beuther, H., Klessen, R. S., Dullemond, C. P., and Henning, T., editors, *Protostars and Planets VI*, page 387.

- Bacher, A., Kimeswenger, S., and Teutsch, P. (2005). Photometry from online Digitized Sky Survey plates. *MNRAS*, 362(2):542–548.
- Bachiller, R. and Tafalla, M. (1999). Bipolar Molecular Outflows. In Lada, C. J. and Kylafis, N. D., editors, *NATO Advanced Science Institutes (ASI) Series C*, volume 540, page 227.
- Bally, J., Walawender, J., Johnstone, D., Kirk, H., and Goodman, A. (2008). *The Perseus Cloud*, page 308. Astronomical Society of the Pacific.
- Benisty, M., Juhász, A., Facchini, S., Pinilla, P., de Boer, J., Pérez, L. M., Keppler, M., Muro-Arena, G., Villenave, M., Andrews, S., Dominik, C., Dullemond, C. P., Galenne, A., Garufi, A., Ginski, C., and Isella, A. (2018). Shadows and asymmetries in the T Tauri disk HD 143006: evidence for a misaligned inner disk. *A&A*, 619:A171.
- Benz, W., Ida, S., Alibert, Y., Lin, D., and Mordasini, C. (2014). Planet Population Synthesis. In Beuther, H., Klessen, R. S., Dullemond, C. P., and Henning, T., editors, *Protostars and Planets VI*, page 691.
- Bertin, E. and Arnouts, S. (1996). SExtractor: Software for source extraction. *A&AS*, 117:393–404.
- Bessell, M. S. (1979). UBVRI photometry II: the Cousins VRI system, its temperature and absolute flux calibration, and relevance for two-dimensional photometry. *PASP*, 91:589–607.
- Boss, A. P. and Yorke, H. W. (1995). Spectral Energy of First Protostellar Cores: Detecting “Class -I” Protostars with ISO and SIRTF. *ApJL*, 439:L55.
- Bouvier, J., Alencar, S. H. P., Bouvier, T., Dougados, C., Balog, Z., Grankin, K., Hodgkin, S. T., Ibrahimov, M. A., Kun, M., Magakian, T. Y., and Pinte, C. (2007). Magnetospheric accretion-ejection processes in the classical T Tauri star AA Tauri. *A&A*, 463(3):1017–1028.
- Bouvier, J., Bertout, C., and Bouchet, P. (1986). DN Tauri : a spotted T Tauri star. *A&A*, 158:149–157.
- Bouvier, J., Cabrit, S., Fernandez, M., Martin, E. L., and Matthews, J. M. (1993). COYOTES I : the photometric variability and rotational evolution of T Tauri stars. *A&A*, 272:176–206.
- Bouvier, J., Chelli, A., Allain, S., Carrasco, L., Costero, R., Cruz-Gonzalez, I., Dougados, C., Fernández, M., Martín, E. L., Ménard, F., Mennessier, C., Mujica, R., Recillas, E., Salas, L., Schmidt, G., and Wichmann, R. (1999). Magnetospheric accretion onto the T Tauri star AA Tauri. I. Constraints from multisite spectrophotometric monitoring. *A&A*, 349:619–635.
- Bouvier, J., Grankin, K. N., Alencar, S. H. P., Dougados, C., Fernández, M., Basri, G., Batalha, C., Guenther, E., Ibrahimov, M. A., Magakian, T. Y., Melnikov, S. Y., Petrov, P. P., Rud, M. V., and Zapatero Osorio, M. R. (2003). Eclipses by circumstellar material in the T Tauri star AA Tau. II. Evidence for non-stationary magnetospheric accretion. *A&A*, 409:169–192.

- Bouvier, J., Matt, S. P., Mohanty, S., Scholz, A., Stassun, K. G., and Zanni, C. (2014). Angular Momentum Evolution of Young Low-Mass Stars and Brown Dwarfs: Observations and Theory. In Beuther, H., Klessen, R. S., Dullemond, C. P., and Henning, T., editors, *Protostars and Planets VI*, page 433.
- Calvet, N. and Gullbring, E. (1998). The Structure and Emission of the Accretion Shock in T Tauri Stars. *ApJ*, 509(2):802–818.
- Calvet, N., Hartmann, L., and Strom, S. E. (2000). Evolution of Disk Accretion. In Mannings, V., Boss, A. P., and Russell, S. S., editors, *Protostars and Planets IV*, page 377.
- Calvet, N., Muzerolle, J., Briceño, C., Hernández, J., Hartmann, L., Saucedo, J. L., and Gordon, K. D. (2004). The Mass Accretion Rates of Intermediate-Mass T Tauri Stars. *AJ*, 128(3):1294–1318.
- Calvet, N., Patino, A., Magris, G. C., and D’Alessio, P. (1991). Irradiation of Accretion Disks around Young Objects. I. Near-Infrared CO Bands. *ApJ*, 380:617.
- Carpenter, J. M., Hillenbrand, L. A., and Skrutskie, M. F. (2001). Near-Infrared Photometric Variability of Stars toward the Orion A Molecular Cloud. *AJ*, 121(6):3160–3190.
- Carpenter, J. M., Mamajek, E. E., Hillenbrand, L. A., and Meyer, M. R. (2006). Evidence for Mass-dependent Circumstellar Disk Evolution in the 5 Myr Old Upper Scorpius OB Association. *ApJL*, 651(1):L49–L52.
- Chiang, E. I. and Goldreich, P. (1997). Spectral Energy Distributions of T Tauri Stars with Passive Circumstellar Disks. *ApJ*, 490(1):368–376.
- Choi, P. I. and Herbst, W. (1996). Rotation Periods of Stars in the Orion Nebula Cluster: The Bimodal Distribution. *AJ*, 111:283.
- Cody, A. M., Stauffer, J., Baglin, A., Micela, G., Rebull, L. M., Flaccomio, E., Morales-Calderón, M., Aigrain, S., Bouvier, J., Hillenbrand, L. A., Gutermuth, R., Song, I., Turner, N., Alencar, S. H. P., Zwintz, K., Plavchan, P., Carpenter, J., Findeisen, K., Carey, S., Terebey, S., Hartmann, L., Calvet, N., Teixeira, P., Vrba, F. J., Wolk, S., Covey, K., Poppenhaeger, K., Günther, H. M., Forbrich, J., Whitney, B., Affer, L., Herbst, W., Hora, J., Barrado, D., Holtzman, J., Marchis, F., Wood, K., Medeiros Guimarães, M., Lillo Box, J., Gillen, E., McQuillan, A., Espaillat, C., Allen, L., D’Alessio, P., and Favata, F. (2014). CSI 2264: Simultaneous Optical and Infrared Light Curves of Young Disk-bearing Stars in NGC 2264 with CoRoT and Spitzer—Evidence for Multiple Origins of Variability. *AJ*, 147(4):82.
- Contreras Peña, C., Lucas, P. W., Froebrich, D., Kumar, M. S. N., Goldstein, J., Drew, J. E., Adamson, A., Davis, C. J., Barentsen, G., and Wright, N. J. (2014). Extreme infrared variables from UKIDSS - I. A concentration in star-forming regions. *MNRAS*, 439(2):1829–1854.
- Contreras Peña, C., Lucas, P. W., Kurtev, R., Minniti, D., Caratti o Garatti, A., Marocco, F., Thompson, M. A., Froebrich, D., Kumar, M. S. N., Stimson, W., Navarro Molina, C., Borissova, J., Gledhill, T., and Terzi, R. (2017a). Infrared spectroscopy of eruptive variable protostars from VVV. *MNRAS*, 465(3):3039–3100.

- Contreras Peña, C., Lucas, P. W., Minniti, D., Kurtev, R., Stimson, W., Navarro Molina, C., Borissova, J., Kumar, M. S. N., Thompson, M. A., Gledhill, T., Terzi, R., Froebrich, D., and Caratti o Garatti, A. (2017b). A population of eruptive variable protostars in VVV. *MNRAS*, 465(3):3011–3038.
- Contreras Peña, C., Naylor, T., and Morrell, S. (2019). Determining the recurrence timescale of long-lasting YSO outbursts. *MNRAS*, 486(4):4590–4611.
- Croswell, K., Hartmann, L., and Avrett, E. H. (1987). Mass Loss from FU Orionis Objects. *ApJ*, 312:227.
- Cutri, R. M. and et al. (2012). VizieR Online Data Catalog: WISE All-Sky Data Release (Cutri+ 2012). *VizieR Online Data Catalog*, page II/311.
- Cutri, R. M. and et al. (2013). VizieR Online Data Catalog: AllWISE Data Release (Cutri+ 2013). *VizieR Online Data Catalog*, page II/328.
- D’Alessio, P., Calvet, N., Hartmann, L., Franco-Hernández, R., and Servín, H. (2006). Effects of Dust Growth and Settling in T Tauri Disks. *ApJ*, 638(1):314–335.
- D’Alessio, P., Cantö, J., Calvet, N., and Lizano, S. (1998). Accretion Disks around Young Objects. I. The Detailed Vertical Structure. *ApJ*, 500(1):411–427.
- di Francesco, J., Evans, N. J., I., Caselli, P., Myers, P. C., Shirley, Y., Aikawa, Y., and Tafalla, M. (2007). An Observational Perspective of Low-Mass Dense Cores I: Internal Physical and Chemical Properties. In Reipurth, B., Jewitt, D., and Keil, K., editors, *Protostars and Planets V*, page 17.
- Ducati, J. R., Bevilacqua, C. M., Rembold, S. B., and Ribeiro, D. (2001). Intrinsic Colors of Stars in the Near-Infrared. *ApJ*, 558:309–322.
- Dullemond, C. P., Hollenbach, D., Kamp, I., and D’Alessio, P. (2007). Models of the Structure and Evolution of Protoplanetary Disks. In Reipurth, B., Jewitt, D., and Keil, K., editors, *Protostars and Planets V*, page 555.
- Dullemond, C. P., van den Ancker, M. E., Acke, B., and van Boekel, R. (2003). Explaining UX Orionis Star Variability with Self-shadowed Disks. *ApJL*, 594(1):L47–L50.
- Dutrey, A., Henning, T., Guilloteau, S., Semenov, D., Piétu, V., Schreyer, K., Bacmann, A., Launhardt, R., Pety, J., and Gueth, F. (2007). Chemistry in disks. I. Deep search for N₂H⁺ in the protoplanetary disks around LkCa 15, MWC 480, and DM Tauri. *A&A*, 464(2):615–623.
- Eisner, J. A. (2007). Water vapour and hydrogen in the terrestrial-planet-forming region of a protoplanetary disk. *Nature*, 447(7144):562–564.
- Evans, N. J., I., Rawlings, J. M. C., Shirley, Y. L., and Mundy, L. G. (2001). Tracing the Mass during Low-Mass Star Formation. II. Modeling the Submillimeter Emission from Preprotostellar Cores. *ApJ*, 557(1):193–208.
- Evans, Neal J., I., Dunham, M. M., Jørgensen, J. K., Enoch, M. L., Merín, B., van Dishoeck, E. F., Alcalá, J. M., Myers, P. C., Stapelfeldt, K. R., Huard, T. L., Allen, L. E., Harvey, P. M., van Kempen, T., Blake, G. A., Koerner, D. W., Mundy, L. G., Padgett, D. L., and Sargent, A. I. (2009). The Spitzer c2d Legacy Results: Star-Formation Rates and Efficiencies; Evolution and Lifetimes. *ApJS*, 181(2):321–350.

- Findeisen, K., Cody, A. M., and Hillenbrand, L. (2015). Simulated Performance of Timescale Metrics for Aperiodic Light Curves. *ApJ*, 798(2):89.
- Findeisen, K., Hillenbrand, L., Ofek, E., Levitan, D., Sesar, B., Laher, R., and Surace, J. (2013). Disk-related Bursts and Fades in Young Stars. *ApJ*, 768(1):93.
- Fitzgerald, M. P. (1970). The Intrinsic Colours of Stars and Two-Colour Reddening Lines. *A&A*, 4:234.
- Froebrich, D., Campbell-White, J., Scholz, A., Eislöffel, J., Zegmott, T., Billington, S. J., Donohoe, J., Makin, S. V., Hibbert, R., Newport, R. J., Pickard, R., Quinn, N., Rodda, T., Piehler, G., Shelley, M., Parkinson, S., Wiersema, K., and Walton, I. (2018a). A survey for variable young stars with small telescopes: First results from HOYS-CAPS. *MNRAS*, 478:5091–5103.
- Froebrich, D., Scholz, A., Campbell-White, J., Crumpton, J., D’Arcy, E., Makin, S. V., Zegmott, T., Billington, S. J., Hibbert, R., Newport, R. J., and Fisher, C. R. (2018b). Variability in IC5070: Two Young Stars with Deep Recurring Eclipses. *RNAAS*, 2(2):61.
- Gaia Collaboration (2018). VizieR Online Data Catalog: Gaia DR2 (Gaia Collaboration, 2018). *VizieR Online Data Catalog*, page I/345.
- Grankin, K. N. (1994). On the Stability of Spotted Regions on Stellar Surfaces of Weak-Line T Tauri Stars. *Information Bulletin on Variable Stars*, 4042:1.
- Grinin, V. P., Kozlova, O. V., Natta, A., Ilyin, I., Tuominen, I., Rostopchina, A. N., and Shakhovskoy, D. N. (2001). Optical spectra of five UX Orionis-type stars. *A&A*, 379:482–495.
- Grinin, V. P., The, P. S., de Winter, D., Giampapa, M., Rostopchina, A. N., Tambovtseva, L. V., and van den Ancker, M. E. (1994). The β Pictoris phenomenon among young stars. I. The case of the Herbig AE star UX Orionis. *A&A*, 292:165–174.
- Guieu, S., Rebull, L. M., Stauffer, J. R., Hillenbrand, L. A., Carpenter, J. M., Noriega-Crespo, A., Padgett, D. L., Cole, D. M., Carey, S. J., Stapelfeldt, K. R., and Strom, S. E. (2009). The North American and Pelican Nebulae. I. IRAC Observations. *ApJ*, 697(1):787–800.
- Gullbring, E., Hartmann, L., Briceño, C., and Calvet, N. (1998). Disk Accretion Rates for T Tauri Stars. *ApJ*, 492(1):323–341.
- Guo, Z., Herczeg, G. J., Jose, J., Fu, J., Chiang, P., Grankin, K., Michel, R., Kesh Yadav, R., Liu, J., Chen, W., Li, G., Xue, H., Niu, H., Subramaniam, A., Sharma, S., Prasert, N., Flores-Fajardo, N., Castro, A., and Altamirano, L. (2018). Star-Disk Interactions in Multiband Photometric Monitoring of the Classical T Tauri Star GI Tau. *ApJ*, 852:56.
- Haisch, K. E., J., Lada, E. A., and Lada, C. J. (2001). Disk Frequencies and Lifetimes in Young Clusters. *ApJL*, 553(2):L153–L156.
- Hartmann, L., D’Alessio, P., Calvet, N., and Muzerolle, J. (2006). Why Do T Tauri Disks Accrete? *ApJ*, 648(1):484–490.
- Hartmann, L., Herczeg, G., and Calvet, N. (2016). Accretion onto Pre-Main-Sequence Stars. *ARA&A*, 54:135–180.

- Hartmann, L. and Kenyon, S. J. (1996). The FU Orionis Phenomenon. *ARA&A*, 34:207–240.
- Hasegawa, Y. and Pudritz, R. E. (2011). The origin of planetary system architectures - I. Multiple planet traps in gaseous discs. *MNRAS*, 417(2):1236–1259.
- Hasegawa, Y. and Pudritz, R. E. (2012). Evolutionary Tracks of Trapped, Accreting Protoplanets: The Origin of the Observed Mass-Period Relation. *ApJ*, 760(2):117.
- Helled, R., Bodenheimer, P., Podolak, M., Boley, A., Meru, F., Nayakshin, S., Fortney, J. J., Mayer, L., Alibert, Y., and Boss, A. P. (2014). Giant Planet Formation, Evolution, and Internal Structure. In Beuther, H., Klessen, R. S., Dullemond, C. P., and Henning, T., editors, *Protostars and Planets VI*, page 643.
- Herbig, G. H. (1960). The Spectra of Be- and Ae-Type Stars Associated with Nebulosity. *ApJS*, 4:337.
- Herbig, G. H. (1966). On the interpretation of FU orionis. *Vistas in Astronomy*, 8(1):109–125.
- Herbig, G. H. (1977). Eruptive phenomena in early stellar evolution. *ApJ*, 217:693–715.
- Herbig, G. H. (1989). FU Orionis eruptions. In *European Southern Observatory Conference and Workshop Proceedings*, volume 33, pages 233–246.
- Herbst, W., Herbst, D. K., Grossman, E. J., and Weinstein, D. (1994). Catalogue of UVRI Photometry of T Tauri Stars and Analysis of the Causes of Their Variability. *AJ*, 108:1906.
- Herbst, W. and Shevchenko, V. S. (1999). A Photometric Catalog of Herbig AE/BE Stars and Discussion of the Nature and Cause of the Variations of UX Orionis Stars. *AJ*, 118(2):1043–1060.
- Herczeg, G. J. and Hillenbrand, L. A. (2008). UV Excess Measures of Accretion onto Young Very Low Mass Stars and Brown Dwarfs. *ApJ*, 681(1):594–625.
- Hernández, J., Hartmann, L., Calvet, N., Jeffries, R. D., Gutermuth, R., Muzerolle, J., and Stauffer, J. (2008). A Spitzer View of Protoplanetary Disks in the γ Velorum Cluster. *ApJ*, 686(2):1195–1208.
- Hernández, J., Hartmann, L., Megeath, T., Gutermuth, R., Muzerolle, J., Calvet, N., Vivas, A. K., Briceño, C., Allen, L., Stauffer, J., Young, E., and Fazio, G. (2007). A Spitzer Space Telescope Study of Disks in the Young σ Orionis Cluster. *ApJ*, 662(2):1067–1081.
- Hernández, J., Morales-Calderon, M., Calvet, N., Hartmann, L., Muzerolle, J., Gutermuth, R., Luhman, K. L., and Stauffer, J. (2010). Spitzer Observations of the λ Orionis Cluster. II. Disks Around Solar-type and Low-mass Stars. *ApJ*, 722(2):1226–1239.
- Hillenbrand, L. A., Contreras Peña, C., Morrell, S., Naylor, T., Kuhn, M. A., Cutri, R. M., Rebull, L. M., Hodgkin, S., Froebrich, D., and Mainzer, A. K. (2018). Gaia 17bpi: An FU Ori-type Outburst. *ApJ*, 869(2):146.
- Hillenbrand, L. A., Strom, S. E., Vrba, F. J., and Keene, J. (1992). Herbig Ae/Be Stars: Intermediate-Mass Stars Surrounded by Massive Circumstellar Accretion Disks. *ApJ*, 397:613.

- Hogg, D. W., Blanton, M., Lang, D., Mierle, K., and Roweis, S. (2008). Automated Astrometry (Invited). In Argyle, R. W., Bunclark, P. S., and Lewis, J. R., editors, *Astronomical Data Analysis Software and Systems XVII*, volume 394 of *Astronomical Society of the Pacific Conference Series*, page 27.
- Hughes, A. M., Wilner, D. J., Andrews, S. M., Qi, C., and Hogerheijde, M. R. (2011). Empirical Constraints on Turbulence in Protoplanetary Accretion Disks. *ApJ*, 727(2):85.
- Ibryamov, S., Semkov, E., Milanov, T., and Peneva, S. (2018a). Long-term BV RI photometric light curves of 15 PMS stars in the star-forming region IC 5070. *Research in Astronomy and Astrophysics*, 18:137.
- Ibryamov, S., Semkov, E., Milanov, T., and Peneva, S. (2019). VizieR Online Data Catalog: Long-term BVRI photometry of 15 PMS stars (Ibryamov+, 2018). *yCatp*, 0400:J/other/RAA/18.
- Ibryamov, S. I., Semkov, E. H., and Peneva, S. P. (2015). Long-Term Multicolour Photometry of the Young Stellar Objects FHO 26, FHO 27, FHO 28, FHO 29, and V1929 Cygni. *PASA*, 32:e021.
- Ibryamov, S. I., Semkov, E. H., and Peneva, S. P. (2018b). V2492 Cygni: Optical BVRI Variability During the Period 2010-2017. *PASA*, 35:e007.
- Ida, S. and Lin, D. N. C. (2008). Toward a Deterministic Model of Planetary Formation. V. Accumulation Near the Ice Line and Super-Earths. *ApJ*, 685(1):584–595.
- Jayawardhana, R., Coffey, J., Scholz, A., Brandeker, A., and van Kerkwijk, M. H. (2006). Accretion Disks around Young Stars: Lifetimes, Disk Locking, and Variability. *ApJ*, 648(2):1206–1218.
- Johansen, A., Blum, J., Tanaka, H., Ormel, C., Bizzarro, M., and Rickman, H. (2014). The Multifaceted Planetesimal Formation Process. In Beuther, H., Klessen, R. S., Dullemond, C. P., and Henning, T., editors, *Protostars and Planets VI*, page 547.
- Jorgensen, J. K., Bourke, T. L., Di Francesco, J., Lee, C. F., Myers, P. C., Ohashi, N., Schoeier, F. L., Takakuwa, S., van Dishoeck, E. F., Wilner, D. J., and Zhang, Q. (2005). Probing the Inner 200 AU of Low-Mass Protostars with the Submillimeter Array. In *American Astronomical Society Meeting Abstracts*, volume 207, page 184.16.
- Joy, A. H. (1945). T Tauri Variable Stars. *ApJ*, 102:168.
- Kalari, V. M., Vink, J. S., Drew, J. E., Barentsen, G., Drake, J. J., Eislöffel, J., Martín, E. L., Parker, Q. A., Unruh, Y. C., Walton, N. A., and Wright, N. J. (2015). Classical T Tauri stars with VPHAS+ - I. H α and u-band accretion rates in the Lagoon Nebula M8. *MNRAS*, 453(1):1026–1046.
- Kenyon, S. J., Hartmann, L. W., Strom, K. M., and Strom, S. E. (1990). An IRAS Survey of the Taurus-Auriga Molecular Cloud. *AJ*, 99:869.
- Kirk, J. M., Ward-Thompson, D., and André, P. (2005). The initial conditions of isolated star formation - VI. SCUBA mapping of pre-stellar cores. *MNRAS*, 360(4):1506–1526.
- Kitamura, Y., Momose, M., Yokogawa, S., Kawabe, R., Tamura, M., and Ida, S. (2002). Investigation of the Physical Properties of Protoplanetary Disks around T Tauri Stars by a 1 Arcsecond Imaging Survey: Evolution and Diversity of the Disks in Their Accretion Stage. *ApJ*, 581(1):357–380.

- Koenig, X. P. and Leisawitz, D. T. (2014). A Classification Scheme for Young Stellar Objects Using the Wide-field Infrared Survey Explorer AllWISE Catalog: Revealing Low-density Star Formation in the Outer Galaxy. *ApJ*, 791(2):131.
- Kolb, U., Brodeur, M., Braithwaite, N., and Minocha, S. (2018). A robotic telescope for university-level distance teaching. *Robotic Telescope, Student Research and Education Proceedings*, 1:127–136.
- Lada, C. J. (1987). Star formation: from OB associations to protostars. In Peimbert, M. and Jugaku, J., editors, *Star Forming Regions*, volume 115 of *IAU Symposium*, page 1.
- Lada, C. J., Muench, A. A., Luhman, K. L., Allen, L., Hartmann, L., Megeath, T., Myers, P., Fazio, G., Wood, K., Muzerolle, J., Rieke, G., Siegler, N., and Young, E. (2006). Spitzer Observations of IC 348: The Disk Population at 2-3 Million Years. *AJ*, 131(3):1574–1607.
- Larson, R. B. (1969). Numerical calculations of the dynamics of collapsing proto-star. *MNRAS*, 145:271.
- Leung, H. W. and Bovy, J. (2019). Simultaneous calibration of spectro-photometric distances and the Gaia DR2 parallax zero-point offset with deep learning. *MNRAS*, page 2167.
- Loomis, R. A., Öberg, K. I., Andrews, S. M., and MacGregor, M. A. (2017). A Multi-ringed, Modestly Inclined Protoplanetary Disk around AA Tau. *ApJ*, 840:23.
- Lucas, P. W., Hoare, M. G., Longmore, A., Schröder, A. C., Davis, C. J., Adamson, A., Bandyopadhyay, R. M., de Grijs, R., Smith, M., Gosling, A., Mitchison, S., Gáspár, A., Coe, M., Tamura, M., Parker, Q., Irwin, M., Hambly, N., Bryant, J., Collins, R. S., Cross, N., Evans, D. W., Gonzalez-Solares, E., Hodgkin, S., Lewis, J., Read, M., Riello, M., Sutorius, E. T. W., Lawrence, A., Drew, J. E., Dye, S., and Thompson, M. A. (2008). The UKIDSS Galactic Plane Survey. *MNRAS*, 391(1):136–163.
- Mainzer, A., Bauer, J., Cutri, R. M., Grav, T., Masiero, J., Beck, R., Clarkson, P., Conrow, T., Dailey, J., Eisenhardt, P., Fabinsky, B., Fajardo-Acosta, S., Fowler, J., Gelino, C., Grillmair, C., Heinrichsen, I., Kendall, M., Kirkpatrick, J. D., Liu, F., Masci, F., McCallon, H., Nugent, C. R., Papin, M., Rice, E., Royer, D., Ryan, T., Sevilla, P., Sonnett, S., Stevenson, R., Thompson, D. B., Wheelock, S., Wiemer, D., Wittman, M., Wright, E., and Yan, L. (2014). Initial Performance of the NEOWISE Reactivation Mission. *ApJ*, 792:30.
- Mainzer, A., Bauer, J., Grav, T., Masiero, J., Cutri, R. M., Dailey, J., Eisenhardt, P., McMillan, R. S., Wright, E., Walker, R., Jedicke, R., Spahr, T., Tholen, D., Alles, R., Beck, R., Brandenburg, H., Conrow, T., Evans, T., Fowler, J., Jarrett, T., Marsh, K., Masci, F., McCallon, H., Wheelock, S., Wittman, M., Wyatt, P., DeBaun, E., Elliott, G., Elsbury, D., Gautier, IV, T., Gomillion, S., Leisawitz, D., Maleszewski, C., Micheli, M., and Wilkins, A. (2011). Preliminary Results from NEOWISE: An Enhancement to the Wide-field Infrared Survey Explorer for Solar System Science. *ApJ*, 731:53.
- Majaess, D. (2013). Discovering protostars and their host clusters via WISE. *Ap&SS*, 344(1):175–186.
- Martín, E. L. (1998). Weak and Post-T Tauri Stars around B-Type Members of the Scorpius-Centaurus OB Association. *AJ*, 115(1):351–357.

- Masset, F. S., Morbidelli, A., Crida, A., and Ferreira, J. (2006). Disk Surface Density Transitions as Protoplanet Traps. *ApJ*, 642(1):478–487.
- Mathis, J. S. (1990). Interstellar dust and extinction. *ARA&A*, 28:37–70.
- Matsumura, S., Pudritz, R. E., and Thommes, E. W. (2009). The Growth and Migration of Jovian Planets in Evolving Protostellar Disks with Dead Zones. *ApJ*, 691(2):1764–1779.
- Matthews, B. C., Krivov, A. V., Wyatt, M. C., Bryden, G., and Eiroa, C. (2014). Observations, Modeling, and Theory of Debris Disks. In Beuther, H., Klessen, R. S., Dullemond, C. P., and Henning, T., editors, *Protostars and Planets VI*, page 521.
- Mayer, L., Quinn, T., Wadsley, J., and Stadel, J. (2002). Formation of Giant Planets by Fragmentation of Protoplanetary Disks. *Science*, 298(5599):1756–1759.
- McGinnis, P. T., Alencar, S. H. P., Guimarães, M. M., Sousa, A. P., Stauffer, J., Bouvier, J., Rebull, L., Fonseca, N. N. J., Venuti, L., Hillenbrand, L., Cody, A. M., Teixeira, P. S., Aigrain, S., Favata, F., Fűrész, G., Vrba, F. J., Flaccomio, E., Turner, N. J., Gameiro, J. F., Dougados, C., Herbst, W., Morales-Calderón, M., and Micela, G. (2015). CSI 2264: Probing the inner disks of AA Tauri-like systems in NGC 2264. *A&A*, 577:A11.
- Moffat, A. F. J. (1969). A Theoretical Investigation of Focal Stellar Images in the Photographic Emulsion and Application to Photographic Photometry. *A&A*, 3:455.
- Muzerolle, J., Hillenbrand, L., Calvet, N., Briceño, C., and Hartmann, L. (2003). Accretion in Young Stellar/Substellar Objects. *ApJ*, 592(1):266–281.
- Myers, P. C. and Ladd, E. F. (1993). Bolometric Temperatures of Young Stellar Objects. *ApJL*, 413:L47.
- Nagasawa, M., Ida, S., and Bessho, T. (2008). Formation of Hot Planets by a Combination of Planet Scattering, Tidal Circularization, and the Kozai Mechanism. *ApJ*, 678(1):498–508.
- Najita, J. R., Carr, J. S., Glassgold, A. E., and Valenti, J. A. (2007). Gaseous Inner Disks. In Reipurth, B., Jewitt, D., and Keil, K., editors, *Protostars and Planets V*, page 507.
- Natta, A., Grinin, V. P., Mannings, V., and Ungerechts, H. (1997). The Evolutionary Status of UX Orionis-Type Stars. *ApJ*, 491(2):885–890.
- Natta, A., Meyer, M. R., and Beckwith, S. V. W. (2000). Silicate Emission in T Tauri Stars: Evidence for Disk Atmospheres? *ApJ*, 534:838–845.
- Natta, A., Testi, L., Calvet, N., Henning, T., Waters, R., and Wilner, D. (2007). Dust in Protoplanetary Disks: Properties and Evolution. In Reipurth, B., Jewitt, D., and Keil, K., editors, *Protostars and Planets V*, page 767.
- Nealon, R., Dipierro, G., Alexander, R., Martin, R. G., and Nixon, C. (2018). Warping a protoplanetary disc with a planet on an inclined orbit. *MNRAS*, 481(1):20–35.
- Nelson, R. P., Papaloizou, J. C. B., Masset, F., and Kley, W. (2000). The migration and growth of protoplanets in protostellar discs. *MNRAS*, 318(1):18–36.
- Ogura, K., Sugitani, K., and Pickles, A. (2002). H α Emission Stars and Herbig-Haro Objects in the Vicinity of Bright-rimmed Clouds. *AJ*, 123:2597–2626.

- Omukai, K. (2007). Observational Characteristics of the First Protostellar Cores. *PASJ*, 59:589–606.
- Papaloizou, J. C. B. and Nelson, R. P. (2005). Models of accreting gas giant protoplanets in protostellar disks. *A&A*, 433(1):247–265.
- Pollack, J. B., Hubickyj, O., Bodenheimer, P., Lissauer, J. J., Podolak, M., and Greenzweig, Y. (1996). Formation of the Giant Planets by Concurrent Accretion of Solids and Gas. *Icarus*, 124(1):62–85.
- Pontoppidan, K. M., Blake, G. A., van Dishoeck, E. F., Smette, A., Ireland, M. J., and Brown, J. (2008). Spectroastrometric Imaging of Molecular Gas within Protoplanetary Disk Gaps. *ApJ*, 684(2):1323–1329.
- Pudritz, R. E., Ouyed, R., Fendt, C., and Brandenburg, A. (2007). Disk Winds, Jets, and Outflows: Theoretical and Computational Foundations. In Reipurth, B., Jewitt, D., and Keil, K., editors, *Protostars and Planets V*, page 277.
- Qi, C., Ho, P. T. P., Wilner, D. J., Takakuwa, S., Hirano, N., Ohashi, N., Bourke, T. L., Zhang, Q., Blake, G. A., Hogerheijde, M., Saito, M., Choi, M., and Yang, J. (2004). Imaging the Disk around TW Hydrae with the Submillimeter Array. *ApJL*, 616(1):L11–L14.
- Rafikov, R. R. (2009). Properties of Gravitoturbulent Accretion Disks. *ApJ*, 704(1):281–291.
- Raymond, S. N., Kokubo, E., Morbidelli, A., Morishima, R., and Walsh, K. J. (2014). Terrestrial Planet Formation at Home and Abroad. In Beuther, H., Klessen, R. S., Dullemond, C. P., and Henning, T., editors, *Protostars and Planets VI*, page 595.
- Rebull, L. M., Guieu, S., Stauffer, J. R., Hillenbrand, L. A., Noriega-Crespo, A., Stapelfeldt, K. R., Carey, S. J., Carpenter, J. M., Cole, D. M., Padgett, D. L., Strom, S. E., and Wolff, S. C. (2011). The North American and Pelican Nebulae. II. MIPS Observations and Analysis. *ApJS*, 193(2):25.
- Reipurth, B. and Schneider, N. (2008). *Star Formation and Young Clusters in Cygnus*, volume 4, page 36. Astronomical Society of the Pacific.
- Rodmann, J., Henning, T., Chandler, C. J., Mundy, L. G., and Wilner, D. J. (2006). Large dust particles in disks around T Tauri stars. *A&A*, 446(1):211–221.
- Rydgren, A. E., Zak, D. S., and Vrba, F. J. (1983). Further UBVRI Monitoring of Late-Type Young Stars. *BAAS*, 15:928.
- Sakai, N., Hanawa, T., Zhang, Y., Higuchi, A. E., Ohashi, S., Oya, Y., and Yamamoto, S. (2019). A warped disk around an infant protostar. *Nature*, 565(7738):206–208.
- Samus, N. N., Goranskii, V. P., Durlevich, O. V., Zharova, A. V., Kazarovets, E. V., Kireeva, N. N., Pastukhova, E. N., Williams, D. B., and Hazen, M. L. (2003). An Electronic Version of the Second Volume of the General Catalogue of Variable Stars with Improved Coordinates. *AstL*, 29:468–479.
- Sand, D. (2014). The Robotic FLOYDS Spectrographs. In Wozniak, P. R., Graham, M. J., Mahabal, A. A., and Seaman, R., editors, *The Third Hot-wiring the Transient Universe Workshop*, page 187.

- Scargle, J. D. (1982). Studies in astronomical time series analysis. II. Statistical aspects of spectral analysis of unevenly spaced data. *ApJ*, 263:835–853.
- Seifried, D., Banerjee, R., Pudritz, R. E., and Klessen, R. S. (2012). Disc formation in turbulent massive cores: circumventing the magnetic braking catastrophe. *MNRAS*, 423(1):L40–L44.
- Shang, H., Li, Z. Y., and Hirano, N. (2007). Jets and Bipolar Outflows from Young Stars: Theory and Observational Tests. In Reipurth, B., Jewitt, D., and Keil, K., editors, *Protostars and Planets V*, page 261.
- Sicilia-Aguilar, A., Hartmann, L., Calvet, N., Megeath, S. T., Muzerolle, J., Allen, L., D’Alessio, P., Merín, B., Stauffer, J., Young, E., and Lada, C. (2006a). Disk Evolution in Cep OB2: Results from the Spitzer Space Telescope. *ApJ*, 638(2):897–919.
- Sicilia-Aguilar, A., Hartmann, L. W., Fürész, G., Henning, T., Dullemond, C., and Brandner, W. (2006b). High-Resolution Spectroscopy in Tr 37: Gas Accretion Evolution in Evolved Dusty Disks. *AJ*, 132(5):2135–2155.
- Skrutskie, M. F., Cutri, R. M., Stiening, R., Weinberg, M. D., Schneider, S., Carpenter, J. M., and et al. (2006). The Two Micron All Sky Survey (2MASS). *AJ*, 131:1163–1183.
- Stahler, S. W. and Palla, F. (2005). *The Formation of Stars*. Wiley.
- Stauffer, J., Cody, A. M., Baglin, A., Alencar, S., Rebull, L., Hillenbrand, L. A., Venuti, L., Turner, N. J., Carpenter, J., Plavchan, P., Findeisen, K., Carey, S., Terebey, S., Morales-Calderón, M., Bouvier, J., Micela, G., Flaccomio, E., Song, I., Gutermuth, R., Hartmann, L., Calvet, N., Whitney, B., Barrado, D., Vrba, F. J., Covey, K., Herbst, W., Furesz, G., Aigrain, S., and Favata, F. (2014). CSI 2264: Characterizing Accretion-burst Dominated Light Curves for Young Stars in NGC 2264. *AJ*, 147(4):83.
- Stauffer, J., Cody, A. M., Rebull, L., Hillenbrand, L. A., Turner, N. J., Carpenter, J., Carey, S., Terebey, S., Morales-Calderón, M., Alencar, S. H. P., McGinnis, P., Sousa, A., Bouvier, J., Venuti, L., Hartmann, L., Calvet, N., Micela, G., Flaccomio, E., Song, I., Gutermuth, R., Barrado, D., Vrba, F. J., Covey, K., Herbst, W., Gillen, E., Medeiros Guimaraes, M., Bouy, H., and Favata, F. (2016). CSI 2264: Characterizing Young Stars in NGC 2264 with Stochastically Varying Light Curves. *AJ*, 151(3):60.
- Stetson, P. B. (1996). On the Automatic Determination of Light-Curve Parameters for Cepheid Variables. *PASP*, 108:851.
- Strom, K. M., Strom, S. E., Breger, M., Brooke, A. L., Yost, J., Grasdalen, G., and Carrasco, L. (1972). Infrared and Optical Observations of a Young Stellar Group Surrounding BD+40°4124. *ApJL*, 173:L65.
- Tanaka, H., Takeuchi, T., and Ward, W. R. (2002). Three-Dimensional Interaction between a Planet and an Isothermal Gaseous Disk. I. Corotation and Lindblad Torques and Planet Migration. *ApJ*, 565(2):1257–1274.
- Terebey, S., Shu, F. H., and Cassen, P. (1984). The collapse of the cores of slowly rotating isothermal clouds. *ApJ*, 286:529–551.
- The, P. S., Perez, M. R., and Van den Heuvel, E. P. J., editors (1994). *The nature and evolutionary status of Herbig Ae/Be stars*, volume 62 of *Astronomical Society of the Pacific Conference Series*.

- Ward-Thompson, D., Motte, F., and Andre, P. (1999). The initial conditions of isolated star formation - III. Millimetre continuum mapping of pre-stellar cores. *MNRAS*, 305(1):143–150.
- Weidenschilling, S. J. (1977). The Distribution of Mass in the Planetary System and Solar Nebula. *Ap&SS*, 51(1):153–158.
- Welch, D. L. and Stetson, P. B. (1993). Robust Variable Star Detection Techniques Suitable for Automated searches: New Results for NGC 1866. *AJ*, 105:1813.
- White, R. J. and Basri, G. (2003). Very Low Mass Stars and Brown Dwarfs in Taurus-Auriga. *ApJ*, 582(2):1109–1122.
- White, R. J. and Ghez, A. M. (2001). Observational Constraints on the Formation and Evolution of Binary Stars. *ApJ*, 556(1):265–295.
- White, R. J., Greene, T. P., Doppmann, G. W., Covey, K. R., and Hillenbrand, L. A. (2007). Stellar Properties of Embedded Protostars. In Reipurth, B., Jewitt, D., and Keil, K., editors, *Protostars and Planets V*, page 117.
- Wilner, D. J., D’Alessio, P., Calvet, N., Claussen, M. J., and Hartmann, L. (2005). Toward Planetesimals in the Disk around TW Hydrae: 3.5 Centimeter Dust Emission. *ApJL*, 626(2):L109–L112.
- Wright, E. L., Eisenhardt, P. R. M., Mainzer, A. K., Ressler, M. E., Cutri, R. M., Jarrett, T., Kirkpatrick, J. D., Padgett, D., McMillan, R. S., Skrutskie, M., Stanford, S. A., Cohen, M., Walker, R. G., Mather, J. C., Leisawitz, D., Gautier, T. N., I., McLean, I., Benford, D., Lonsdale, C. J., Blain, A., Mendez, B., Irace, W. R., Duval, V., Liu, F., Royer, D., Heinrichsen, I., Howard, J., Shannon, M., Kendall, M., Walsh, A. L., Larsen, M., Cardon, J. G., Schick, S., Schwalm, M., Abid, M., Fabinsky, B., Naes, L., and Tsai, C. (2010). The Wide-field Infrared Survey Explorer (WISE): Mission Description and Initial On-orbit Performance. *AJ*, 140(6):1868–1881.
- Wu, Y., Wei, Y., Zhao, M., Shi, Y., Yu, W., Qin, S., and Huang, M. (2004). A study of high velocity molecular outflows with an up-to-date sample. *A&A*, 426:503–515.
- Wyatt, M. C. (2008). Evolution of debris disks. *ARA&A*, 46:339–383.
- Zuckerman, B., Forveille, T., and Kastner, J. H. (1995). Inhibition of giant-planet formation by rapid gas depletion around young stars. *Nature*, 373(6514):494–496.

Appendix A: Description of Observatories and Data Reduction

A.1 Description of Amateur Observatories and Data

This section describes the equipment used by the various amateur astronomers. Each subsection also contains a basic description of the observing and data reduction procedures. The descriptions have been written by the participants for each observatory and edited by my supervisor, Dr. Dirk Froebrich. In order to protect the privacy and for safety reasons the exact locations of the amateur observatories are not published. There is an online map of the observatory locations¹ that shows their world-wide distribution. For the same reason the markers for the observatories are usually placed on a nearby (~ 1 km radius) road junction or landmark.

Amanecer de Arrakis Observatory

The observatory is located south of Seville, Andalusia, Spain. It uses an SC 8" telescope with an ICX285AL CCD chip. The optics results in a 1.92" per pixel resolution at 2×2 binning. A filter-set with B, V, R_c and I_c filters is available. Observations are typically taken with 50 s – 60 s exposure time. Science frames are reduced with Bias, Dark and Flat frames. MaximDL software is used for all data and calibration frame acquisition. On average about 3 or 4 night per week are used for observations. Observing conditions are clear for most of the year.

¹<https://www.google.co.uk/maps/@51,0,6000000m/data=!3m1!1e3!4m2!6m1!1s10hvfem7JcCjRodjofvwzGZBURSJsjvpw>

Anne and Lou Observatory

The observatory is located North of Roanoke, Virginia, USA in a roll off roof shed. It has a pier mounted AstroPhysics Mach1GTO mount and a GSO 250mm f/10 Ritchey-Chrétien carbon fiber tube telescope. It is further equipped with an AstroPhysics CCDT67 telecompressor, an Atik 428EX monochrome CCD with a Sony ICX674 Sensor. The optics provides a $22' \times 17'$ field of view at a $0.7''$ per pixel plate scale. The Atik filter wheel is equipped with Astrodon B, V and I_c filters. Depending on the target, typically 30 s and 60 s exposures are obtained. The images are Bias, Dark and Flat field corrected and stacked, using Astroart 6 software with ASCOM drivers.

AstroLAB IRIS Observatory

The public observatory is located in Zillebeke, South of Ypres in Belgium and host a 684 mm aperture Keller F4.1 Newtonian New Multi-Purpose Telescope (NMPT). It utilises a Santa Barbara Instrument Group (SBIG) STL 6303E CCD operated at -20°C . A 4 inch Wynne corrector feeds the CCD at a final focal ratio of 4.39, providing a nominal field of view of $20' \times 30'$. The $9\ \mu\text{m}$ physical pixels project to $0.62''$ and are read out binned to 3×3 pixels, i.e. $1.86''$ per combined pixel. The filter wheel is equipped with B, V, and R filters from Astrodon Photometrics. Typical exposures times are 20 s for HOYS imaging. Dark and Bias correction as well as stacking are done using Lesvephotometry². No flat-field correction is applied to the data.

Belako Observatory

The observatory is located near Muniga (North-East of Bilbao) in Spain. It uses a Meade LX200 SCT $10''$ telescope (254mm diameter) with ACF GPS f10 (2540mm focal length). The CCD is a SBIG ST2000-XM double chip with a pixel size of $7.4 \times 7.4\ \mu\text{m}$ and 1600×1200 pixel. The Mead 0.63 focal reducer results in a $0.84''$ per pixel resolution. The filter wheel, a SBIG CFW-10, is equipped with optical trichromia R, G, B, L and H _{α} filters from SBIG, as well as photometric B, V, Rc and Ic Johnson Coussin filters. Typical seeing is $2'' - 5''$ and exposure times up to 3 min are used for observations. Data capture and reduction including stacking are done using MaximDL, KStars & INDI³, and Deep Sky Stacker⁴.

Bowerhill Observatory

The Observatory is located East of Bath in the UK. It uses a Skywatcher Startravel telescope with 102 mm aperture, f/4.9 and a Canon 600D DSLR camera. The field of view is about 2° with $1.9''$ per pixel resolution. This telescope is placed on a Skywatcher EQ

²<http://www.dppobservatory.net/AstroPrograms/Software4VS0bservers.php>

³<https://www.indilib.org/>

⁴<http://deepskystacker.free.fr/english/index.html>

5 equatorial mount. Typically up to 120 60 s exposures are obtained at ISO 800 depending on darkness and weather conditions during the run. Data reduction is carried out using the IRIS software. The raw files from the DSLR are first decoded, then reduced with Dark and Flat frames and stacked.

Cal Maciarol mòdul 8 Observatory

The observatory is located in Parc Astronòmic del Montsec, Starlight reserve in Àger, Catalonia, Spain. The typical sky brightness is 21.5 mag/square arcsec towards the zenith and the typical seeing is 2''–4'' at the observatory's location. It uses a Meade LX200/R 12'' (305 mm aperture), f/8.9 (2720 mm focal length) telescope and a full-frame Moravian G9000 (KAF-09000 sensor, 36.7 mm × 36.7 mm, 12 μm pixel size) CCD camera. The field of view is 46.35' × 46.35' and the resolution per pixel is 0.91'' at 1 × 1 binning. The camera is equipped with a Moravian EFW-4L-7 filter wheel (up to 7 filters) with Astrodon 52 mm g' r' i' Sloan and V Johnson-Cousins filters placed into it. Typical HOYS observations are taken as 3–5 frames with 300 s exposures for each filter. The images are calibrated with Bias, Dark and twilight Flat Field frames (either evening or morning twilight depending on conditions). Image capture is performed with the KStars/Ekos software and data reduction and stacking with MaxIM DL.

CBA Extremadura Observatory

The Center for Backyard Astrophysics (CBA) Extremadura Observatory has an excellent location in a dry and dark part of Spain, just North of Fregenal de la Sierra. The site has on average about 280 clear nights per year. It is part of the e-EyE complex⁵, which is the largest telescope hosting place in Europe, providing high-end modules of individual observatories allowing astronomers from all over the world to remotely control their telescopes. The telescope is a 0.40 m f/5.1 Newton with a KAF-16200, ASA DDM-85 mount and a Starlight Xpress SX Trius SX-46 CCD camera. The filter wheel houses Clear, B, V, R and I filters. Observations are typically done with 3 × 3 binning at a pixel scale of 1.82'' per pixel and a field of view of 46' × 37'. A typical observing sequence for HOYS targets consists of 3 120 s exposures in B, V, R. Post processing is done using Lesve Photometry.

Chicharronian Tres Cantos Observatory

The observatory is situated about 15 miles North of Madrid, Spain. It has a 254 mm aperture f4.8 Skywatcher Newtonian telescope mounted on a Skywatcher EQ6 mount. The system is controlled by Astroberry Kstars and EKOS for scheduling and imaging. It uses an SBIG ST8XME mono CCD camera, cooled to 35°C below the ambient temperature. The pixel scale is 1.55''/pixel with a field of view of 39' × 28'. The telescope is also equipped with a SBIG CFW9 motorised filter wheel with Baader V, J-C and RGB

⁵www.entreencinasyestrellas.es

filters. Typically 5–20 images are stacked, with individual exposure times ranging from 120 s to 300 s, depending on object, filter and sky conditions.

Clanfield Observatory

The observatory is located in Clanfield, North of Portsmouth, UK and is run by the Hampshire Astronomical Group⁶. There are several telescopes in the observatory that have been used for HOYS imaging. i) An Astro-Physics 7-inch 'Starfire' F9 Apochromatic refractor with a Starlight Xpress SX-46 CCD Camera, Baader L, R, G, B, H α , SII, and OIII filters, Plate Scale: 0.773''/pixel and a field of view of 58.53' \times 46.93'. ii) A 24'' (612 mm) f7.9 Ritchey-Chrétien reflector with a Moravian G4-9000 CCD Camera, Baader L, H α , SII, and OIII filters, Astrodon R, V and B photometric filters, Plate Scale: 0.515''/pixel and a field of view of 26.21' \times 26.21'. iii) A Meade LX200 12 inch Schmidt-Cassegrain with f10 to f6.3 focal reducer and Starlight Xpress SX-46 CCD Camera, Baader L, R, G, B, H α , SII, and OIII filters, Plate Scale: 0.644''/pixel and a field of view of 48.72' \times 39.06'. iv) A 12'' (0.305 m) Newtonian Guided Reflector using an Atair Hypercam 183C 20mp Cooled Colour CMOS Camera with a plate scale of 0.26''/pixel and TR, TG, TB filters.

Several HOYS participants use the various telescopes. Typically observations range from 5 \times 30–300 s per filter on the CCD cameras, and 60 \times 30 s exposures for the CMOS camera, for up to several targets per night. Images are captured using Astro Photography Tool, Maxim DL or Moravian's SIPS for the G4-9000 camera, and are stacked and calibrated for Bias, Dark and Flat frames using PixInsight or Maxim DL.

El Guijo Observatory

The observatory is located North West of Madrid, Spain. It uses a 300 mm f/4 GSO Newtonian astrograph telescope mounted on a Celestron mount and controlled by TheSky6 Pro and CCDSoft for image capture. It utilises a SBIG ST-7 XME Kaf-0402 mono CCD camera, cooled to -15°C . It has an image scale of 1.53''/pixel and a field of view of 19.6' \times 13.1'. All HOYS images are taken with 20 \times 120 s in B and 15 \times 120 s in V, R, I filters.

Emsworth Observatory

The observatory is situated North East of Portsmouth, UK. It consists of two telescopes: i) A SW80+SX814 Skywatcher Evostar 80 ED DS Pro refractor with Starlight Xpress SX-814 CCD Camera and Baader Clear, H α , R, V, B, I, U photometric filters, Plate Scale: 1.269''/pixel and a field of view of 71.63' \times 57.34'. ii) A C8+SX814+FR Celestron NEXSTAR 8SE 8 inch Schmidt-Cassegrain f10 to f6.3 focal reducer with Starlight Xpress SX-814 CCD Camera and Baader Clear, H α , R, V, B, I, U photometric filters, Plate Scale: 0.982''/pixel and a field of view of 74.32' \times 59.59'.

⁶www.hantsastro.org.uk

Maxim DL6 is used to capture and process images, which are reduced using a library of Flats, Darks and Bias frames taken on each of the telescope/camera combinations.

Forthimage Observatory

Forthimage Observatory, in a semi-rural area on the western edge of Edinburgh, about 10 miles from the City centre. It uses a 250 mm f4.8 Orion Optics Newtonian telescope, a permanently pillar mounted Skywatcher EQ6-R mount, controlled by EQMOD and Cartes du Ciel, and autoguided using PHD2. It is housed in a motorised 2.2 m dome. The telescope is equipped with an Atik 460EX mono CCD camera, which is cooled to 25°C below ambient. The pixel scale is 0.79"/pixel resulting in a field of view of 36' × 29'. A Starlight Xpress motorised filter wheel with Baader tri-colour RGB and H_α filters is used. For HOYS observations typically 3–5 images are stacked, with individual exposure times ranging from 120 s to 300 s, depending on the target region, filter and sky conditions. Seeing in Edinburgh is typically around 1.5"–3". During May, June and July, all-night twilight interferes, but useful data can still be gathered, even under Civil Twilight conditions. Camera control and imaging are done by APT (AstroPhotography Tool) along with plate solving to frame the object accurately, flat fielding, bias and dark frame acquisition. Images are calibrated and stacked in Nebulosity 4.

Griffon Educational Observatory

The observatory is located near El Bosque in the South of Spain. It uses exactly the same equipment and observing procedures as the Bowerhill Observatory (see Appx. A.1) with the exception of a Skywatcher EQ6 mount.

Horndean Observatory

The observatory is situated North of Portsmouth in the UK. It uses a Williams Optics Zenith Star SD Doublet APO 66 mm telescope (Focal Length 388 mm) with a Canon EOS 600D(Mod) camera (pixel scale 2.29"/pixel), on a Skywatcher Star Adventurer Non Guided, Pulse dithered mount. The sky Quality is Class 4 Bortle. A Typical HOYS observing session consists of 60 × 30 s exposures to avoid trailing and minimize sky glow. Images are processed with Bias, Darks and Flats in Pixinsight. Usually 1 or 2 HOYS targets are observed per night.

Karen Observatory

The observatory is located in the North West of Warrington, UK. It uses a C11 Sct working at f7.5 telescope with a 278 mm aperture and 2780 mm focal length. It is equipped with a Starlight xpress SXV-H694 Trius CCD with a plate scale of 0.67"/pixel and field of view of 15.3' × 12.3'. The telescope uses off axis guiding with Starlight xpress X2. The motorised filter wheel contains a B, V, R, I, Baader 1/2 mm filter set.

Typical HOYS observations are taken with 10, 20, or 30 s exposure times and 10 or 20 are stacked depending on the target region and filter.

KSE Observatory

The Observatory is located North of San Diego, US. It uses a Meade LX200, 12'' (30.5 cm) telescope with F0.63 focal reducer. It is equipped with a Santa Barbara Instruments ST-7E CCD camera and a Johnson V filter. The field of view is 12.3' \times 8.2'. Typical HOYS imaging sessions consist of 6 \times 60 s exposures per target. Standard data reduction (bias, dark, flat correction) and stacking is performed with AIP4WIN Version 2.4.8.

La Vara, Valdes Observatory

The observatory is located in the North of Spain, West of Oviedo. It uses a RCX400 MEADE telescope with a SBIG STXE camera. The filter wheel is equipped with B, V, R, I filters. At 2 \times 2 binning the pixel scale is 1.74''/pixel and the field of view is 22.2' \times 14.8'. Typical exposure times for HOYS observations are 3 min with 3–6 images taken per filter. The typical seeing is about 4''. Dark, Bias and Flatfield corrections are applied to the images. Observations are conducted with CCD Soft v.5.

Les Barres Observatory

The observatory is located in the South of France, half way between Avignon and Marseille. It uses a Celestron Schmidt-Cassegrain SCT 203 mm telescope with focal reducer (f/8.1) and is equipped with a SBIG ST-8XME (KAF-1603ME) CCD. HOYS data is obtained using an Astrodon Johnson/Cousins V filter. The pixel scale is 1.13''/pixel and the field of view 28' \times 19'. Typically total integration times range from 30 min to 60 min with 2 min sub-exposures. Image calibration (flat, dark, bias correction and stacking) is performed with the Prism software⁷.

Mount Oswald Observatory

The observatory is situated some 2 km south of Durham city, UK. It is mainly used for the BAA VSS programme of variable stars and the HOYS project has been added to the list of targets. The telescope is a Skywatcher 190MN DS-Pro with a ZWO ASI1600MM Cooled CMOS Camera on a NEQ6 mount, the ZWO filter wheel holds Bessel B, V, R filters. The plate scale is 0.78''/pixel and a field of view of 60' \times 45'. Images are taken with the V-Band filter with integration times of 250 s with sub-exposures of 10 seconds managed semi-automatically using the Sequence Gen Pro software. The B and R filters have been recently acquired and will be used in the next imaging cycle. Calibration (bias, dark, flat-frame correction and image stacking) is performed in AstroImageJ.

⁷<https://www.hyperion-astronomy.com/pages/prism-landing>

Movil Observatory

The observatory is situated North of León in Spain. It uses a RC 12" telescope and QHY9 (AF8300 chip) CCD and a LodestarX2 off axis guider. The optics provides a resolution of 0.458"/pixel with a field of view of 25.63' × 19.36'. HOYS observations are typically done as 10 × 180 s exposure in a CV filter. Standard date reduction is applied.

Observatorio de Sencelles

The observatory is located South of Inca on Mallorca, Spain. It uses a Meade LX200 10" f/10 SC telescope with f/4.3 reducer and a ST-7XME CCD camera equipped with an Astrodon Johnson V filter. The pixel scale is 1.70"/pixel and the field of view 21.52' × 14.34'. The telescope is autoguided with a 200 mm, f/2.8 telephoto and Orion CCD. Data gathering and analysis is performed with a variety of software packages (MaximDL, TheSky, Fotodif, Elbrus, Astrometrica). Typical HOYS images are taken with exposure times ranging from 120 s to 900 s. Dark, bias and flatfield correction is applied to all images.

Observatorio El Sueño

The Observatory is situated in Vinyols i els Arcs, West of Tarragona, Spain. It uses a newton 300/1500 mm GSO telescope and ST8-XE SBIG CCD camera with AO. it is equipped with V, R_c, Johnson and Cousins filters. The optics results in a scale of 1.22"/pixel and a field of view of 20.7' × 31.0'. Typically HOYS observations are taken with 1200 s exposures. All images are dark and flatfield corrected using Maxim DL(Windows).

Observatorio Mazariegos

The observatory is located North of Valladolid, Spain. It uses a Celestron XLT 8" (2032 FL) and Atik 314L+ camera (Sony ICX-285AL CCD), equipped with V and R filters Johnson/Cousins. The pixel scale is 0.85"/pixel. Typically HOYS observations was taken as 120 s exposures. All images are dark and flatfield corrected following standard procedures using the MaximDL software.

Observatorio Montcabrer

The Observatory is situated North East of Barcelona, Spain. It uses a Meade ACF 305/3000 mm telescope and Moravian G4-900 CCD Camera, equipped with V, R_c Johnson-Cousins and g, r, i Sloan filters. The scale is 0.85"/pixel and the field of view 43' × 43'.

Typically HOYS observations are taken as 600 s exposures. All images are darks and flatfield corrected following standard procedures using the Kstars software.

Observatorio Nuevos Horizontes

The observatory is located in Camas, West of Seville, Spain. It uses a SC 9,25" telescope with an ICX285AL CCD chip. The optics results in a scale of 1.96"/pixel at 2×2 binning. The camera is equipped with a B, V, R filter set. HOYS observations are typically taken with 60 s exposure time. Science frames are reduced with Bias, Dark and Flat frames following standard procedures. The MaximDL software is used for all data and calibration frame acquisition. On average about 4 or 5 nights per week are used for observations. Observing conditions are clear for most of the year.

Rolling Hills Observatory

The observatory is located West of Orlando, Florida, USA. It uses a 35 cm aperture, f/10 Schmidt-Cassegrain telescope and a SBIG STT-8300M CCD with Astrodon B and V filters. The pixel scale (at 2×2 binning) is 0.64"/pixel and the field of view $17.4' \times 13.1'$. Typical HOYS observations are done as three images per filter with individual exposures of 75 s and 180 s in V and B, respectively. Dark images at the same camera temperature and exposure length were subtracted and then a sky flat is applied.

R.P. Feynman Observatory

The observatory is located in Gagliano del Capo in the South of Italy. The telescope used for HOYS observations is a 12" f/5.3 Orion Optics newtonian reflector with an Atik460Ex monochrome camera and Custom Scientific B, V, SR, SI filters. Using 2×2 binned pixels, this provides a plate scale of 1.18"/pixel and a field of view of $27' \times 21.6'$. Typical seeing in the images is around 3"–4". Integration times for the images range from 60 s to 240 s depending on target and filter. Image calibration (dark, flat-field correction and stacking) is carried out with the AstroArt software.

Sabadell Observatory

The observatory is situated North of Barcelona, Spain. It uses an Newton 500/2000 mm telescope and a Moravian G2-1600 camera equipped with Johnson-Cousins filters. The pixel scale is 0.92"/pixel and the field of view $23.5' \times 15.7'$. Typically HOYS observations are taken with 60 s exposures and set of 10–15 images are stacked. All images are dark and flatfield corrected using a number available software packages (Cartes du Ciel, AstroArt, Astrometrica, Focas).

Shobdon Observatory:

The observatory has already been described in Froebrich et al. (2018a). For completeness we reproduce here the text used in that earlier publication.

The observatory is situated in Herefordshire about 8 km from the UK/Wales Border. It houses a Meade LX200 35 cm SCT (f/7.7) operating at a focal length of 2500 mm with a Starlight XPress SXV-H9 CCD and a set of Johnson-Cousins B, V, R and I filters. Integration times are typically 60 s and darks and flats are applied using AIP4WIN software.

Steyning Observatory

The observatory has already been described in Froebrich et al. (2018a). For completeness we reproduce here the text used in that earlier publication.

The observatory is situated in Steyning, West Sussex, UK. The telescope is an 8'' (200 mm) Ritchey Chretien (f/8.0) operating at a focal length of 1600 mm with a Santa Barbara Instrument Group (SBIG) STF-8300M mono camera, and a 'green' filter from a tri-colour imaging set made by Astronomik. Using 2×2 binned pixels, this provides a plate scale of about 1.4''/pixel with a field of view of $39' \times 29'$. Integration times for the images range from 60 s to 240 s. Image calibration (darks, flat-fields and stacking) is carried out with the AstroArt software.

Tigra Automatic Observatory

The observatory is one of a pair located in Monkton Nature Reserve on the Isle of Thanet, Kent, UK. It uses a 305 mm f/10 Schmidt Cassegrain telescope (Meade LX200) mounted on an equatorial fork within a domed observatory. The CCD camera is manufactured by Santa Barbara Instruments Group (SBIG) and has a Kodak KAF-6303E non-antiblooming sensor with 3072×2048 pixels of $9 \mu\text{m}$. Guiding is aided by an SBIG AO-X adaptive optics unit. Filters available are Baader L, R, G, B, C and H_α , OIII and SII. Imaging for HOYS is normally performed with the sensor cooled to -35°C at 2×2 binning, for a measured image scale of 1.175''/pixel. Exposures are typically 300 s which are dark-subtracted, flat fielded and stacked to produce an image for submission to HOYS. The observatory is robotic and is scheduled and orchestrated by Astronomer's Control Program (ACP)⁸. Image processing and camera control is provided by MaxIm DL from Diffraction Limited⁹. Device control is performed using a number of ASCOM¹⁰ drivers developed by Tigra Astronomy¹¹.

⁸<http://www.dc3.com>

⁹<http://diffractionlimited.com/>

¹⁰<https://ascom-standards.org>

¹¹<http://tigra-astronomy.com/>

Uraniborg Observatory

The observatory is located in the South of Spain, between Seville and Córdoba. It uses a SC Celestron C11 telescope at $f6,3$ and an Atik 414ex monochrome CCD camera. The pixel scale is $0.779''/\text{pixel}$ and the field of view $18' \times 13'$. Images are taken either at the full resolution or using a 2×2 binning. Typically 40–60 s exposures are obtained for HOYS and 10–20 are stacked, depending on the target region. Dark, Bias and Flatfield corrections are applied using Maxim DL.

Warsash Observatory

The observatory is located in Warsash, between Portsmouth and Southampton in the UK. It uses a Williams Optics 110 mm Apochromatic Refractor with William Optics 0.8x Focal reducer/flattener and a Starlight Xpress SX 694 mono CCD camera for guided exposures. The camera has an image scale of $1.53''/\text{pixel}$ and a field of view of $71' \times 57'$. HOYS images are typically taken through a Photometric V filter (10×120 s), a Baader Red filter (10×30 s or 10×120 s) and Baader Blue filter (10×120 s). All images are calibrated and stacked following standard procedures using the SIPS software.

A.2 Description of University and Professional Observatories

This section describes the utilised University and professional telescopes. Each subsection also contains a basic description of the observing and data reduction procedures. The subsections have been written by participants and edited by my supervisor, Dr. Dirk Froebrich. Like for the amateur observatories, the locations are available on the online map.

Białków Observatory

The observatory is located at 51.474248°N , 16.657821°E , to the North West of Wrocław in Poland. The data in Białków were gathered with the 60 cm Cassegrain telescope equipped with an Andor Tech iKon-L DW432-BV back-illuminated CCD camera covering $13' \times 12'$ field of view in the B, V, Rc and Ic passbands of the Johnson-Kron-Cousins photometric system. The CCD has 1250×1152 pixels with a pixel size of $22.5 \mu\text{m}$ and a scale of $0.619''/\text{pixel}$. Exposure times range from 100 s to 140 s. The typical seeing is $2.5''$. Observations were calibrated in the standard way, which included dark and bias subtraction and flat-field correction. Custom made software and iraf package routines are used for data reduction.

Las Cumbres Observatory Global Telescope Network

Some of the projects participants used access to the range of telescopes from the Las Cumbres Observatory Global Telescope Network (LCOGT). The observatory has already been described in Froebrich et al. (2018a). For completeness we reproduce here the text used in that earlier publication.

LCOGT provides a range of 2 m, 1 m and 0.4 m telescopes located at various sites around the Earth to allow complete longitudinal coverage. The two 2 m telescopes are the Faulkes telescopes built by Telescope Technologies Ltd. which are f/10 Ritchey-Cretien optical systems. The 1 m telescopes are also Ritchey-Cretien systems with f/7.95, while the 0.4 m telescopes are Meade 16'' RCX telescopes. Data included in this work has been taken on Haleakala Observatory (0.4 m, 2 m), Siding Spring Observatory (0.4 m, 1 m) and Tenerife (0.4 m). All data from LCOGT are returned reduced with dark and flat-field corrections applied. Integration times are typically 60 s but depend on the target and telescope size.

OpenScience Observatories - COAST Observatory

The observatory is located at the Observatorio del Teide, Tenerife, Spain (same site as the PIRATE observatory - see Appx. A.2. It is currently operated by the Open University, and a fully autonomous, queue-scheduled system. The telescope is a Celestron 14'' Schmidt-Cassegrain (f/10) on a 10Micron GM4000 mount. It uses a FLI ProLine KAF-09000 CCD with photometric Johnson B, V, R filters. The field of view is 33' × 33' at a pixel scale of 0.65''/pixel.

Image calibration has been performed with COAST pipeline, and fully calibrated images have been retrieved. Dark and Bias subtraction has been done with library frames and dawn sky flats are used for flat-fielding. Typical HOYS observations consist of single integrations of 40 s–60 s, repeated roughly 2–3 times a week.

OpenScience Observatories - PIRATE (Open University)

The observatory (Kolb et al., 2018) is sited at Teide Observatory (Latitude: 28.299286°N, Longitude: 16.510297°W, Altitude: 2370 m). It uses a 17'' (432 mm) Aperture Planewave CDK17 telescope with Cassegrain optics (2939 mm Focal Length, Focal ratio f/6.8) on a 10Micron GM4000 HPS mount. It is equipped with a FLI ProLine PL16803 Camera with a KAF-16803 CCD and a 10 position filter wheel (U, B, V, R, I, H_α, OIII, SII, Clear). The field of view is 43' × 43' with 0.63''/pixel resolution.

Dark, Bias and Flat field frames are taken at dusk and dawn every day. Data is reduced using a custom built pipeline that is loosely based off AstroImageJ and follows a standard calibration technique, it also removes the overscan region of the CCD. Seeing conditions are typically better than 1'', and during the summer, 50 % of the time the seeing is better than 0.54''. All images were taken with 100 s exposure times. The typical HOYS observing pattern includes taking two exposures in B, V, R, H_α filters

every night.

University of Kent Beacon Observatory

The observatory has already been described in Froebrich et al. (2018a). For completeness we reproduce here the text used in that earlier publication.

The Beacon Observatory consists of a 17'' *Planewave* Corrected Dall-Kirkham (CDK) Astrograph telescope situated at the University of Kent (51.296633° North, 1.053267° East, 69 m elevation). The telescope is equipped with a 4k × 4k Peltier-cooled CCD camera and a B, V, R_c, I_c, H_α filter set. The pixel scale of the detector is 0.956'', giving the camera a field of view of about 1° × 1°. Due to the optical system of the telescope the corners of the detector are heavily vignetted. Hence the usable field of view of the detector is a circular area with a diameter of approximately 1°.

The observatory has, despite its location, a good record for observations. Over the first two years of operations an average of 10 nights per month were used for science observations, with an average of 50 hrs per month usable, i.e. just above 50% of the time is used in each night with clear skies. The typical seeing in the images is about 3''–4''.

Images taken by the observatory for the HOYS project are typically taken in the following sequence: 120 s integrations are done in V, R_c, and I_c and this sequence is repeated 8 times. Including filter changes and CCD readout, this sequence takes one hour. All individual images are dark and bias subtracted and flat-fielded using sky-flats. All images taken of a particular target during a sequence are median averaged using the Montage software package¹².

University of Leicester Observatory (UL50)

The observatory has already been described in Froebrich et al. (2018a). For completeness we reproduce here the text used in that earlier publication.

The University of Leicester runs a 0.5 m telescope (the University of Leicester 50 cm, or UL50). This is a 20'' *Planewave* CDK telescope with a SBIG ST2000XM camera. It is equipped with a Johnson-Cousins B, V, R, I filter-set. Data were reduced using dark, bias and flat-frames taken the same night as science observations, using an IRAF pipeline. In addition the observatory now operates a Moravian Instruments G3-11000 CCD camera with Johnson-Cousins B, V, R, I filters.

¹²<http://montage.ipac.caltech.edu/>

Thüringer Landessternwarte

The observatory has already been described in Froebrich et al. (2018a). For completeness we reproduce here the text used in that earlier publication.

The Thüringer Landessternwarte is operating its Alfred-Jensch 2 m telescope¹³ near Tautenburg (50.980111° North, 11.711167° East, 341 m elevation, Germany). For HOYS the telescope is used in its Schmidt configuration (clear aperture 1.34 m, mirror diameter 2.00 m, focal length 4.00 m). It is equipped with a 2k × 2k liquid nitrogen-cooled CCD camera and with a U, B, V, R, I, H α filter set. The employed SiTe CCD has 24 μm × 24 μm pixels, leading to a field of view of 42' × 42'. Single exposures of 20 s to 120 s integration time – depending on the filter – are obtained, and several consecutive frames may be co-added. Dark frames and dome-flats are used for image calibration.

Vihorlat Observatory

The observatory is located in eastern Slovakia at 48.935000°N, 22.273889°E. the Vihorlat National Telescope is a 1000 mm aperture and 9000 mm focal length telescope equipped with a FLI PL 1001E camera. At 2 × 2 binning the pixel scale is 1.11''/pixel and the field of view 9.47' × 9.47'. The filter wheel contains a B, V, R_c, I_c, and Clear Johnson Cousins filter set. For HOYS targets we use 2 min or 3 min exposure times, with at least 5 images in every filter, Typical seeing conditions are around 3''. The data reduction is following standard procedures with bias, dark and sky flat corrections and image stacking. For image acquisition we use MaximDL, the data reduction is performed by recently developed CoLiTecVS software¹⁴.

iTelescope Network

Several of the amateur observers have used access to the iTelescope network¹⁵ to support HOYS observations. In particular the T5 and T7 telescopes were used.

The T5 telescope is situated at the New Mexico Skies Observatory near Mayhill in the US. It uses a 0.25 m f/3.4 reflector and SBIG ST-10XME CCD equipped with Red Green Blue, Ha, SII, OIII, Clear and Johnson's Cousins's Photometric B, V, and I filters. The field of view is 60.6' × 40.8' at a scale of 1.65''/pixel.

The T7 telescope is situated at Astro Camp Nerpio, west of Murcia in Spain. It uses a 0.43 m f/6.8 reflector and SBIG STL-11000M CCD equipped with R, V, B, Ha, OIII, SII, I filters. The field of view is 28.2' × 42.3' at a scale of 0.63''/pixel.

¹³<http://www.tls-tautenburg.de/TLS/index.php?id=25&L=1>

¹⁴[http://www.neoastrosoft.com/colitecvsvs_\\$en/](http://www.neoastrosoft.com/colitecvsvs_$en/)

¹⁵<https://www.itelescope.net/>